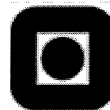


Fatigue Strength of Titanium Risers

Defect Sensitivity

A thesis submitted in partial fulfillment of the
Requirements for the degree of
Doktor Ingeniør
by
Olusegun Tunde Babalola

Trondheim, 2001



DEPARTMENT OF MARINE STRUCTURES
FACULTY OF MARINE TECHNOLOGY
NORWEGIAN UNIVERSITY OF SCIENCE AND TECHNOLOGY

ABSTRACT

This study is centred on assessment of the fatigue strength of titanium fusion welds for deep-water riser's applications. Deep-water risers are subjected to significant fatigue loading.

Relevant fatigue data for titanium fusion welds are very scarce. Hence there is a need for fatigue data and life prediction models for such weldments.

The study has covered three topics: Fatigue testing, Fractography and defect assessment, and Fracture Mechanics modelling of fatigue crack growth.

Two series of welded grade of titanium consisting of 14 specimens in each series were fatigue tested under constant amplitude loading. Prior to fatigue testing, strain gauge measurements of some specimens was conducted to enable the definition of stress range in the fatigue assessment procedure. The results were compared with finite solid element analysis and related to fatigue stresses in a riser pipe wall.

Distribution and geometry of internal and surface defects both in the as-welded and in the post-weld machined conditions were assessed using fractography. This served as a tool to determine the fatigue initiation point in the welds.

Fracture mechanics was applied to model fatigue strength of titanium welds with initiation from weld defects. Two different stress intensity factor formulations for embedded eccentrically placed cracks were used for analysis of elliptical cracks with the major axis parallel and close to one of the free surfaces. The methods were combined to give a satisfactory model for crack growth analysis.

The model analyses crack growth of elliptical and semi-elliptical cracks in two directions, with updating of the crack geometry. Fatigue strength assessment was conducted using two crack growth models, the Paris-Erdogan relation with no threshold and the Donahue et al. relation with an implied threshold.

The model was validated against experimental data, with a discussion on the choice of crack growth model.

ACKNOWLEDGEMENTS

First and foremost, I thanked God for giving me the strength to endure the bitterness in the root of patience so as to enjoy the sweetness of its fruit.

This work was carried out under the supervision of Prof. Stig Berge. Before the work came to its present form, Stig was very patient and painstakingly reviewed each part. I am indeed very grateful.

Kjell Müller and Dall Wilhelm of SINTEF Material Technology at one point or the other provided insight in the use of Scanning Electron Microscope (SEM). Koji Gotoh of Department of Naval Architecture and Marine Systems Engineering, Kyushu University, Japan was of tremendous help in the finite element work and proof reading of Chapter 5 and 10. David Økland of MARINTEK, Structural Engineering also helped in understanding some part of the finite element result. I am also grateful for the assistance of Roar Schjetne and Eirik Fleischer of the Marine Structural Laboratory, Department of Marine Structures.

The administrative staffs of Faculty of Marine Technology are a delight to know and work with, Bjørn Østbye, Mustafa, Lisbet Slagstad, Grete, Kari. Also our dear Leif Lundby, Sigríð and Marianne. Keep on smiling!

This work was financed by a grant from a Joint Industry Project (JIP) on Titanium Risers and Flowlines, with additional support from the Faculty of Marine Technology in conjunction with Department of Marine Structures at the Norwegian University of Science and Technology, and from MARINTEK, Department of Structural Engineering.

Table of Contents

Abstract	i
Acknowledgements	iii
Table of Contents.....	iv
List of Figures	vii
List of Tables.....	xiii
NOMENCLATURE	xiv
1 INTRODUCTION.....	1
1.1 Background and Objective.....	1
1.2 Scope of Work	2
1.3 Organisation of the Thesis.....	4
2 TITANIUM RISERS.....	5
2.1 Applications.....	5
2.2 Performance Characteristics of Titanium for Riser Application Compared to Steel	6
3 BASIC MATERIAL PROPERTIES	11
3.1 Pipe Materials.....	11
3.2 Chemical Composition	12
3.3 Properties of Titanium Alloy	13
4 WELDING	17
4.1 Welding processes	17
4.1.1 Pressure welding processes	17
4.1.2 Fusion welding processes.....	19
4.1.3 TIG fusion welding	20
4.2 Weld Defects.....	21
5 STRESS DISTRIBUTION ACROSS THE FUSION WELD	25
5.1 Specimens	25
5.2 Experimental	26
5.3 Results	28

5.3.1 Root ground specimens	29
5.3.2 Machined and ground specimens.....	30
5.4 Finite Element Analysis.....	30
5.4.1 Boundary conditions and applied loading	31
5.4.2 As welded condition – test specimen.....	32
5.4.3 Fully machined and ground specimen	34
5.4.4 As-welded condition – full pipe	37
5.4.5 Plain pipe.....	40
5.5 Comparison Between Experimental And Finite Element Analysis	
Result	41
5.5.1 As-welded specimens.....	41
5.5.2 Fully machined and ground specimens.....	42
5.5.3 Coupon specimens vs. full section pipe	42
5.6 Conclusion	42
6 FATIGUE TESTING.....	45
6.1 Mean Stress Level.....	45
6.2 SN Testing - Experimental	49
6.3 Test Equipment	49
6.4 Test Specimen	49
6.5 SN Fatigue Testing.....	50
7 FRACTOGRAPHIC INVESTIGATIONS – BASIC CONCEPTS.....	53
7.1 Objective	53
7.2 Scanning Electron Microscopy	54
7.3 Fractographic Features.....	55
7.3.1 Shear lips	55
7.3.2 Chevron markings	57
7.3.3 Beach marks.....	57
7.3.4 Fatigue striations	58
7.3.5 Dimples.....	59
7.4 Fatigue Crack Initiation and Growth	60
7.4.1 Crack initiation	60
7.4.2 Crack growth	62
8 FRACTOGRAPHIC INVESTIGATION – MAIN CONCEPTS.....	65
8.1 Classification of Defects	65

8.2 Surface Defects	67
8.3 Internal Defects	76
8.3.1 Clusters of pores	84
8.4 Results.....	87
9 STRESS INTENSITY FACTOR.....	89
9.1 Small Fatigue Cracks.....	89
9.2 Modelling of Internal Defect Near Free Surface Under Tension	91
9.2.1 Magnification Correction Factor For An Embedded Elliptical Crack	92
9.3 Elliptical Crack Under A Linear Stress Distribution	96
10 FRACTURE MECHANICS-BASED FATIGUE LIFE METHODS....	97
10.1 Fatigue Crack Growth Rate	97
10.1.1 Threshold region	99
10.1.2 Crack growth in three dimensions.....	100
10.1.3 Cracks growing from internal defects.....	101
10.2 Form Factors for the Stress Intensity Factor	102
10.2.1 Influence of the weld geometry	102
10.2.2 Finite size corrections	102
10.2.3 Effect of crack closure.....	103
10.2.4 Crack growth relations for internal /surface cracks	103
10.3 Fatigue initiation life	104
11 FATIGUE CRACK GROWTH IN WELDED TITANIUM 6-4 ALLOY IN THE PRESENCE OF EMBEDDED DEFECT.....	105
12 FRACTURE MECHANICS ANALYSIS RESULTS.....	111
12.1 Stress Intensity Factor Model.....	112
12.1.1 Case 1: $b < a$	112
12.1.2 Case 2: $b > a$	113
12.2 Model For Crack Increment And Stress Intensity Factor Updating..	114
12.3 Selection of Threshold for The Crack Growth Formula.....	120
13 CONCLUSIONS AND RECOMMENDATIONS	125
13.1 Summary	125
13.2 Concluding Remarks.....	127
13.3 Recommendations for further studies	128
REFERENCES.....	131

List of Figures

Figure 2.1	Thick – end riser joint concept. The outer diameter of the pipe is increased locally at the weld.....	7
Figure 2.2	Connection of a riser to a floating production system. Typical application for a titanium stress joint.....	8
Figure 4.1	Rotary friction weld (schematic), with excess material which needs to be machined off.....	18
Figure 4.2	Radial friction welding principle.....	18
Figure 4.3	Schematic representation of a multipass TIG weld.....	19
Figure 4.4	Vertical downward technique, welding from 12 o'clock to 6 o'clock in multiple runs.....	21
Figure 4.5	Lack of fusion due to cold lap.....	21
Figure 4.6	Pores due to presence of hydrogen during welding. The grey area is the final fracture zone.....	22
Figure 5.1	(a) Strain gauge location at the fusion weld (b) and (c) Dog-bone coupon specimen from the pipe wall (schematic).....	27
Figure 5.2	Stress distribution through the plate thickness for the as-welded model, at the center of the weld.....	32
Figure 5.3	Stress distribution through the plate thickness for the as-welded model, at the toe of the weld.....	33
Figure 5.4	Stress distribution through the plate thickness for the as-welded model measured 10mm away from the toe of the weld.....	33
Figure 5.5	Contour plot of the axial stress in the specimen.....	34

Figure 5.6	Stress distribution through the plate thickness for the fully machined and ground specimen measured at the weld centre.....	34
Figure 5.7	Stress distribution at the toe of the weld through the plate thickness for the fully machined and ground model..	35
Figure 5.8	Stress distribution at 10mm away from the weld toe through the plate thickness for the fully machined and ground model.....	35
Figure 5.9	Specimen with weld profile in fully ground condition showing the boundary condition.....	36
Figure 5.10	Stress distribution through the pipe wall for the as-welded pipe at centre of the weld.....	37
Figure 5.11	Stress distribution through the pipe wall for the as-welded pipe at the toe of the weld.....	38
Figure 5.12	Stress distribution for the as-welded pipe in the thickness direction, at 16mm away from the toe of the weld.....	38
Figure 5.13	Contour of axial stress for the as-welded pipe.....	39
Figure 5.14	Stress distribution through the pipe wall at the weld centre.....	39
Figure 5.15	Stress distribution through the pipe wall at the weld toe..	40
Figure 5.16	Stress distribution through the pipe wall at 16mm away from the toe of the weld.....	40
Figure 5.17	Plain pipe with the boundary and loading condition.....	41
Figure 6.1	Effect of mean stress on fatigue life (Schematic).....	45
Figure 6.2	Haigh diagram showing the effect of mean stress, and the modified Goodman, Gerber and Søderberg relations.....	47
Figure 6.3	Effect of high stress ratio on the fatigue life.....	48
Figure 6.4	Instron closed-loop electro- hydraulic servo controlled testing systems (schematic).....	48
Figure 6.5	SN data for RA 41 series (1G welds). Initiation of fatigue failure for the entire specimen in the ground condition is internal.....	52

Figure 6.6	SN data for RA 42 series (5G welds). Only two of the specimens (represented with a 'x') in the ground condition had internal fatigue initiation.....	52
Figure 7.1	Fatigue test piece.....	53
Figure 7.2	Scanning electron microscope.....	53
Figure 7.3	(a) Shear lips in cup-cone fracture, (b) Shear lip zone of an un-notched cylindrical specimen and (c) Diagrammatic representation of fracture surface marks in rectangular tension specimen subjected to monotonic loading.....	55
Figure 7.4	Crack growth showing radial marks known as chevron – the origin of the crack is at the right edge of the specimen.....	56
Figure 7.5	Beach marks.....	57
Figure 7.6	Ductile striation in fatigued Titanium 6-4 alloy specimens as seen on SEM images.....	58
Figure 7.7	Ductile dimples typified final fracture region in fatigued Titanium 6-4 alloy specimens as seen on SEM. The dimples are a result of plastic deformation during the fracture process.....	59
Figure 7.8	(a) Slip band with extrusions and intrusion formed on the surface of a grain subjected to cyclic stress. Crack nucleation at intrusion. (b) Stage I and Stage II crack growth in polycrystalline material.....	62
Figure 8.1	Idealised representation of as-detected defects.....	65
Figure 8.2	Surface breaking pores (a) X20, (b) X250, Specimen R03/13.....	68
Figure 8.3	Surface breaking pores (re-categorised), Specimen R08/7.	69
Figure 8.4	Surface breaking pores (semi-elliptic pore), Specimen BS10.....	69
Figure 8.5	Surface breaking pores (re-categorised), Specimen RA42/9.....	70

Figure 8.6	Surface breaking pores, Specimen RA42/8.....	70
Figure 8.7	Multi-origin crack initiation from the clusters of pores, Specimen RA42/5.....	71
Figure 8.8	Fatigue crack originating from a corner crack, Specimen RA42/6.....	72
Figure 8.9	Fatigue crack initiation from the elliptical pore to the left, Specimen RA42/13.....	72
Figure 8.10	Fatigue crack initiation due to formation of PSBs, Specimen RA41/14.....	73
Figure 8.11	Fatigue crack initiation from the surface, Specimen RA41/12.....	74
Figure 8.12	Fatigue crack initiation from the surface. X10, Specimen RA42/3.....	74
Figure 8.13	Fatigue crack initiation from the surface. X100, Specimen RA42/3.....	75
Figure 8.14	Fatigue crack initiation from the surface, Specimen T35/6.....	75
Figure 8.15	Fatigue crack initiation from the surface, Specimen T39/11.....	76
Figure 8.16	Fatigue crack initiation due to embedded flaw, Specimen RA42/10.....	76
Figure 8.17	Fatigue crack initiation due to surface and an embedded flaw, Specimen RA41/13.....	77
Figure 8.18	Internal initiation from the elliptical crack, Specimen RA41/6.....	78
Figure 8.19	Internal initiation from the elliptical crack, Specimen Ra41/10.....	79
Figure 8.20	Internal initiation from the elliptical crack, Specimen RA41/7.....	79
Figure 8.21	Internal initiation from the elliptical crack, Specimen RA41/8.....	80
Figure 8.22	Fatigue crack initiation due to embedded flaw, Specimen RA42/12.....	80

Figure 8.23	Fatigue crack initiation due to embedded flaw, Specimen RA41/9.....	81
Figure 8.24	Fatigue crack initiation due to embedded flaw. The arrow points to dimples zone indicating a ductile mode of failure, Specimen RA42/14.....	82
Figure 8.25	Embedded elliptic crack as a fatigue origin, Specimen R08/2.....	82
Figure 8.26	Fatigue crack initiation due to lack of fusion defect, Specimen AS6.....	83
Figure 8.27	Fatigue crack initiation due to lack of fusion defect, Specimen BS2.....	84
Figure 8.28	Clusters of pores. X10 the origin of the fatigue crack is to the far left, Specimen RA42/11.....	84
Figure 8.29	Clusters of pores. X10 but overlapped with (Figure 8.28), Specimen RA42/11.....	85
Figure 8.30	Clusters of pores as fatigue initiation origin. X10, Specimen BS7.....	85
Figure 8.31	Clusters of pores as fatigue initiation origin. The largest pore to the left and the two others above it were assumed to interact, Specimen BS7.....	86
Figure 9.1	An elliptical crack embedded in plate subjected to uniform tension.....	91
Figure 9.2	Concept of front surface and back surface corrections.....	95
Figure 10.1	Crack growth rate curve. Region A, B and C denoted threshold, Paris-Erdogan and final failure region respectively.....	98
Figure 10.2	Cycle by cycle crack extension. (a) With constant half-axis – growth in two degrees of freedom, d_1 varied. (b) Modified form of (a), growth in 3 degrees of freedom, d_1 constant.....	100
Figure 11.1	(a) Crack depth, b as a function of the number of cycles to failure. (b) Critical defect size for a semi-elliptical surface crack and elliptical embedded flaw.....	109

Figure 12.1	Elliptical crack embedded in plate subjected to uniform tension.....	111
Figure 12.2	Extending Method 2 for a crack with $b > a$ using Model 1.....	113
Figure 12.3	Extending Method 2 for a crack with $b > a$ using Model 2.....	114
Figure 12.4	Semi-infinite solution compare with finite thickness solution and $d_1 = \text{constant}$	115
Figure 12.5	Method 1: Calculated fatigue life is compared under pure membrane and combined loading conditions i.e. membrane stress (85% stress range) and bending (15% stress range). $d_1 = \text{constant}$	116
Figure 12.6	Method 1: Calculated fatigue life is compared under pure membrane and combined loading condition i.e. membrane stress (85% stress range) and bending (15% stress range). $d_1 = \text{constant}$	117
Figure 12.7	Method 1 (Fett et al., 1997) and Method 2 (Isida_Fett / Isida_extr) are compared for Case 1 with $b < a$ under tensile loading condition.....	117
Figure 12.8	Model verification for the calculated fatigue life for Case 2 with $b > a$	118
Figure 12.9	Fatigue life calculated compare for constant d_1 and varied d_1 using Method 1.....	119
Figure 12.10	Iterated form of equation (10.2) i.e. assuming F is not constant and equation (12.2) i.e. assuming F is constant. Case $b < a$	121
Figure 12.11	Iterated form of equation (10.2) i.e. assuming F is not constant and equation (12.2) i.e. assuming F is constant. Case $b > a$	122
Figure 12.12	Estimation of fatigue life for surface defect using equation (10.2) i.e. F iterated.....	123

List of Tables

Table 3.1	Grades of pipe material taken as dog-bone coupon specimens from the pipe wall.....	11
Table 3.2	Key properties of Ti-6Al-4V ELI (Peacock, 1999).....	13
Table 5.1	Secondary bending stress for specimens with the inner side (root) of the weld ground flush, $\Delta\sigma = 250\text{MPa}$	28
Table 5.2	Ratio of bending to axial stress weld profile machined and fully ground condition.....	29
Table 6.1	SN DATA – RMI PIPE GRADE 29 – WELDED SPECIMENS – 1G (Constant amplitude loading).....	50
Table 6.2	SN DATA – RMI PIPE GRADE 29 – WELDED SPECIMENS – 5G (Constant amplitude loading).....	51
Table 7.1	Development of the fatigue process for initiation from defects and initiation from surface (PSB).....	64
Table 8.1	Interaction of flaws, from BSI PD 6493 (1991).....	66
Table 8.2	Fatigue and geometry data for surface defects.....	87
Table 8.3	Fatigue and geometry data for surface initiation (PSB).....	87
Table 8.4	Fatigue and geometry data for internal defect.....	88

NOMENCLATURE

LATIN SYMBOLS

A	Area, point on 6 o' clock position of the elliptical crack
B	Point on 12 o' clock position of the elliptical crack
C	Material constant, point on 3 o' clock position of the elliptical crack
D	Diameter, point on 9 o' clock position of the elliptical crack
E	Elastic modulus
F	Form factors
K_{IC}	Fracture toughness
K_{ISCC}	Fracture toughness in sea water
M_1	Magnification correction factor for front surface
M_2	Magnification correction factor for back surface
M_A	Magnification correction factor for point A
M_B	Magnification correction factor for point B
M_C	Magnification correction factor for point C
M_D	Magnification correction factor for point D
N	No of cycles to failure
R	Stress ratio
S_a	Axial stress
S_a^{LC}	Measured stress range (load cell reading)
S_a^{SG}	Measured stress range (strain gauge reading)
S_b	Bending stress
S_m	Mean stress
S_{\max}	Maximum stress level
S_{\min}	Minimum stress level
S_u	Ultimate stress
S_y	Yield stress
Y_m, Y_b	Geometric function for membrane and bending load
a	Half crack length
a_1	Crack length for crack 1
a_2	Crack length for crack 2

b	Half crack depth
b_1	Half crack depth for crack 1
b_2	Half crack depth for crack 2
d_1	Distance between elliptical crack from the centre to the front free surface
d_2	Distance between elliptical crack from the centre to the back free surface
da	Crack length increment
db	Crack depth increment
dN	Incremental no of cycle
e, e_1, e_2	Separation distance between two cracks either in the depth or length direction
m	Material constant
t	Thickness

GREEK SYMBOLS

$\Delta\sigma$	Applied stress range
ΔS	Applied stress range
ΔS_o	Stress range at a given fatigue life under reversed loading
ΔK	Stress intensity factor range
ΔK_{th}	Threshold stress intensity
ΔP	Applied load (KN)
σ_m	Mean stress
ϕ	Angle on the elliptical crack
Φ	Ellipticity correction of the second kind
λ	Ratio of crack depth/crack distance from centre to front free surface or back surface
μ	Aspect ratio

ABBREVIATIONS

GTAW	Gas tungsten arc welding
LEFM	Linear elastic fracture mechanics
PE	Paris – Erdogan
MAAW	Manual argon-arc welds
TIG	Tungsten inert gas
FEA	Finite Element Analysis
Dob	Degree of bending
Ru	Ruthenium
ASTM	American Society for Testing and Materials
SN	Stress range – number of cycles (SN – curve)
BSI	British Standard Institutions
SCC	Stress corrosion cracking
UTS	Ultimate tensile strength
RMI	US supplier of titanium
ELI	Extra low interstitial
<i>Mises@C</i>	Von mises stress at the centre of the weld
$S_{33} @ C$	Axial stress at the centre of the weld
<i>Mises@T</i>	Von mises stress at the toe of the weld
$S_{33} @ T$	Axial stress at the toe of the weld
<i>Mises@10</i>	Von mises stress at 10mm away from toe of the weld
$S_{33} @ 10$	Axial stress at 10mm away from toe of the weld
LVDT	Linear variable differential transformer
SEM	Scanning electron microscope
PSB	Persistent slip bands
SE	Semi-elliptic
RC	Re-categorised
MO	Multi-origin
SB	Surface breaking
CS/EF	Coplanar surface and embedded flaw
CP	Clusters of pores

1 INTRODUCTION

1.1 Background and Objective

With the depletion of onshore and shallow offshore reserves of most petroleum exporting countries, most industry has to grapple with challenges for increasing oil and natural gas production from deep or ultra deepwater's.

Mostly the new challenges have required new technological solutions to be found, either by adapting already existing technologies or by developing new alternatives to make exploration possible in a severe environment.

In recent years, the offshore industries have been pressed to develop new technological and cost effective solution for the riser pipe materials that can thrive well in extremely adverse conditions.

Such riser material should satisfy high specific strength, good corrosion resistance, and high temperature /pressure requirements. The limitations exhibited by steel in severe applications have been a subject for considering titanium as a riser material.

With the advent of deep-water exploration and exploitation, titanium has been identified with desirable attributes and low life cycle cost for riser systems (Fisher et al., 1990).

An important design consideration for critical girth welded components for a deepwater application (e.g. titanium riser) is fatigue. In general, risers are subjected to significant loading. Well-established properties of structural grades of titanium relating to extreme loading; i.e. tensile strength and ductility existed. However, the fatigue properties of heavy section girth welds, which are required for manufacture of pipe, are less known (Berge, 1998a).

To this end, effort is geared towards establishing an improved basis for fatigue design of titanium risers.

1.2 Scope of Work

The ultimate fatigue performance of a weld is greatly influenced by specifics of a weld procedure, the weld alignment, quality of the weld root pass, internal weld flaws and the temperature history during welding.

One of the means of improving the fatigue performance at the weld reinforcements is by grinding, such that the internal and outside diameter of the weld profile is flushed with the pipe walls to eliminate the weld toe defects.

For a large diameter riser, access to internal and outside diameter is possible, hence surface weld defects can be eliminated by grinding. Fatigue strength of such weldment is controlled by internal defects e.g. pores, slag inclusion, lack of side-wall fusion etc.

This study is centred on assessment of the fatigue strength of titanium fusion welds for deep-water riser's applications.

Distinctively, three main topics were covered: Fatigue testing, Fractography and defect assessment, and Fracture Mechanics modelling of fatigue crack growth.

Experimental work at the initial stage included constant amplitude fatigue testing of 6 series of test specimens, with each of the series consisted of 10

specimens were fatigue tested in as-welded condition. Most of the fatigue initiations have been from the surface of the specimens. In some cases, it was difficult to determine the source of initiation of fatigue cracks.

A refined study was carried out with constant amplitude fatigue test of two series of welded grade of titanium consisting of 14 specimens in each series. These formed the backbone of the study. Prior to fatigue testing, strain gauge measurements of few specimens were conducted to enable the definition of stress range in the fatigue assessment procedure. The results have been compared with finite solid element analysis.

Fractography was used to assess the distribution and geometry of internal and surface defects both in as-welded and in post-weld machined conditions. This served as a tool to determine the fatigue initiation point in the welds.

Fracture mechanics was applied to model fatigue fracture strength of titanium welds with initiation from weld defects. Two different stress intensity factor formulations for embedded eccentrically placed cracks were used for analysis of elliptical cracks with major axis parallel and close to one of the free surfaces, namely:

- i. Isida et al. (1984b) parametric equations for stress intensity factors at the point close to the front surface (6 o' clock position) and back surface (12 o' clock position). This was combined with a linear extrapolation of tabulated stress intensity factors presented by Guozhong et al. (1996) for crack tip at long axis of the crack (3 o' clock position).
- ii. Fett et al. (1997) parametric equations covering any locations on the circumference of the embedded elliptic crack and for any orientation of the embedded elliptic crack.

For elliptical crack with minor axis parallel and close to one of the free surfaces, Isida et al. (1984b) is not valid. However Isida et al. (1984b) was extended. Two models were used, namely; crack rotation and crack enlargement at constant aspect ratio.

The model analyses crack growth of elliptical and semi-elliptical cracks in two directions, with updating of the crack geometry. Fatigue strength assessment was conducted using two crack growth models, the Paris-Erdogan relation with no threshold and Donahue et al. relation with an implied threshold.

The model was validated against experimental data with a discussion on the choice of crack growth model.

1.3 Organisation of the Thesis

Chapter 2 provides a theoretical understanding on application and performance characteristics of welded Titanium alloys as a candidate for deep-water risers. Chapter 3 described the basic material properties for this study. Relevant welds processes and associated weld defects are the subject of Chapter 4. Chapter 5 and 6 present a series of static and fatigue tests on TIG welded Titanium specimen respectively.

Chapter 7 and 8 dealt with the fractographic investigation of fatigue fracture surface to determine the fatigue initiation point in the welds. Chapter 9 focussed on the characterisation of crack growth in terms of the stress intensity factor. Chapter 10, 11 and 12 presented fracture mechanics as a tool to solve fatigue-related problems. Summary and general conclusions were given in Chapter 13.

2 TITANIUM RISERS

2.1 Applications

In general marine risers are used to transport fluid or gas between a floating production system and the seafloor. Predominantly, marine risers are of tensioned and compliant types which are grouped according to their applications, cross-sectional properties etc.

Tensioned riser

Tensioned marine risers include drilling risers, production, export and workover risers. Mainly, they have a top tension that provides lateral stiffness and must therefore be heave compensated (Carlsen, 1998). For example, in a tension leg platform (TLP) riser system, each riser can be considered as a slender beam member supported and tensioned at the TLP, and reacted at the anchor point of the subsea wellhead (Simonsen et al., 1999).

Current and waves act on the hull and wind on the topside to cause TLP offsets, the restoring forces are provided by tethers. This effect induces fatigue loads into the riser.

Compliant riser

Compliant risers have been designed in order to avoid tension control and heave compensation and are thus suitable for floating platforms system. Compliant risers are applied as production and export risers, also as jumpers and on-bottom flowlines.

Compliant risers may be:

- Nonbonded flexible type
- Metallic, at large water-depth

A main problem for such risers is to avoid excessive bending deformations. Ideally, the cross section should have low bending stiffness, high axial and torsional stiffness, high radial stiffness when exposed to external or internal pressure. Usually bending overload at terminations is prevented by engineering solutions e.g. using flexjoint, taper stress joint etc.

Titanium has been considered for riser application, especially for severe conditions (ultra deep water, high temperature, high-pressure applications or where large diameters are required) where titanium has favourable properties compared to nonbonded flexible risers (Grealish et al., 1999).

Of relevance in the design of titanium riser are the design criteria for extreme response stresses (tension, upper end rotation etc.), hoop stress from internal and external pressure, buckling, collapse and fatigue. In this study emphasis is on fatigue properties of titanium welds.

2.2 Performance Characteristics of Titanium for Riser Application Compared to Steel

High strength to weight ratio

Titanium alloys offers superior strength to weight ratios to other metallic alloys. For example, when compared to steel alloy, Titanium Grade 5 at 20° C has a strength to weight ratio of 188MPa/Kg, while a stainless steel 13% Cr – AISI 410 has a strength to weight ratio of 45MPa/Kg (Peacock, 1999).

Depending on the type of riser, application or geometrical configuration, the relative weight could either be a benefit or a design problem.

Benefit:

- Reduction in the top tensioner requirement due to lighter weight.
- Significant reduction in loads on the subsea connector can be achieved

Design problem (e.g. catenary and wave type configurations)

In a catenary and wave type configuration risers where buoyancy is an important parameter in design, it is necessary to design systems to improve the stability and response characteristics of titanium risers. Mainly because titanium risers are buoyant in empty conditions, technical solutions such as attachments of clump weight or application of weight coating are needed to achieve the required stability for the dynamic response.

Stiffness

Titanium has a low elastic modulus with a stiffness of about 50% compare to steel. The implication is that a pipe with unsupported free spans may be subjected to higher strain compared to steel, since it can tolerate higher deflection before yielding. Buckling strength may be critical because of the low stiffness.

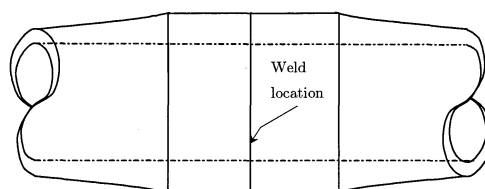


Figure 2.1 Thick – end riser joint concept. The outer diameter of the pipe is increased locally at the weld.

Fatigue

Fatigue characteristics of titanium is better compared to steel, in some cases a factor of two difference in the number of cycles to failure could be achievable (Grealish et al., 1999).

Fatigue damage in titanium risers are caused by wave loads and associated vessel motions (first order effects), second order slow drift vessel motions, vortex induced vibrations and during installation etc.

There are different fatigue critical regions for different types of riser. For a metallic catenary riser, two fatigue critical regions exist, in the touchdown zone and at the upper end.

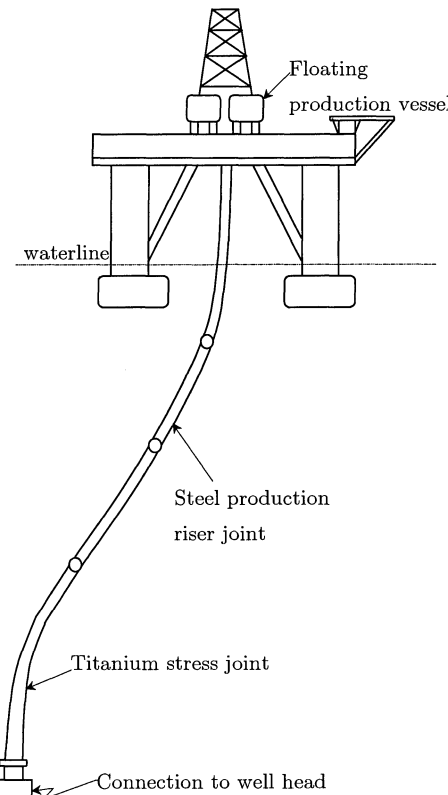


Figure 2.2 Connection of a riser to a floating production system. Typical application for a titanium stress joint.

Welded joints tend to be weak links with regard to fatigue design. To improve the fatigue life of a riser pipe the wall thickness of the pipe may be increased at the end of each joint (Figure 2.1) to reduce the bending stress at the girth weld between adjacent sections. Despite the thickening of the pipe wall, the global stiffness or the moment distribution is not affected since the pipe is thickened only at discrete locations (Newberry, 1998).

Titanium has a better fatigue performance compare to steel. This may be utilised in applications where thick walled and highly stressed parts are required (Grealish et al., 1999). Titanium is particularly favourable in displacement controlled loading, which is generally the case for risers. Due to the low modulus of elasticity, curvature variations give significantly less dynamic stress in a titanium pipe compared to a steel pipe.

Connection of riser to a floating system

Using a flexjoint

The flexjoint accommodates the upper end rotation of a riser while still maintaining the flow path. With steel metallic risers for a TLP, flexjoints are in general required. Titanium offers reduced weight, reduced tension requirements and topside loads as well as the elimination of flexjoints (Simonsen et al., 1999).

Using a tapered stress joint

The taper stress joint can be used to connect the riser to the floating system and can also serve as a means of connecting the riser to the top of the sub sea wellhead connector (Figure 2.2) to reduce local bending stress and to provide flexibility.

Compared to a flex joint, stress joint offers a potential cost saving alternative for small size risers in situations where the maximum top rotation during the extreme loading event is small (Allen et al., 1998).

The use of steel will give excessive joint length. Titanium taper stress joint coupled directly to steel has been used e.g. on Placid Oil's Green Canyon (Herman, 1991), Neptune Field spar platform in the Gulf of Mexico (Baugus et al., 1998) and Heidrun platform (Lunde, 1999). When titanium is coupled to a less noble and active material like steel, it may be necessary to protect the material from galvanic attack.

Corrosion characteristics

Steel riser is exposed to potential internal corrosion due to well flow containing H_2S and CO_2 . Carbon steel needs to be protected against H_2S and CO_2 by use of a corrosion resistance liner.

Titanium alloys offer superior corrosion and erosion resistance especially in solid free or silt laden seawater flow (depending on the flow velocities), marine and hydrocarbon production environments.

Cost

Production cost for titanium risers is quite high compare to equivalent steel risers. However, in recent years improved production efficiency and capacity have lead to decline in the price of the product (Schutz, 1991). It becomes justifiable to utilise titanium as a riser material because of the low life cycle cost.

There are low cost penalties associated with maintenance and downtime with the usage of the product. Importantly, available effective welding techniques and fabrication methods has made titanium components and structures more practical and cost effective (Fisher et al., 1990).

3 BASIC MATERIAL PROPERTIES

3.1 Pipe Materials

The present work was linked to a joint Industry Project in which a range of titanium pipe and welds were fatigue tested. The titanium pipes for the test program are shown in Table 3.1.

Table 3.1 Grades of pipe material taken as dog-bone coupon specimens from the pipe wall.

Series	Material	Weld type
R01	ASTM Grade 28	1G
R03	ASTM Grade 29	1G
R05	ASTM Grade 28	5G
R08	ASTM Grade 29	5G
RA41	ASTM Grade 23 + Ru	1G
RA42	ASTM Grade 23 + Ru	5G
AS	PT-3V (Russian grade)	1G
BS	PT-3V (Russian grade)	1G

All grades were medium to high strength alloys with 4 – 6% Al and 2 – 4% V, in the ELI (extra low interstitial) condition. These grades are considered to be the prime candidates for riser applications.

The pipes were seamless, produced by the pierce-roll method, with diameter in the range 100 – 200mm and wall thickness 10 – 20mm. The pipes were girth welded as shown in Table 3.1, with TIG (Tungsten Inert Gas) welding.

Each of the series consisted of 10 specimens, taken as dog-bone coupon specimens from the pipe wall. All of the series had been fatigue tested in as-welded condition except for RA41 and RA42 series, which had some of the specimens fatigue tested in the machined and profile ground condition. Initiation of fatigue cracks was in some cases from the surface of the specimens, in some cases from internal defects. In some cases it was difficult to determine the source of initiation of fatigue cracks.

3.2 Chemical Composition

Generally, alloys are described generically by their metallurgical structure. Titanium alloys are classified in three main groups, alpha, alpha-beta and beta depending on the heat treatment and interstitial (primary oxygen) content. Alpha and beta alloy composition, are the two main crystalline structures in the solid phase. Alpha is closely packed hexagonal (CPH) structure. The body centred cubic (BCC) structure is termed as beta. Alpha-beta is a combination of alpha and beta grains.

Beta is stable at room temperature only if it is enriched with more than 15 wt. % vanadium (Boyer et al., 1994). Alpha phase is stabilised by addition of aluminium. By varying the alloy composition combined with heat treatment, microstructures with favourable properties may be developed.

3.3 Properties of Titanium Alloy

Near-alpha, and alpha-beta alloys have lower to intermediate strength with good crack growth resistance. Near-beta and beta alloys are high strength alloys which in general exhibit reduced crack growth resistance.

ASTM Grades 23 and 28 are lean alpha-beta (near-alpha) alloys of medium strength, with reduced oxygen content (ELI - extra low interstitials) for enhanced toughness and ductility. The alloys are somewhat susceptible to crevice corrosion and stress corrosion cracking in sea water at elevated temperatures (above 80 – 90° C). Small additions of Ruthenium or Palladium gives Grades 29 or 24, for improved corrosion resistance (Grauman, 1999).

The favourable properties of titanium alloys have made it a potential choice for a wide range of applications in the oil and gas industry. Such properties include lower density compare to other corrosion resistant alloys, low modulus and high strength.

Table 3.2 Key properties of Ti-6Al-4V ELI (Peacock, 1999)

Ti-6Al-4V ELI. Grade 23 or 29								ρ $\left(\frac{Kg}{m^3}\right)$	
Alloy type	0.2% proof stress (MPa)	UTS (MPa)	Strain (%)	TM (MPa)	TOM (MPa)	Toughness ($MPa.m^{\frac{1}{2}}$)			
						K_{IC} (air)	K_{ISCC} sea - water		
Alpha	760 –	830 –	10 –15	110 –	40-43	85-110	75-90	4.42	
-beta	900	1000		115					

UTS: Ultimate tensile TM: tensile modulus
strength TOM: torsion modulus

Density

The lower density of Titanium alloy has given it a unique property of higher strength to weight ratio compared to other corrosion resistant alloys. In relation to structural or pipeline steels, the strength/weight ratio of titanium is a factor 3 – 4 larger. The implication is that considerable weight savings may be obtained, especially where design for minimum weight is critical. This is the case for floating production platforms, where buoyancy may carry a significant cost factor.

Low modulus of titanium alloy

Dynamic

Risers are subjected to displacement controlled loading. The dynamic stress in a titanium riser, due to the lower modulus of elasticity, is thus 50% of the stress in a corresponding steel riser. In fatigue analysis, this provides a very large improvement in fatigue strength, based on the usual SN curve formulation.

A titanium pipe may be bent to a curvature which is 3 – 4 times the curvature of a steel pipe with the same diameter, under elastic conditions. This is also a favourable property for riser applications, allowing various configurations with buoyancy elements to minimise dynamic stress.

Corrosion resistance

The resistance to corrosion of Ti-6Al-4V alloy is obtained from the highly spontaneous formation of a thin (50-200Å) transparent, adherent, stable, tenacious surface oxide film, primarily TiO_2 (Equation (3.1)). If oxygen is present, which is the case in air and in seawater, the oxide film can re-heal itself instantaneously when mechanically damaged.

In water the reaction can be described by



Titanium can resist solid-free seawater flow to velocities as high as 30m/sec, and to silt-laden seawater erosion to at least 5-6m/sec due to its protective oxide coatings (Schutz, 1991).

4 WELDING

4.1 Welding processes

In welding technology, a large number of processes have been developed. For titanium riser applications, two processes have been investigated, the fusion welding and the pressure or friction welding processes.

4.1.1 Pressure welding processes

With pressure welding processes joining is achieved through externally applied forces. The pressure welding processes could be further subdivided into solid state and pressure fusion groups. Gas pressure and friction welding (radial friction and rotary friction welding) are examples of solid state welding processes. Examples of pressure-fusion processes are resistance-spot and resistance-seam welding (e.g. Davies, 1989).

Rotary friction welding

Frictional heat is generated through contact between a rotating pipe and a stationary pipe. Presently two main methods exists to achieve this, firstly the rotating pipe can be driven by a motor and brake when a forging pressure is applied. Lastly, the rotating pipe may be attached to a flywheel while the stationary pipe provides the inertia force to brake the system (Smith et al., 1999).

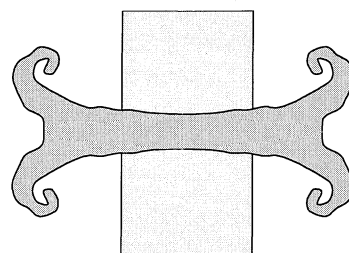


Figure 4.1 Rotary friction weld (schematic), with excess material which needs to be machined off.

Limitations arise for very long lengths of pipe because the speed of rotation decreases as the length of the pipe increases.

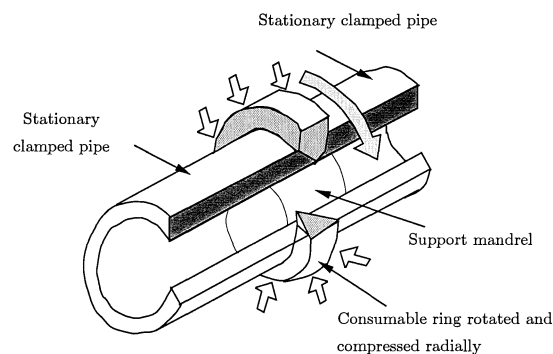


Figure 4.2 Radial friction welding principle.

Radial friction welding

This welding process offers a cost-effective technology to produce high quality welds in high strength titanium alloys. Two sections of pipe are stationary clamped while a consumable ring is rotated and subjected to a radial compressive pressure to provide the frictional interaction between the ring and the pipe surfaces, Figure 4.2. The heat resistant mandrel acts as support against collapse for the consumable ring and the pipe (Hutt et al., 1999). The need to rotate long length of pipe is eliminated in radial friction welding technique.

4.1.2 Fusion welding processes

Fusion welding process is the most common form of welding load-bearing steel structures. Joining is achieved through melting and solidification. No external force is applied, other than to stabilise the components to be welded.

Various forms of fusion welding techniques for joining Titanium are TIG welding (Tungsten inert gas), Plasma welding, Vacuum or Reduced pressure electron beam welding, Laser welding etc.

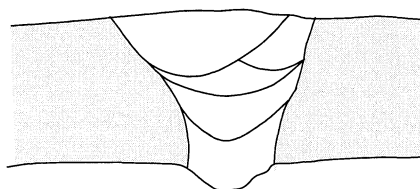


Figure 4.3 Schematic representation of a multipass TIG weld.

TIG welding, also called gas tungsten arc welding (GTAW) is the most common form of joining technique for titanium. The method can be applied in any position, and for virtually any thickness. The problems associated with TIG welds are as follows:

- The process is slow and many passes must be made to fill this joint (Figure 4.3). For mass production the method is expensive.
- Solidifying weld metal gives coarse grained structure with a grain size roughly proportional to the number of passes.
- The coarse grains can increase the difficulty in detecting small defects using ultrasonic inspection techniques.
- The TIG welding process tends to leave pores, typically of size 0.5 – 1.0mm, in the root region. These pores are detrimental to fatigue strength.

A clear advantage for TIG welds is that mechanical properties other than fatigue strength compare favourably with those of the base material despite the coarse grain size.

Broadly, the procedure for Plasma welding is similar to TIG welding, Heat input is much larger, and one-pass welding of plate thickness up to 12 – 14mm is possible. Plasma welding is thus more economical. For pipe welding, the method needs more development due to the problem of closure of the weld.

Reduced pressure electron beam is performed in a partial pressure of helium. The main advantage over vacuum electron beam welding is that it is suitable for welding large pipelines. Satisfactory welds up to 16mm thickness can be made in titanium pipes (Smith et al., 1999).

Laser welding can be successfully applied to titanium alloy. When the beam is focused into a small spot and there is sufficient energy, welding, cutting and piercing operations can be performed.

4.1.3 TIG fusion welding

In the present study, welds were tested from pipes which had been welded in two positions; namely 1G welds and 5G welds on extruded RMI Grade 23 + Ru. For 1G welds, the welding of the joint is done in the flat position, i.e. the pipe is rotated while the welding torch is stationary. The advantage here is that the weld pool can be controlled quite easily.

5G welds are made by a different technique. The pipe is fixed while the welding torch is rotated orbitally. Making such welds require vertically downward welding whilst welding from 12 o'clock to 6 o'clock, Figure 4.4. An obvious drawback is the difficulty in control of large weld pools due to gravitational pull.

Generally, the strength and ductility seems to be somewhat better for the 1G welded procedure when compared with 5G weld (Ødegård, 1998).

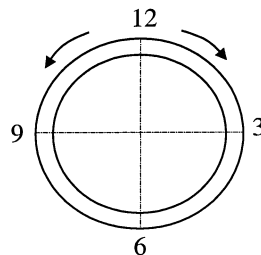


Figure 4.4 Vertical downward technique, welding from 12 o'clock to 6 o'clock in multiple runs

4.2 Weld Defects

Weld defects are inevitable in fusion welding processes. Such weld defects are porosity, lack of fusion, non-metallic inclusions, undercut, lamellar tearing, hot cracking etc.

For TIG welds in titanium alloys, the most common defects are lack of fusion and porosity. Weld defects may be detrimental to fatigue strength. Other effects of welding which could affect fatigue strength are poorly finished surfaces, or presence of sharp transitions, unblended radii and corners.

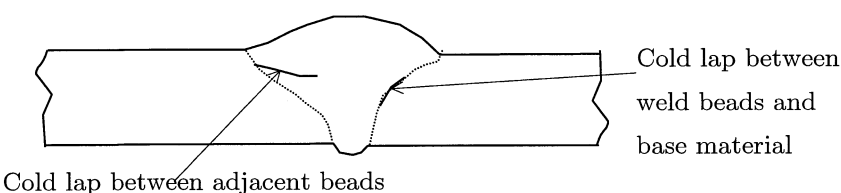


Figure 4.5 Lack of fusion due to cold lap

Lack of fusion defects

Lack of fusion refers to a condition in which the interface between adjacent weld passes or between the weld and base metal has not been melted, Figure 4.5. The causes is insufficient application of heat to raise the temperature of the base metal to the melting point.

There is very few data available for lack of fusion defects. In the present work defects were found with a crack length up to 6mm with crack depth of about 0.2mm.

Porosity

The presence of pores in welds is termed porosity. The influence of pores (Figure 4.6) close to the surface in TIG welds may contribute significantly to lower the fatigue strength. Moreover, regardless of size, weld pores are potential sites for fatigue initiation provided other weld defects and geometry-specific stress raisers are absent.

From the data in the present study, the most common shape for such defects is elliptical with size ranges 0.2 – 0.6mm. Pores may also be elongated or irregular in shape.

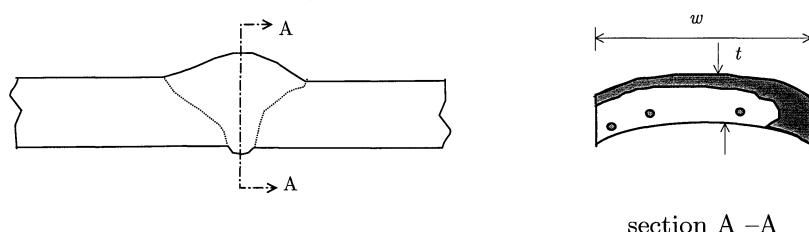


Figure 4.6 Pores due to presence of hydrogen during welding. The grey area is the final fracture zone.

The primary cause for the pores is hydrogen, formed by dissociation of water during the welding process (Smith et al., 1999). Titanium oxide is highly hygroscopic, and adsorbed water tends to be present.

Smith et al. (1999) proposed that thorough cleaning of the joint surface before welding, machining without aqueous lubricants and welding in the same 24h period are advised as means for preventing porosity. Furthermore, application of autogenous TIG dressing passes over the completed root weld surface is a simple method to counter porosity.

5 STRESS DISTRIBUTION ACROSS THE FUSION WELD

In the fatigue tests the nominal applied stress was axial. Due to the shape of the specimens, significant secondary bending stresses were present. In order to apply fracture mechanics analysis, the stress distribution through the specimen thickness was analyzed experimentally and by finite element analysis.

5.1 Specimens

The specimens were produced in accordance with ASTM E466 Recommended Practice for constant amplitude axial fatigue tests of metallic materials with dimensions given in Figure 5.1(c). A procedure known as water jet cutting was applied. This machining method leaves a satisfactory surface with no heating or residual stresses (Berge, 1998).

Post weld preparations

The specimens were supplied in the as-welded condition. Post weld preparations included cold grinding, and machining as shown in Figure 5.1a.

Root grinding

The roots (inner side of the weld) of 2 specimens were ground smooth with a portable hand held grinder. A special grinder was used to avoid any heating to the titanium surface. Heating could lead to oxidation and possible formation of brittle α -case on the surface.

Weld profile grinding

The weld profile for 8 specimens was cold machined using a rotary grinder. The use of portable hand held grinder with a smooth abrasive provided the inner and the outer side of the weld with good surface finish.

5.2 Experimental

Strain gauge locations

The locations of strain gauges in the vicinity of the weld was as indicated in Figure 5.1(a). One strain gauge was fixed at the center of the fusion line on the inner surface (strain gauge 3). Strain gauge 2 was attached at the inner surface at a distance of 10mm from the toe of the weld. Strain gauge 1 was fixed on the opposite side of Strain gauge 2 but at the same distance from the toe of the weld.

Measurements

Prior to connection of the strain gauges to the strain meter (Wheatstone bridge), the zero level of the strain meter was checked.

One end of the specimen was clamped in the grips of the hydraulic actuator. The strain gauges were connected to the strain meter and the strain reading was balanced to zero before clamping the opposite end of the specimen. With the load level set to zero the strain after clamping was noted. In all cases the measured value was below $20\mu\text{S}$. The gauges were then re-zeroed.

The specimens were tested at two stress ranges with $\sigma_m = 200\text{MPa}$, $\Delta\sigma = 250\text{MPa}$ and $\Delta\sigma = 300\text{MPa}$ (Chapter 6).

5.3.1 Root ground specimens

As shown in Table 5.1 the root ground specimens had secondary bending which was 17 and 11 percent of the axial stress respectively. The secondary bending was tensile at the root side. The reason for the secondary bending is two-fold. Due to the shape of the coupons, the neutral axis of the specimens is slightly curved, giving tensile stress at the root side. Furthermore, the one-sided weld reinforcement contributes to the same effect. Possible misalignment of the weld or of the test machine could be a cause for the scatter.

S_a^{LC} was the stress calculated at section $A_1 - A_1$ from the load cell reading. S_a^{SG} was the stress measured by strain gauges in the same cross section. The deviation between S_a^{SG} and S_a^{LC} is insignificant, and confirms the strain measurements.

Table 5.2 Ratio of bending to axial stress weld profile machined and fully ground condition

Specimen	A (mm ²)	ΔS_a^{LC} load cell	ΔS_a^{SG} strain gauge $A_1 - A_1$	ΔS_a^{SG} strain gauge $A - A$	S_b	$\frac{S_b}{S_a^{LC}}$	$\frac{S_b}{S_a^{SG}}$
Section $A_1 - A_1$							
Ra41/4	184	223	225	251	45	.20	.20
Ra41/6	186	224	217	245	32	.15	.15
Ra41/7	197	207	190	227	23	.11	.12
Ra41/8	184	223	226	252	17	.08	.08
$\Delta\sigma = 250\text{MPa}$							
Ra41/9	194	254	246	289	18	.07	.07
Ra41/10	194	254	251	295	45	.18	.18
$\Delta\sigma = 300\text{MPa}$							
Ra42/6	193	254	239	280	14	.06	.06
Ra42/8	195	254	237	281	8	.03	.04

5.3.2 Machined and ground specimens

The strain measurements for specimens which had been machined and ground flush are shown in Table 5.2.

The ratio of bending stress to the axial stress measured with strain gauges was within 7 – 20% with an average of 13% for RA41 series specimen. RA42 series shows 3 and 5% ratio of bending stress to the axial stress.

There is no significant difference between secondary bending for machined specimens and for specimens with the weld overfill intact. Random misalignment appears to contribute to the secondary bending even more than the effects of weld overfill.

5.4 Finite Element Analysis

A three dimensional finite solid element elastic stress analysis was used to calculate the stress distribution at the weld across the thickness of the pipe. The model was a coupon cut from a pipe of nominal thickness of 10.3mm and outside diameter of 242.7mm Figure 5.1(c).

An average thickness of 9.45mm was recorded on the test specimens and was used in modelling the geometry. Nominal thickness of 10.3mm was used for the true dimension of the pipe.

Four types of models were analysed which represent; as-welded condition, machined and ground, true dimension of the pipe in the as-welded condition and a plain pipe without weld.

Pre-processing, numerical computation and post processing of the models were carried out using ABAPRE (ABAQUS/Pre 5.7-1), ABAQUS standard and ABAQUS/Post (Hibbit et al., 1998).

The weld zone, heat-affected zone, and the loading part were partitioned into 4 solids and discretized into 8 node Hex. Solid element (type C3D8).

5.4.1 Boundary conditions and applied loading

Symmetry conditions allowed a quarter part of the specimen to be modelled. Symmetry boundary conditions were applied along section $A - A_1$ and section $A - A$ symmetry line (Figure 5.1b, Figure 5.9, Figure 5.17).

The displacement boundary condition on the loading end was fixed on all translational degrees of freedom except in the loading direction, which means the clamped surface cannot contract laterally. This introduces a small error at the loading end since in reality the clamped surface could contract with the clamps held on to the surface.

A force equivalent to 1Mpa stress was distributed on the loading surface, and shared between the corner nodes, the remaining nodes on the 4 edges, and the middle nodes in the ratio of 0.25:0.5:1 respectively, corresponding to the area on which the forces act.

From the finite solid element analysis, the components of stress in other directions than the tensile axis were negligible, only uniaxial stress would be assumed to contribute to fatigue damage. Hence, the subsequent finite solid element analysis figures were presented with the von-Mises stress and the stress component in the loading direction.

5.4.2 As welded condition – test specimen

In Figure 5.2 is shown the stress distribution through the plate thickness at section A-A (@C). In Figure 5.3 is shown the distribution at the toe of the weld, and in Figure 5.4 at section $A_1 - A_1$, 10mm from the toe of the weld (@10). In Figure 5.5 is shown a contour plot of the axial stress in the specimen. S_{33} and Mises indicated in Figure 5.2 - Figure 5.4 are the axial stress and von-Mises stress in the specimen.

As shown by the plots, the presence of a weld profile has a significant effect on the shape of the stress distribution, with increased secondary bending.

The stress distributions at the toe of the weld and at section $A_1 - A_1$ are quite similar, apart from the local stress concentration at the toe of the weld. The secondary bending stress is 20% of the axial stress at the weld toe, 17% at section $A_1 - A_1$.

The change in gradient of the stress distribution at the toe to distribution at section $A_1 - A_1$ is due to the change in cross-section. The cross sectional area of the specimen increases as distance from the toe increases.

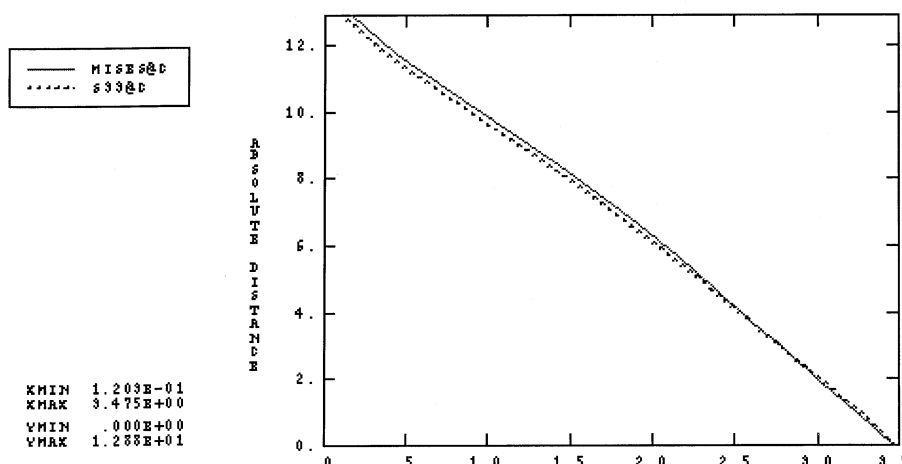


Figure 5.2 Stress distribution through the plate thickness for the as-welded model, at the center of the weld

5.4.4 As-welded condition – full pipe

The coupon specimens are essentially two dimensional, with very little restraint in the direction normal to the pipe wall. Misalignments therefore lead to relatively large secondary bending stress. In a pipe wall, the cylindrical shell gives a radial stiffness which may lead to a much reduced effect of misalignment and weld overfill. For this reason the full pipe was analysed with a finite element model.

The finite element model for the specimen was described in section 5.4.1. Since the full pipe is symmetrical, the same procedure used for specimens was adopted for the full pipe configuration with regard to boundary and loading conditions (Figure 5.17).

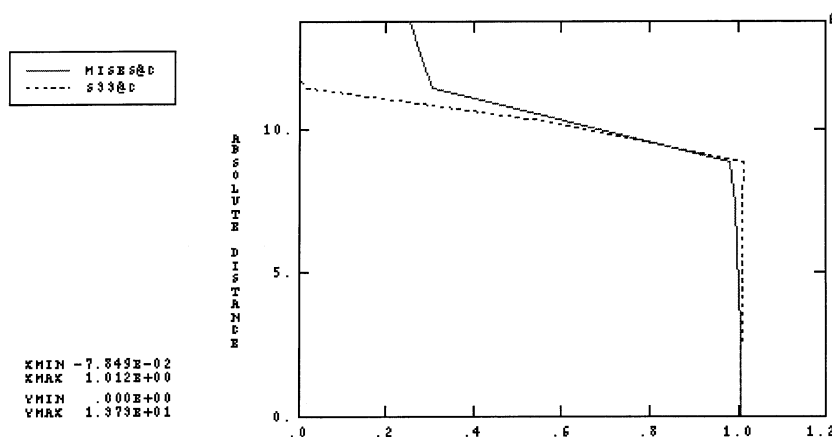


Figure 5.10 Stress distribution through the pipe wall for the as-welded pipe at centre of the weld.

In Figure 5.10 - Figure 5.12 are shown the stress distributions for the full pipe. The change in the distribution close to the through thickness is due to the presence of weld profile. The cross-section stress could be taken as pure membrane. At the toe and at 16mm from the weld toe the stress is purely membrane (Figure 5.11 and Figure 5.12). Through the weld the stress is seen to be strongly reduced through the weld overfill.

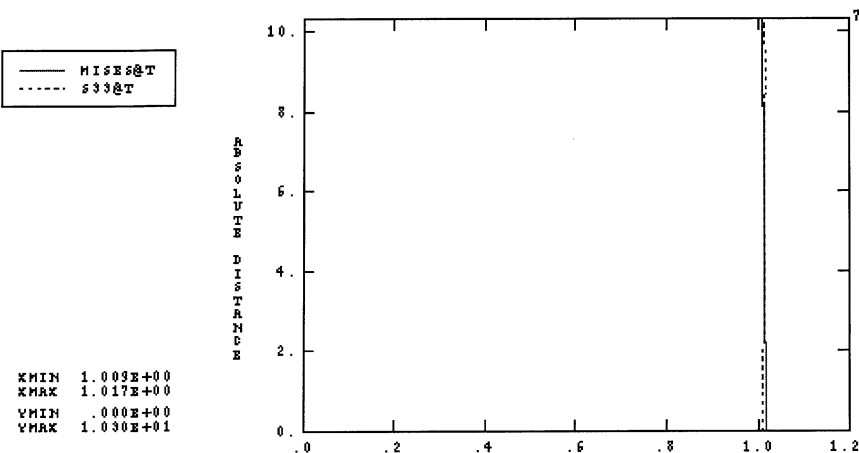


Figure 5.11 Stress distribution through the pipe wall for the as-welded pipe at the toe of the weld.

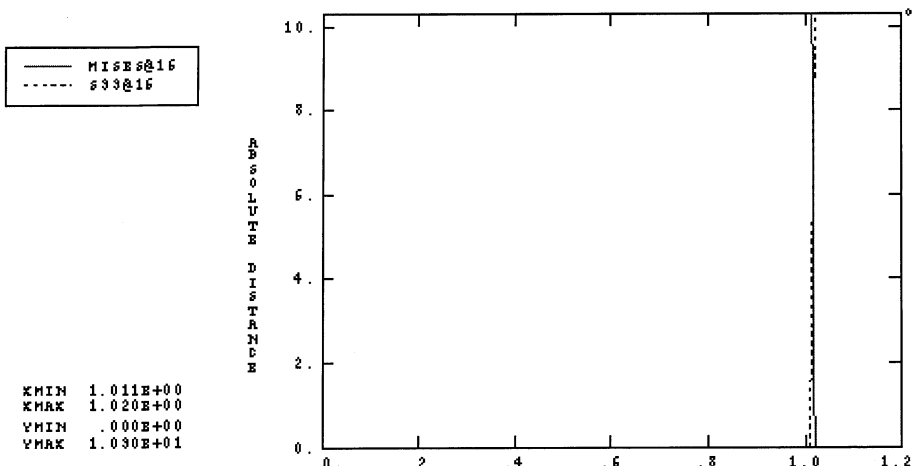


Figure 5.12 Stress distribution for the as-welded pipe in the thickness direction, at 16mm away from the toe of the weld.

From section 5.5.1 and section 5.5.2, there was no significant difference between the observed ratio of bending stress to membrane stress (11% - 19%) going from the as-welded condition to ground and machined condition. As a conclusion, 15% of the applied stress was taken as bending contribution while the remaining 85% was assumed to be membrane components of the applied stress. This result was applied in the fracture mechanics analysis, Chapter 10

6 FATIGUE TESTING

6.1 Mean Stress Level

The effect of mean stress on fatigue life is shown schematically in Figure 6.1.

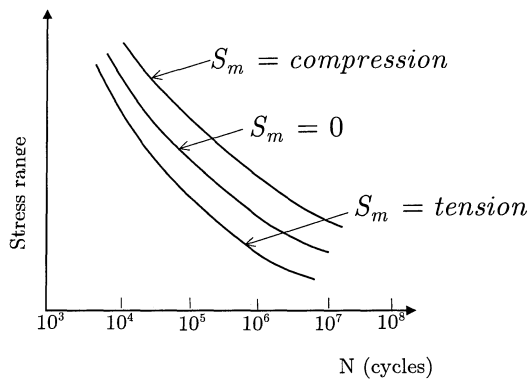


Figure 6.1 Effect of mean stress on fatigue life (Schematic)

$$R = \frac{S_{\min}}{S_{\max}} \quad (6.1)$$

$$S_m = \frac{S_{\max} + S_{\min}}{2} \quad (6.2)$$

The mean stress may also be represented by the stress ratio R, equation (6.1). The relationship between the mean stress and the stress ratio, is given in equations (6.1) and (6.2).

In terms of the stress ratio, the mean stress can be expressed as

$$S_m = \frac{\Delta S}{2} \cdot \frac{1+R}{1-R} \quad (6.3)$$

A dynamic titanium riser will be subjected to an essentially constant mean stress, due to internal pressure, tension and permanent curvature. Based on engineering judgement, the mean stress for constant amplitude fatigue testing of 200MPa was assumed.

Testing was carried out at a stress range of 250MPa and 300MPa. The basis for selecting these levels of stress range was to obtain fatigue failures in the high cycle range. The corresponding stress ratios were R=0.231 and 0.143.

Ruppen et al., (1980) investigated the influence of R ratio (stress ratio) on crack growth rates in an air environment for Ti-6Al-4V alloy. For a constant stress intensity range, crack growth rates increased as the stress ratio increased.

There is a region where the greatest effect occurred (R=0.3 to R=0.5). Increasing the stress ratio further from R=0.5 to 0.7 had little effect on growth rates. The observation suggested that the effect of microstructure on growth rates and fracture topography is enhanced at low R values.

Similarly in a series of testing sponsored by the royal aeronautical society (Engineering science data, May 1982) the effect of stress ratio, R shows that for a given value of ΔK , the larger the value of R the higher is the value of

da/dN . This effect is greatest at low values of da/dN when ΔK approaches the fatigue threshold stress intensity factor.

The effect of mean stress is commonly presented in the Haigh diagram. Various researchers have presented empirical relationship (equations (6.4) - (6.6)) for this effect based on experimental data obtained under different tensile mean stress. Graphically this is represented in Figure 6.2.

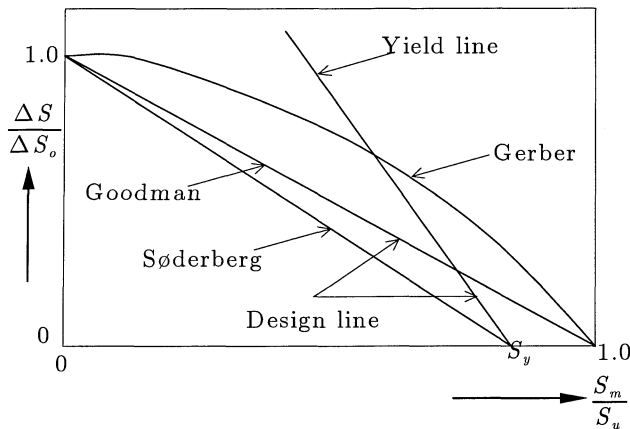


Figure 6.2 Haigh diagram showing the effect of mean stress, and the modified Goodman, Gerber and Søderberg relations.

$$\text{Modified Goodman} \quad \frac{\Delta S}{\Delta S_o} + \frac{S_m}{S_u} = 1 \quad (6.4)$$

$$\text{Gerber} \quad \frac{\Delta S}{\Delta S_o} + \left(\frac{S_m}{S_u} \right)^2 = 1 \quad (6.5)$$

$$\text{Søderberg} \quad \frac{\Delta S}{\Delta S_o} + \frac{S_m}{S_y} = 1 \quad (6.6)$$

ΔS_o is the stress range at a given fatigue life under reversed loading ($S_m = 0$ or $R = -1$). The curves have been derived on the basis of best-fit data generated from experiment under different tensile mean stresses.

It should be noted that tests under constant mean stress will in general yield SN curves which are different from SN curves derived from constant stress ratio, (Figure 6.3).

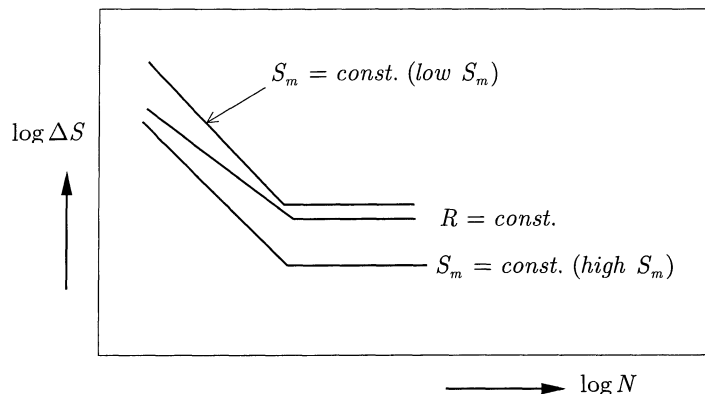


Figure 6.3 Effect of high stress ratio on the fatigue life.

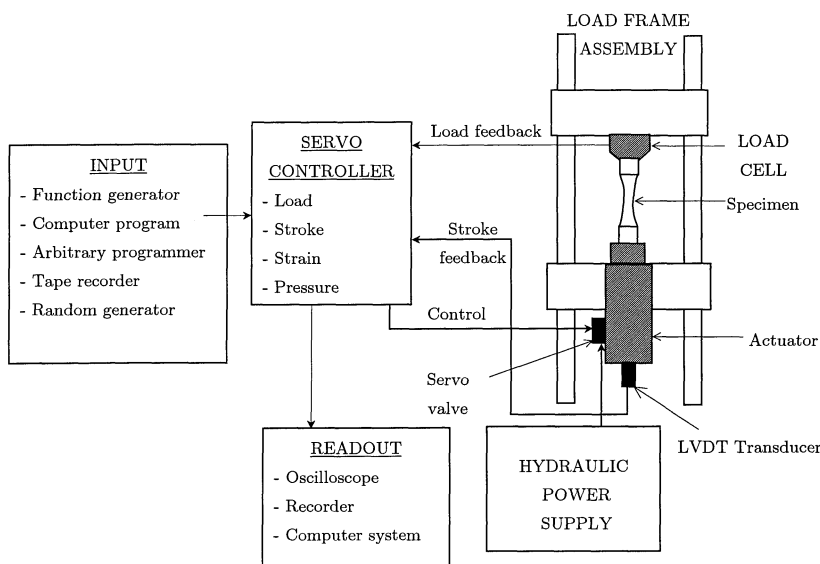


Figure 6.4 Instron closed-loop electro-hydraulic servo controlled testing systems (schematic)

6.2 SN Testing - Experimental

Loading frequency is not an important parameter in fatigue of metallic materials except at high temperatures when there is interaction between creep and fatigue or when corrosion influences fatigue life (Haagensen, 1998).

Fatigue testing in laboratory air was conducted at a frequency of 10 Hz in ambient air. Environmental factors such as atmosphere or seawater, temperature, etc. were not considered in this study.

6.3 Test Equipment

The Instron model 1342 (Figure 6.4) servo-hydraulic actuator powered by pressurised hydraulic fluid system was used to apply uniaxial force to a test specimen under closed-loop servo control. This equipment was used for fatigue testing and strain measurements. The maximum loading parameters for the system are given below:

Static load: $\pm 125\text{KN}$ Dynamic load: $\pm 100\text{KN}$ Stroke: $\pm 25\text{mm}$

6.4 Test Specimen

The test specimens were described in Chapter 5. Fatigue testing was carried out with specimens in the as-welded and in the fully machined and ground condition.

6.5 SN Fatigue Testing

Fatigue test results are presented in Table 6.1 and Table 6.2.

Table 6.1 SN DATA – RMI PIPE GRADE 29 – WELDED SPECIMENS – 1G (Constant amplitude loading)

TEST NR.	ΔS_{nom} (MPa)	Number of cycles	Failure initiation
RA41-1	250	58,796	Surface
RA41-2	150	1,071,524	Surface
RA41-3	100	5,482,600	Run-out
RA41-3	150	415,574	Surface
RA41-4	250	4,387,750	Run-out
RA41-G5	250	-	Overload
RA41-G6	250	531,234	Internal
RA41-G7	250	276,548	Internal
RA41-G8	250	1,479,815	Internal
RA41-G9	300	376,852	Internal
RA41-G10	300	544,789	Internal
RA41-G11	300	315,077	Internal
RA41-G12	250	149,937	Surface
RA41-G13	250	87,896	Surface & embedded flaw
RA41-G14	250	144,352	Surface

Specimen RA41/3 was tested twice, initially at a stress range of 100MPa without failure ($N > 5E6$ cycles), it was tested further at a stress range of 150MPa until failure ($N=415574$ cycles).

The specimens marked with “?” in Table 6.2 were not investigated with electron microscope. It was not possible to identify the location of crack initiation by visual check or with an optical stereo microscope.

Table 6.2 SN DATA – RMI PIPE GRADE 29 – WELDED SPECIMENS – 5G (Constant amplitude loading)

TEST NR.	ΔS_{nom} (MPa)	Number of cycles	Failure initiation
RA42-1	250	97,201	Surface
RA42-2	200	226,298	Surface
RA42-3	150	429,313	Surface
RA42-4	100	4,489,440	Run-out
RA42-G5	300	89,151	Surface
RA42-G6	300	62,058	?
RA42-G7	300	85,188	?
RA42-G8	300	96,884	?
RA42-G9	300	179,014	Surface
RA42-G10	250	592,009	Surface
RA42-G11	250	171,171	?
RA42-G12	250	172,229	Internal
RA42-G13	300	142,033	?
RA42-G14	300	617,857	Internal

The SN data are plotted in Figure 6.5 and Figure 6.6. The RMI design curve is also shown (Baxter et al., 1997)

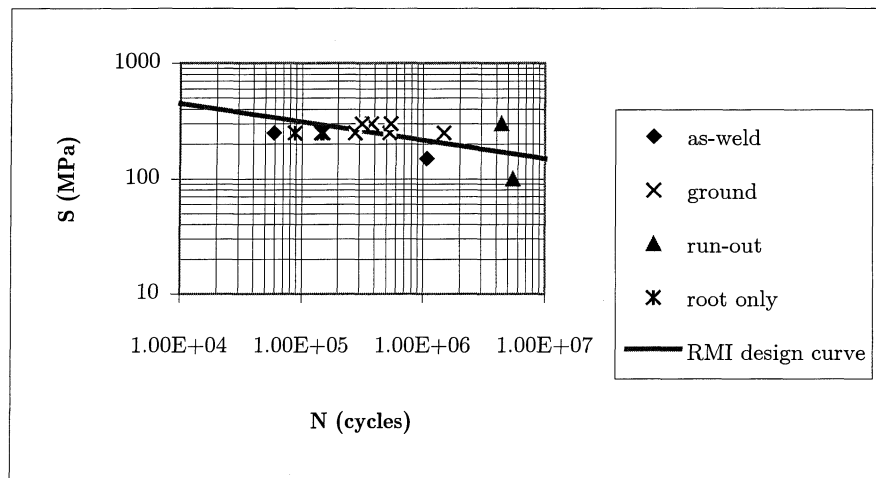


Figure 6.5 SN data for RA 41 series (1G welds). Initiation of fatigue failure for the entire specimen in the ground condition is internal.

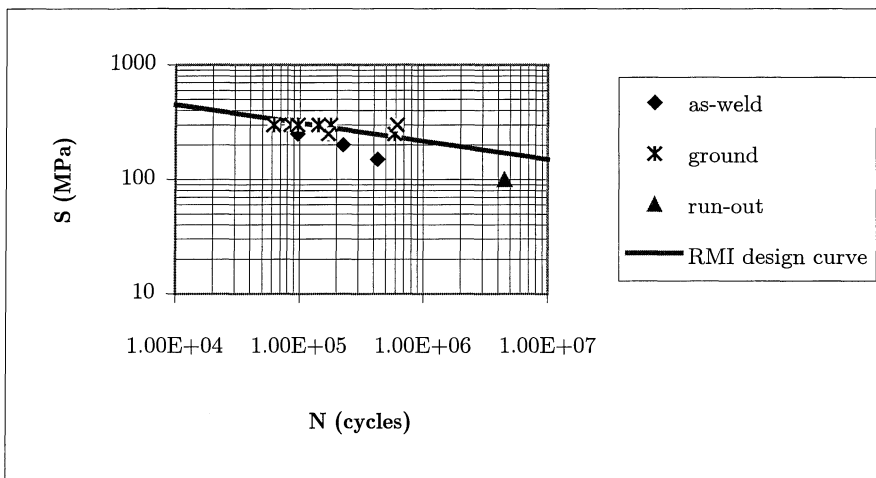


Figure 6.6 SN data for RA 42 series (5G welds). Only two of the specimens (represented with a 'x') in the ground condition had internal fatigue initiation.

7.3 Fractographic Features

Fracture surfaces are characterized by markings or features, which yield information on the initiation and development of a fracture.

Such features are shear lips, chevron markings, bench marks, striations, dimples, feather marks and river patterns amongst others. A detailed description of fractographic features may be found in standard metallurgical textbooks e.g. Colangelo et al. (1987), a brief discussion is given below.

7.3.1 Shear lips

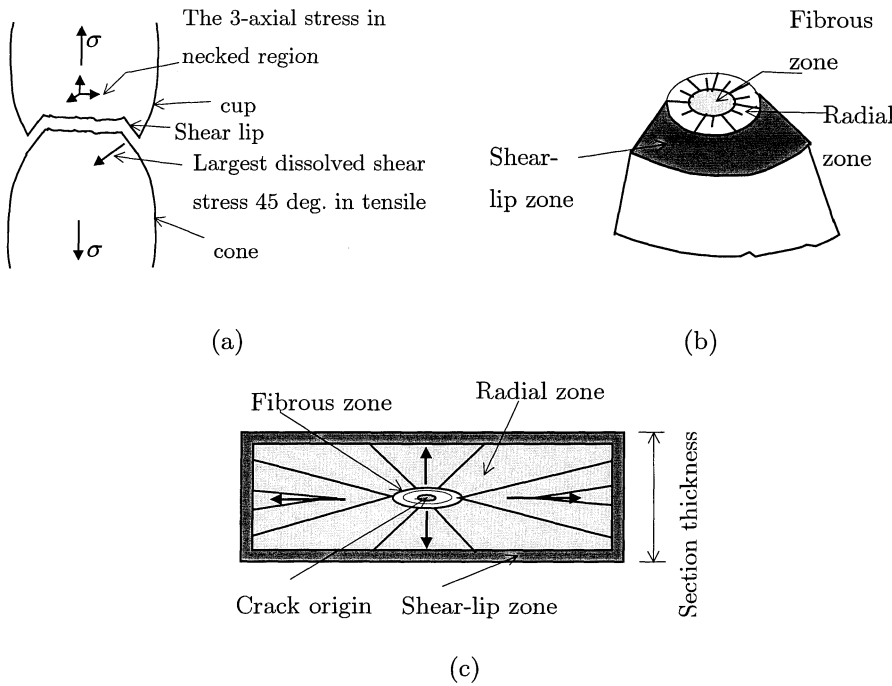


Figure 7.3 (a) Shear lips in cup-cone fracture, (b) Shear lip zone of an unnotched cylindrical specimen and (c) Diagrammatic representation of fracture surface marks in rectangular tension specimen subjected to monotonic loading.

When a cylindrical or rectangular specimen of a ductile material is subjected to monotonic tension loading to failure, the resulting feature is cup-cone fracture, Figure 7.3. On a macroscopic level, with the naked eye, three fracture zones can be identified.

The fibrous zone is located in the central part of the surface, where fracture is initiated. In this zone the state of stress is tri-axial, and failure occurs in a stable mode, by void formation and coalescence on a plane normal to the tensile axis.

The resulting fracture surface has a fibrous appearance. In a cylindrical specimens the fibrous zone will be concentric with the tensile axis.

In the radial zone fracture is rapid and unstable. The markings here are parallel to the direction of crack propagation. In a cylindrical specimen the markings will be radial, with a spoke or star-shaped appearance. The fracture plane is normal to the tensile axis.

Close to the surface plane stress will prevail, and failure occurs by ductile shear rupture at planes with maximum shear stress, 45° to the tensile axis. The fracture surface in this region tends to be extremely smooth.

The size and shape of a test specimen have a strong influence on fracture surface marks.

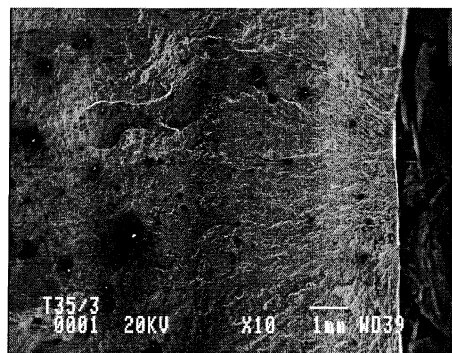


Figure 7.4 Crack growth showing radial marks known as chevron – the origin of the crack is at the right edge of the specimen.

The major difference in fracture appearance due to specimen shape is in the radial zone. As the section of the specimen becomes thinner, the radial zone will be suppressed in favour of a larger shear-slip zone. A very thin section exhibits no radial zone because plane stress conditions apply through the entire cross section.

7.3.2 Chevron markings

Fatigue failures either in brittle or ductile materials show markings characteristic of static overload. Chevron or river markings are often present (Colangelo et al., 1987).

Chevron pattern is characteristic of the radial zone and is a result of relatively rapid crack growth. The appearance indicates the general direction of crack propagation and the inherent tendency of a propagating crack to take the direction giving the shortest path to a free surface, Figure 7.4.

7.3.3 Beach marks

Beach marks are often found on fatigue fractures occurring in service and from fatigue testing of components. Primarily, they are formed either due to variation in load, differences in oxidation or corrosion of the fracture surface or because of local plastic flow in the region with high stress concentration near the crack tip.

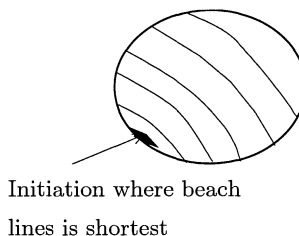


Figure 7.5 Beach marks

Beach marks may form rings or contours, which are concentric with the area of initiation.

7.3.4 Fatigue striations

Fingerprints of fatigue failures are patches of finely spaced parallel marks called fatigue striations. Striations are microscopic in size, and are visible by microscopy only. Not all fatigue fractures show striations.

Striations are indications of the local progress of a crack. Generally, striations are oriented normal to the direction of crack growth, but sometimes seen in other directions too. One reason for this is the influence of inclusions, grain boundaries and other features of the microstructure.

Figure 7.6 shows a typical ductile striation taken from a fatigued titanium specimen. These features are more visible at higher stress levels and are more readily visible in ductile materials.

The local plastic zone at the crack tip causes striations. When a crack advances, the plastic zone remains as a ripple, a striation on the surface. Striations may be formed cycle-by-cycle, or by a process zone mechanism where the crack advances after a number of applied cycles.

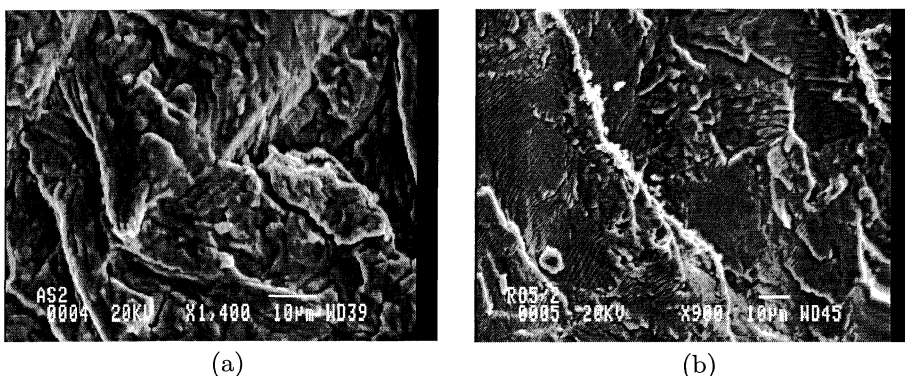


Figure 7.6 Ductile striation in fatigued Titanium 6-4 alloy specimens as seen on SEM images.

The local crack growth direction as indicated by the striations may differ from the over-all direction of crack propagation, Figure 7.6(a).

In particular, a wavy striation with a rough front is typical at high rates of crack growth (Solberg, 1998).

A large plastic zone exists in front of the crack, which may cause extensive secondary cracking. This in turns creates a network of secondary striations, hence the many changes in direction of the local fracture path.

7.3.5 Dimples

Dimples are characteristic features of a ductile failure under monotonic loading i.e. the final fracture zone of a fatigue failure.

Dimples are formed by plastic deformation as part of the fracturing process. In Figure 7.7, equiaxed dimples as a result of tensile overload in the final fracture region of a fatigue specimen is shown.

The fraction of ductile dimple growth in the unstable fracture region increases with increasing stress intensity factor.

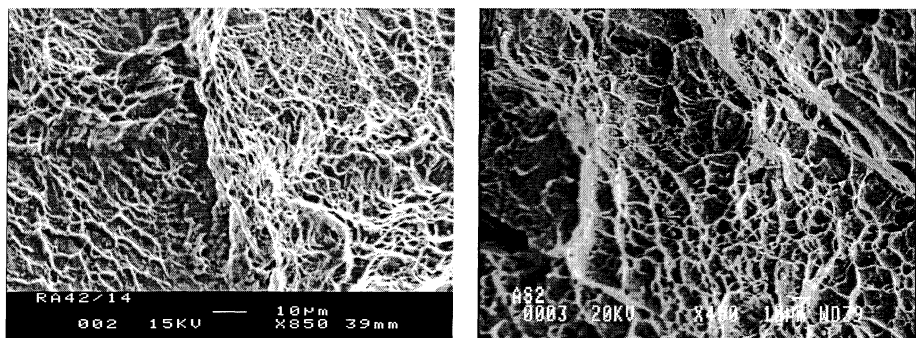


Figure 7.7 Ductile dimples typified final fracture region in fatigued Titanium 6-4 alloy specimens as seen on SEM. The dimples are a result of plastic deformation during the fracture process.

7.4 Fatigue Crack Initiation and Growth

Before discussing the issue of crack initiation and growth, some key points related to the fatigue process will be identified.

Most relevant to the fatigue process in a metallic material is cyclic plasticity. Plasticity is generation and movement of dislocations, i.e. a fault in the crystallographic/atomic arrangement.

With increasing plastic strain, the density of dislocations increases. The presence of dislocations in the material causes permanent offsets /displacements in the material. By accumulation of these displacements, fatigue damage is also introduced into the material.

From the description of the fractographic features, three main stages can be identified in the fatigue process, namely; crack initiation, crack growth and final fracture.

7.4.1 Crack initiation

Primarily, initiation of cracks can be classified into two, viz. initiation from defects (two and three - dimensional) and initiation from the material surface.

Initiation from defects

Two and three-dimensional defects are potential crack initiation sites. The defect could be either located on the surface or embedded. Two-dimensional defects are planar defects such as lack of fusion defects, undercut, lack of penetration etc. An embedded pore is an example of a three-dimensional defect.

Surface defects may be modelled as semi-elliptic defects and embedded defects as elliptic defects (Nisitani et al., 1973), Figure 8.1.

These defects (two and three-dimensional) have high stress concentrations, hence large driving force to cause fatigue crack initiation and growth.

Initiation from surface

In a polycrystalline materials (like engineering materials), grains are individually oriented in a random manner with an ordered atomic structure giving rise to directional properties.

Plastic deformation takes place on crystallographic slip planes within each grain along which dislocations can move more easily than other planes. Slip is controlled by shear stress, hence slip deformation takes place along crystallographic planes that are oriented close to 45° to the tensile stress direction.

Cyclic deformation causes atomic planes sliding relative to each other giving rise to roughening of the surface in slip bands. Further cycling causes intensified slip band deformation which extends into the interior of the grain, resulting into persistent slip bands (PSB), Figure 7.8.

Stage I crack growth

Accumulation of local plastic flow gives rise to surface ridges and troughs called extrusions and intrusions respectively. Oxidation of fresh surfaces and hardening of the strained material tends to weaken the cohesion between the layers in slip bands.

Small cracks may develop in the intrusions. The microcracks grow along slip planes under a shear stress driven process. This is the Stage I growth (i.e. growth in a shear mode). This mode of crack growth may extend over a few grains. Continuous cycling yield one or a few dominating cracks through coalescence of microcracks in different grains.

Stage II crack growth

The stress field associated with the dominating crack causes further growth under the primary action of maximum principal stress; this is called stage II growth. The crack path is now essentially perpendicular to the tensile stress axis corresponding to a Mode I crack in fracture mechanics analysis, Figure 7.8(b). Stage II crack growth usually leads to the formation of fatigue striations.

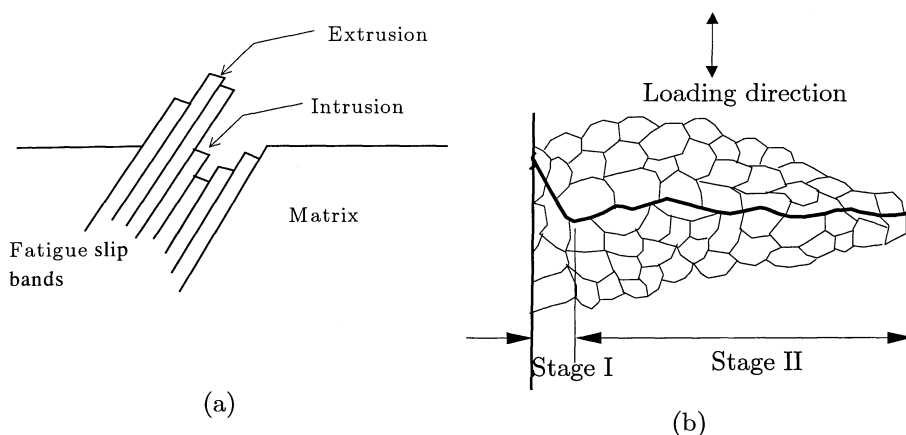


Figure 7.8 (a) Slip band with extrusions and intrusion formed on the surface of a grain subjected to cyclic stress. Crack nucleation at intrusion. (b) Stage I and Stage II crack growth in polycrystalline material.

7.4.2 Crack growth

Crack growth mechanism in Stage II could be due to one of the following: ductile striation, microcleavage, microvoid coalescence and the intergranular separation (Zheng, 1994).

For an alloy with a ductile phase as the continuous matrix, the crack growth mechanism is by striation formation (cycle by cycle striations or process zone striations). Interestingly, when the crack growth is by ductile striation mechanism the crack growth rates are lowest (Zheng, 1987).

Cycle by cycle striations

In ductile materials, fracture surfaces created by stage II crack growth are characterised by striations whose density and width can be related to the applied stress level. For low alloyed steel and polycrystalline iron, the assumption of one load cycle per striation is only valid in a narrow crack growth rate interval. This interval is less than one order of magnitude, and the striation spacing is dependent on the stress intensity range (Roven et. al., 1991). This striation is an indication of the local progress of a crack.

Process zone striations

The long crack fatigue life is dominated by a non-continuum growth process where the striation spacing is independent of the ΔK , which implies that the number of cycles necessary to form one striation could be greater than one (Roven et al., 1991).

Rapid crack growth region

For ductile materials, the characteristic features of the rapid crack growth region are ductile dimples formation. These are regions of higher stress intensity range and crack growth rate $\geq 10^{-6} \text{ m/cycle}$. In high cycle fatigue, which is relevant for riser design, this is the last and relatively short phase of fatigue life, and of no significance to fatigue assessment.

Development of the fatigue process for initiation from defects and initiation from surface (PSB)

Summarily, the fatigue process in time scale for two types of initiation mechanism is given in Table 7.1.

Table 7.1 Development of the fatigue process for initiation from defects and initiation from surface (PSB)

Initiation from defects	Initiation from surface (PSB)
Cyclic loading	Cyclic loading
-	Formation of PSB, stage I crack growth
Physically small crack already exists ($\approx 0.2 - 0.6\text{mm}$)	Formation of a stage II physically small crack ($\approx 1\mu\text{m}$)
Small crack growth (to several mm)	Small crack growth (1 - 2mm) + small crack interactions and linking together (several mm)
Long crack growth	Long crack growth
Fracture	Fracture

8 FRACTOGRAPHIC INVESTIGATION – MAIN CONCEPTS

8.1 Classification of Defects

Based on the investigated fracture surfaces of the test samples, two types of defect location were identified, viz. surface defect and internal defect. One single case of a corner crack was observed, Figure 8.8.

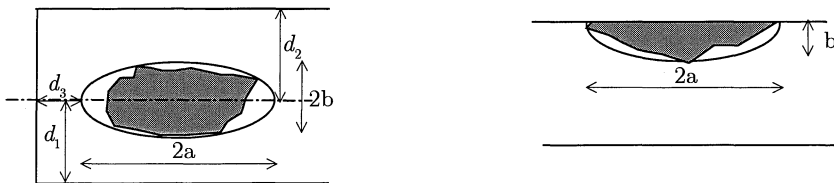


Figure 8.1 Idealised representation of as-detected defects

Principles of flaw re-categorisation

Defects may appear in irregular shapes. Re-categorization of such defects involves re-categorization into idealized crack shapes included in the basic (fracture mechanics) assessment methodology.

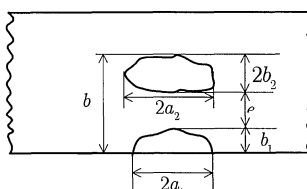
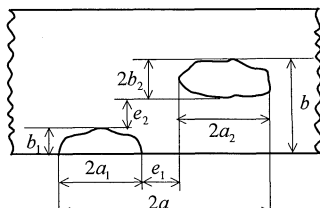
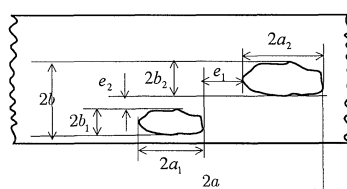
The basic shapes include; circular or elliptical, semi-circular or semi-elliptical defects of various aspect ratios as models for surface or embedded defects.

Interaction between adjacent defects

Fractographic examination of surfaces of fatigue tested TIG welded titanium has shown that it is not uncommon to see clusters of pores located arbitrarily on these surfaces.

If the distances between the cracks are small there is the tendency for interaction between these cracks, which may result to stress shielding and stress amplification etc. (Xiao et al., 1995).

Table 8.1 Interaction of flaws, from BSI PD 6493 (1991).

Flaw types	Criterion for interaction	Effective dimensions after interaction
 Coplanar surface and embedded flaws	$e \leq b_1 + b_2$	$b = 2b_2 + b_1 + e$ $2a = 2a_2$ Comment: Model used for micrograph in Figure 8.3
 Coplanar surface and embedded flaws	$e_1 \leq 2a_1$ $a_1 < a_2$ and $e_2 \leq b_1 + b_2$	$b = b_1 + 2b_2 + e_2$ $2a = 2a_1 + 2a_2 + e_1$ Comment: Model used for micrograph in Figure 8.17
	$e_1 \leq 2a_1$ $a_1 < a_2$ and $e_2 \leq b_1 + b_2$	$2b = 2b_1 + 2b_2 + e_2$ $2a = 2a_1 + 2a_2 + e_1$ Comment: Model used for micrograph in Figure 8.31.

Of importance in the consideration of interaction between adjacent defects are cracks centre distances in both directions (i.e. depth and length directions).

Variation of stress intensity magnification factor at the deepest point due to the presence of another elliptical crack was investigated by Nisitani (Nisitani and Murakami 1974) covering only coplanar elliptical cracks. BSI PD 6493 (1991) gives criteria for interaction between planar flaws.

The guideline was readily available for estimating the effective dimensions after interaction for various forms of embedded flaws: coplanar embedded flaws, coplanar surface and embedded flaws oriented arbitrarily relative to each other.

The cracks in Figure 8.3, Figure 8.5, Figure 8.17 and Figure 8.31 were re-categorised subject to the procedures and criteria given in BSI PD6493: 1991 (Table 8.1).

8.2 Surface Defects

Surface breaking pores are sub millimetres pores at a distance of some few micrometers from a free surface. Generally, the idealised shape for this defect is semi-elliptical.

Examples of surface breaking pores are shown in Figure 8.2 to Figure 8.9.

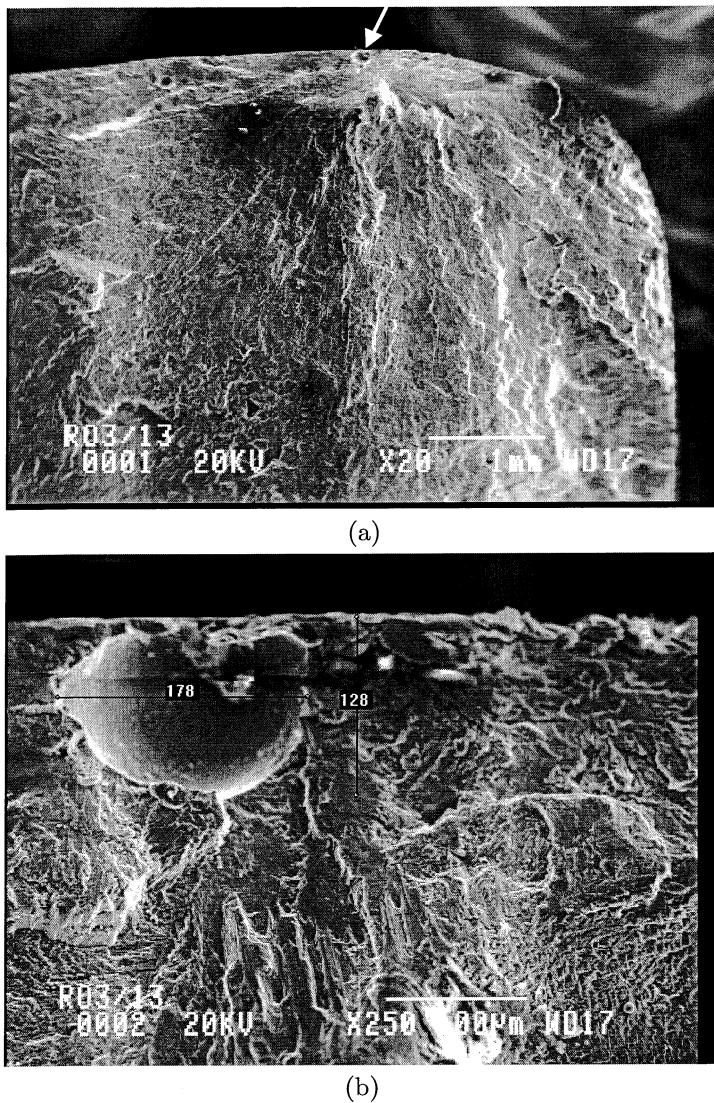


Figure 8.2 Surface breaking pores (a) X20, (b) X250, Specimen R03/13

In Figure 8.2(a), as seen under SEM, Chevron marks point to the origin of fatigue crack as indicated by the arrow. The image in (a) was further magnified in (b), the aspect ratio for this pore is 0.7 and crack depth of $128\mu m$.

In Figure 8.3 is a surface breaking spherical pore on top of an internal elliptical pore with sizes of few microns. By re-categorisation of crack, a conservative shape would be a semi-elliptical crack with crack depth of $224\mu\text{m}$ and crack width of $170\mu\text{m}$.

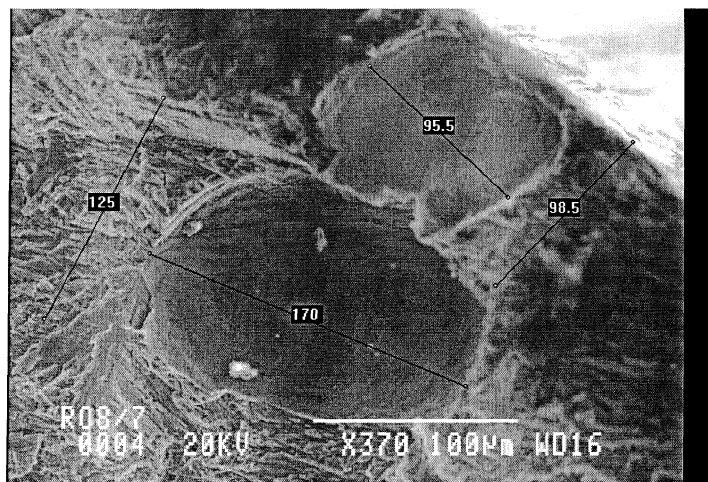


Figure 8.3 Surface breaking pores (re-categorised), Specimen R08/7

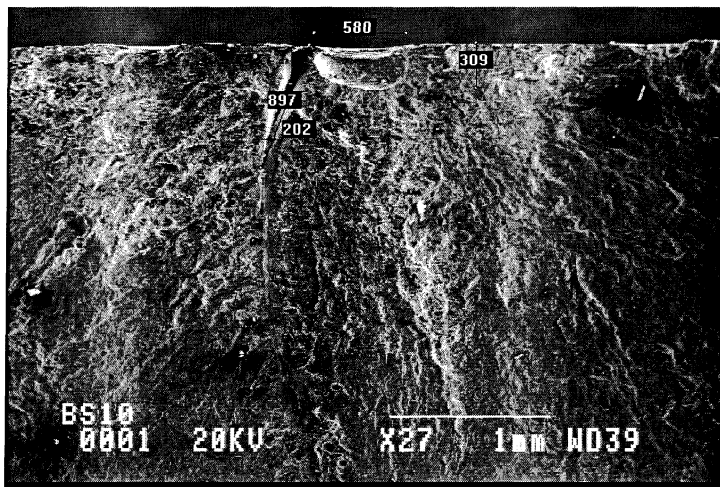


Figure 8.4 Surface breaking pores (semi-elliptic pore), Specimen BS10

In Figure 8.4, the fracture marks are directed to the origin of the fatigue. Apparently, it is a semi-elliptical crack with a depth of $309\mu\text{m}$ and aspect ratio of 0.53.

In Figure 8.5 fatigue was initiated from two adjacent surface defects. In this case the defects were re-categorised and the resulting semi-elliptic crack size had a depth of $244\mu m$ and length of $588\mu m$.

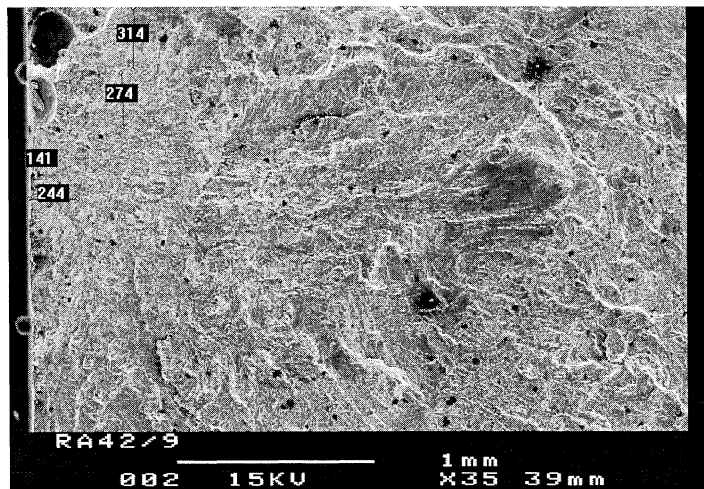


Figure 8.5 Surface breaking pores (re-categorised), Specimen RA42/9

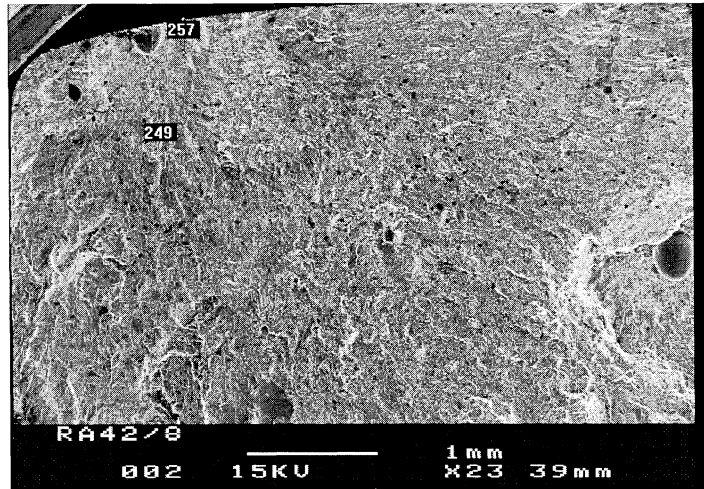


Figure 8.6 Surface breaking pores, Specimen RA42/8

Crack initiation in specimen RA42/8 in Figure 8.6 was from the pore located on the top left of the fractographic image.

A good approximation for the modelling could be a semi-elliptical crack with depth of $257\mu m$ and aspect ratio close to unity.

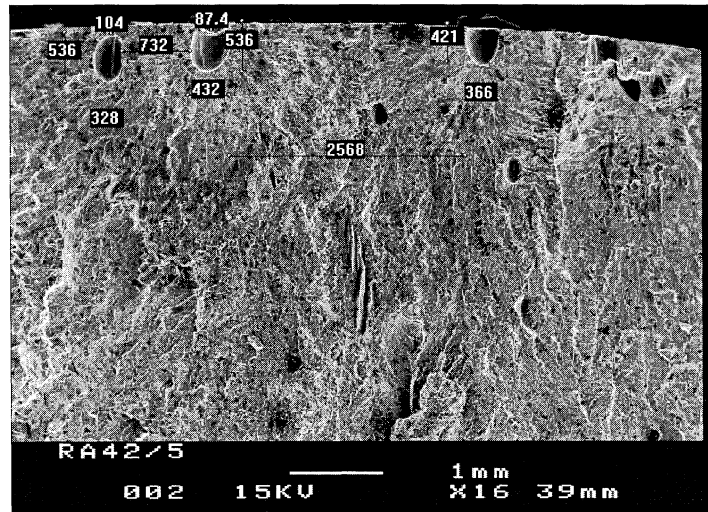


Figure 8.7 Multi-origin crack initiation from the clusters of pores, Specimen RA42/5.

The image in Figure 8.7 shows a multi origin crack initiation from the clusters of pores that break on to the free surface. These pores can be termed as coplanar surface flaws. According to PD 6493:1991, the criterion for interaction of the pores were not met because the distance between the pores is greater than stipulated by PD6493.

It is reasonable to choose the middle pore with crack depth of $536\mu m$ and crack width of $432\mu m$ for further analysis since it is the largest pore. There is no beach marks because there was no variation of load during fatigue test.

A corner crack was the fatigue initiation point in Figure 8.8 from the pattern of the fracture marks, which are essentially Chevron. In this region, a surface and an embedded flaw exist. However, this will be regarded as a surface defect because the distance between the pores is too large to comply with the criterion for re-categorisation.

The crack depth is $208\mu\text{m}$ with an aspect ratio of 0.42.

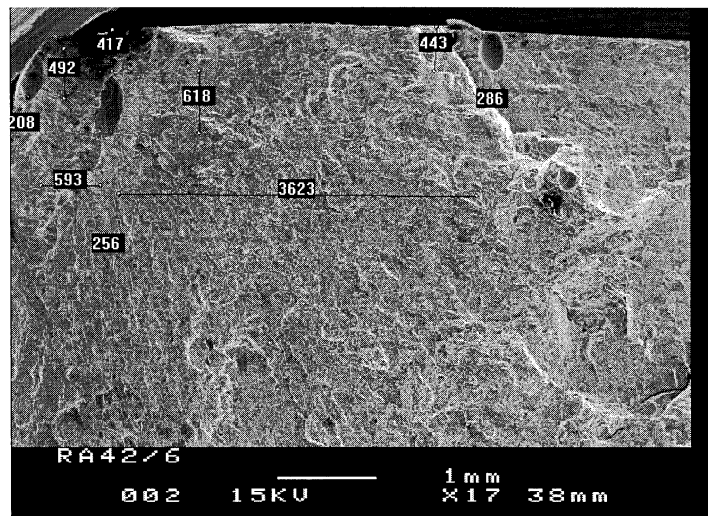


Figure 8.8 Fatigue crack originating from a corner crack, Specimen RA42/6

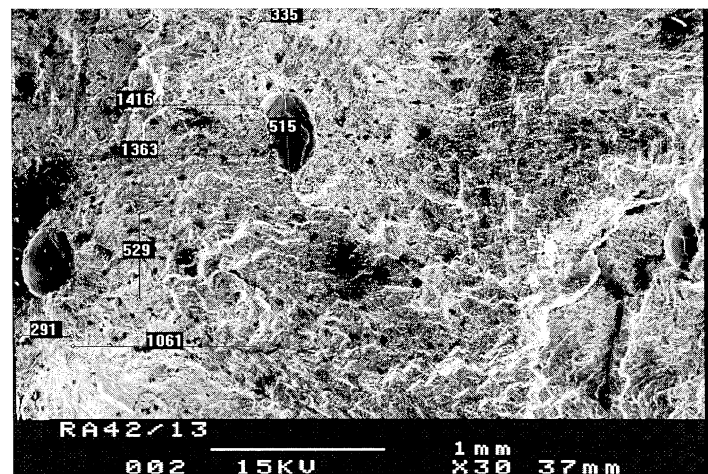


Figure 8.9 Fatigue crack initiation from the elliptical pore to the left, Specimen RA42/13

The image of the fatigue surface represented in Figure 8.9 shows that the fatigue crack initiation was due to the elliptical pore to the left with an aspect ratio 0.55 and crack depth of $291\mu\text{m}$.

The distance to the free surface is negligible; as such, it can be classify as surface breaking pore.

Figure 8.10 – Figure 8.15 shows the type of surface initiation (PSBs) described in section 7.4, it is a multi-origin fatigue failure due to extensive slip band deformation (Figure 7.4).

RA41/14 (Figure 8.10) has only the root of the weld ground. The crack had initiated from the toe of the weld.

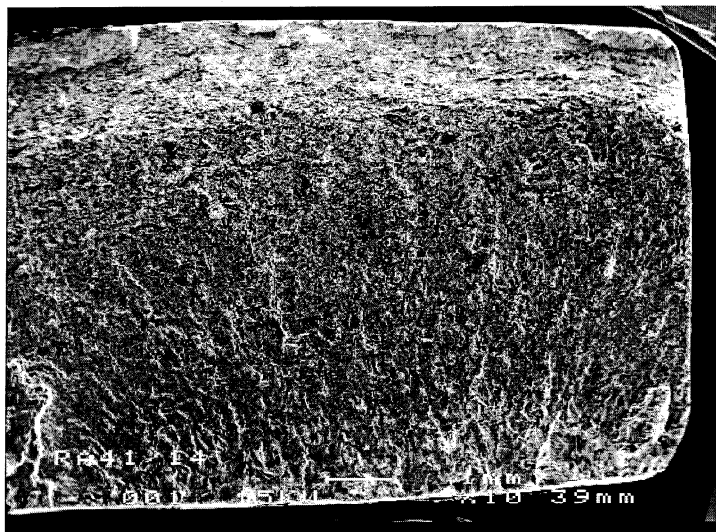


Figure 8.10 Fatigue crack initiation due to formation of PSBs, Specimen RA41/14

Note the transition to shear rupture along the top edge of Figure 8.10. Here the final fracture zone extends from the fatigue zone into a shear fracture (plane-stress mode) at 45 degree to the surface of the part bordering the tensile fracture. This behaviour is common in ductile materials, with thick or round sections (Solberg, 1998).

RA41/12 (Figure 8.11) was of the same type with RA41/14 (Figure 8.10). In this case the fatigue crack initiation was from the root.

A simple explanation is that fatigue is a surface sensitive process. In the absence of internal inhomogeneities with higher stress concentration, stress gradients giving maximum stress on the surface can be expected. Moreover, the surface is never ideally smooth, defects in the form of surface scratches from machining or handling can be found.

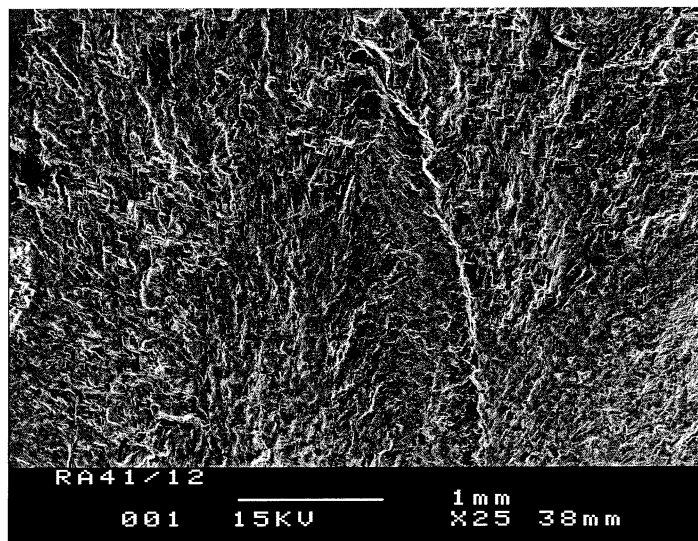


Figure 8.11 Fatigue crack initiation from the surface, Specimen RA41/12

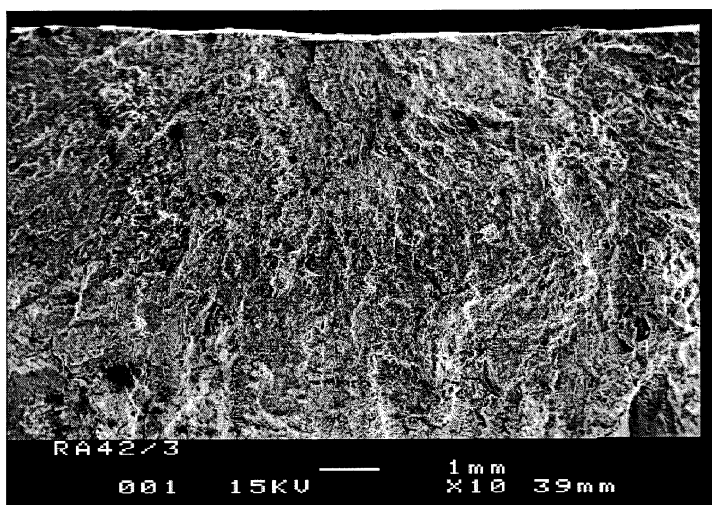


Figure 8.12 Fatigue crack initiation from the surface. X10, Specimen RA42/3.

In Figure 8.12 to Figure 8.15, the specimens were in the as-welded condition. Surface initiation is observed.

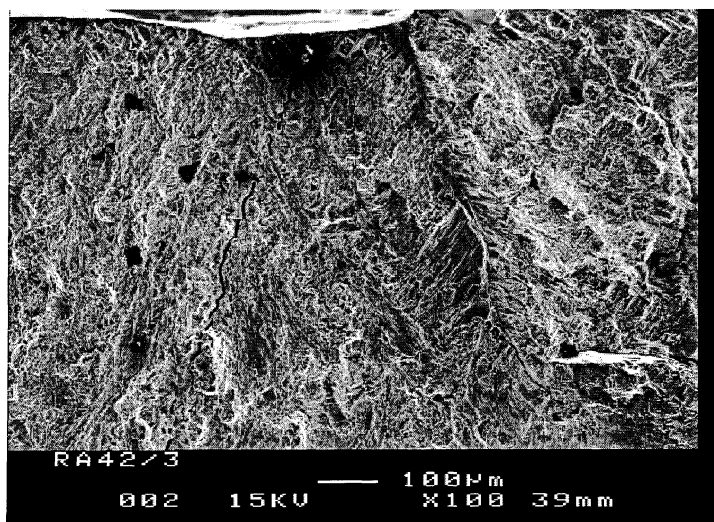


Figure 8.13 Fatigue crack initiation from the surface. X100, Specimen RA42/3.

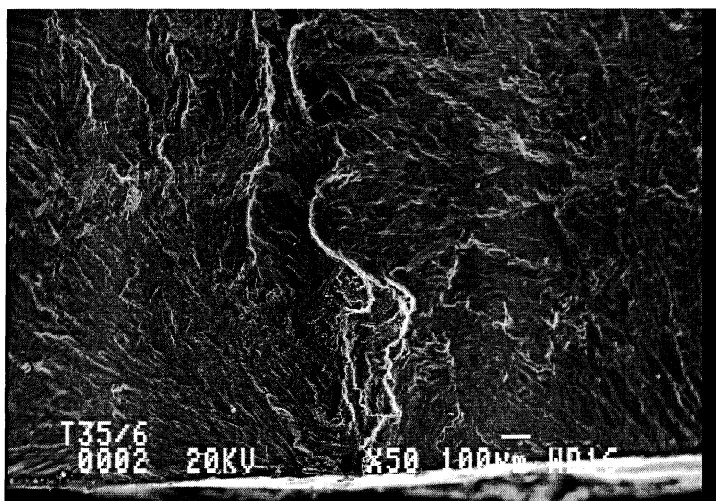


Figure 8.14 Fatigue crack initiation from the surface, Specimen T35/6.

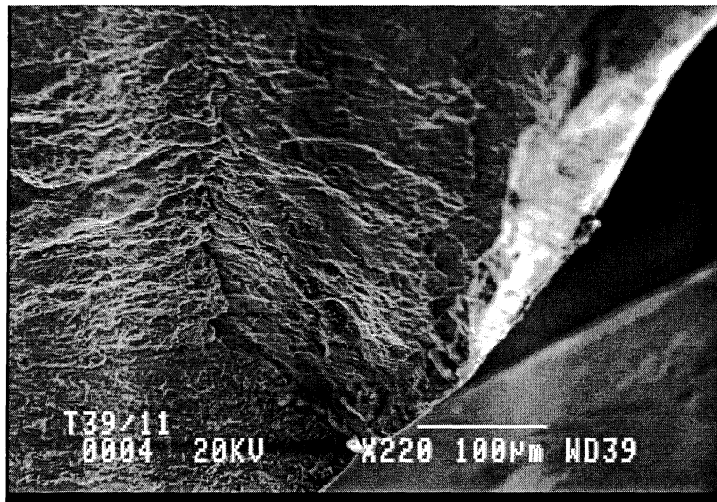


Figure 8.15 Fatigue crack initiation from the surface, Specimen T39/11.

8.3 Internal Defects

Generally, on the basis of applied stress only, fatigue cracks are often initiated from the surface. Comparison of stress concentration and stress intensity factors for inhomogeneities of the same type on the surface and in the interior indicates a higher stress concentration for surface cracks (Klesnil et al., 1992).

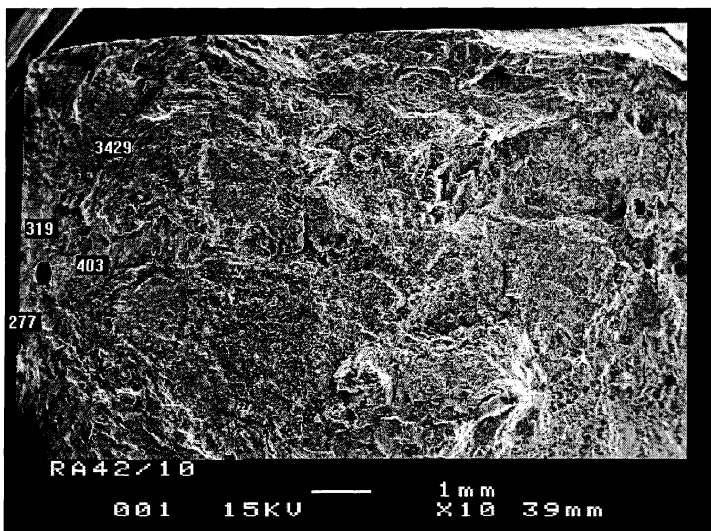


Figure 8.16 Fatigue crack initiation due to embedded flaw, Specimen RA42/10

This section focuses on the internal fatigue initiation. In most cases, porosity was the causes of initiation.

The fractographs have shown defects with different orientation, size and distance to the free surface. The common shape of the defects was found to be elliptical.

All the specimens were fully ground prior to fatigue loading except specimen RA41/13 (Figure 8.17) which had only the root ground and the specimens in Figure 8.26 and Figure 8.27 (AS6 and BS2 respectively) which were in as-welded condition.

In Figure 8.16 the failure origin is from the elliptical pore located at a distance of $277\mu\text{m}$ and with the major axis parallel to the free surface. The aspect ratio for this defect is 0.79 and a crack depth of $319\mu\text{m}$.

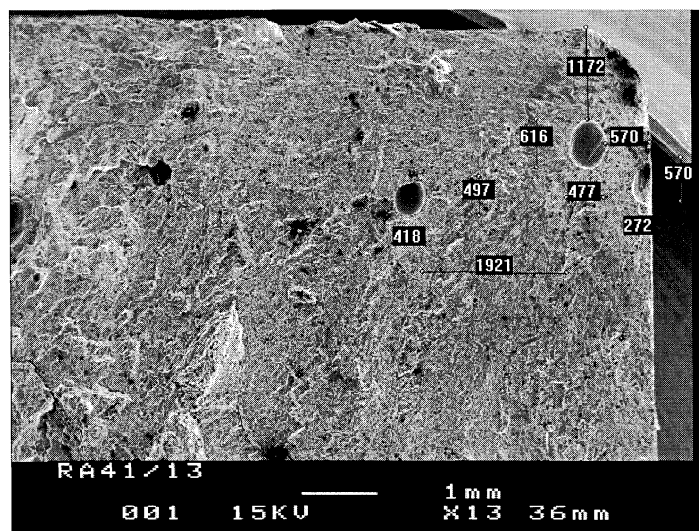


Figure 8.17 Fatigue crack initiation due to surface and an embedded flaw, Specimen RA41/13

The fracture marks for specimen RA41/13 (Figure 8.17) indicates a fatigue crack initiation from both the larger pore on the top right and the smaller pore that breaks on to the free surface.

This is an example of a surface and an embedded flaw adjacent to each other.

The smaller pore is idealised as a semi-elliptical crack with crack depth of 0.272mm and crack length of 0.57mm . Using BSI PD6493 (1991), the cracks will interact to form a much larger crack with aspect ratio of 0.88 and crack depth of about 1mm .

The fatigue initiation sites for specimens RA41/6, RA41/10 (Figure 8.18 and Figure 8.19), and specimens RA41/7, RA41/8 (Figure 8.20 and Figure 8.21) are internal pores. The location of the defect to the free surface is greater than 1.0mm .

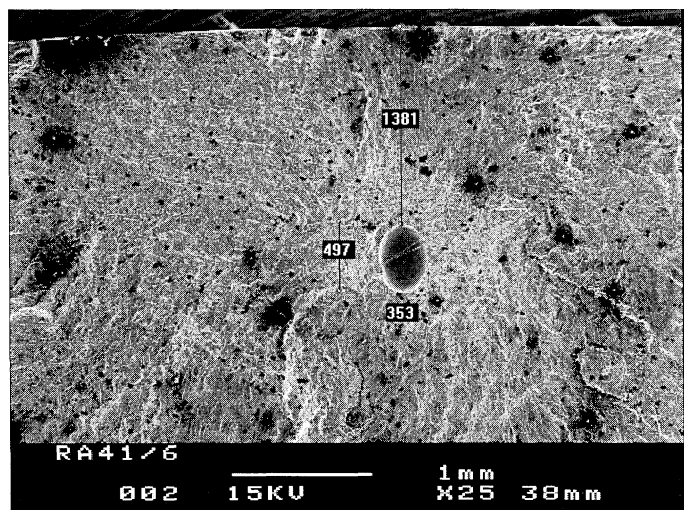


Figure 8.18 Internal initiation from the elliptical crack, Specimen RA41/6

The respective aspect ratios for the defects with the corresponding distance to the free surface are $(1.4, 1.381\text{mm})$, $(1.3, 1.792\text{mm})$, $(1.45, 1.337\text{mm})$ and $(0.66, 2.25\text{mm})$.

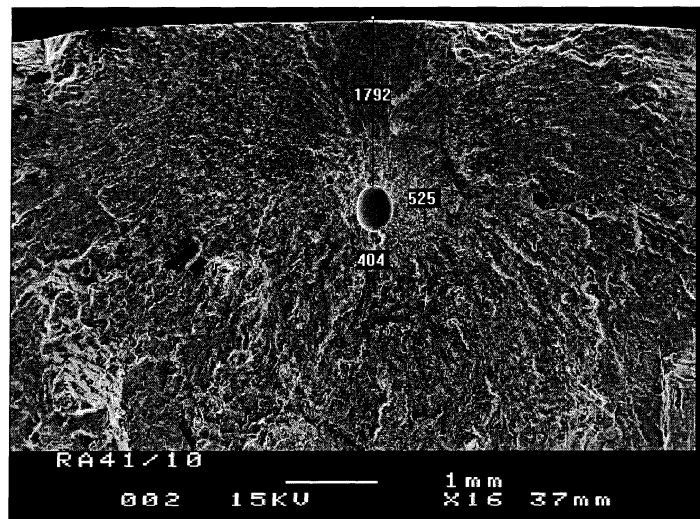


Figure 8.19 Internal initiation from the elliptical crack, Specimen Ra41/10

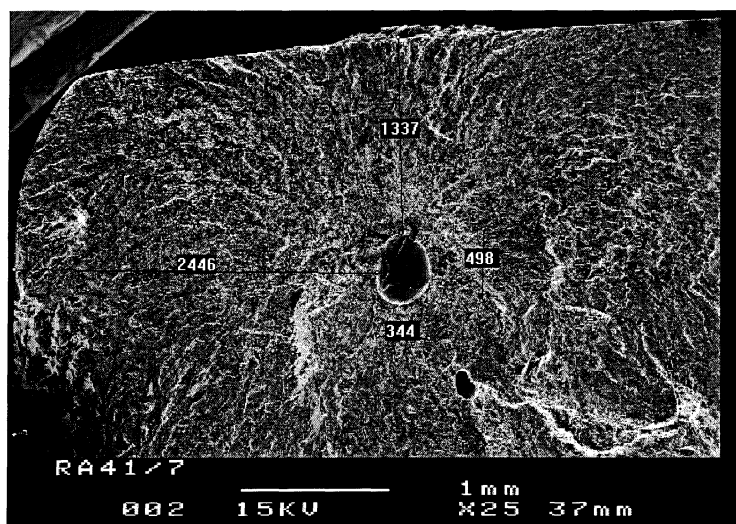


Figure 8.20 Internal initiation from the elliptical crack, Specimen RA41/7

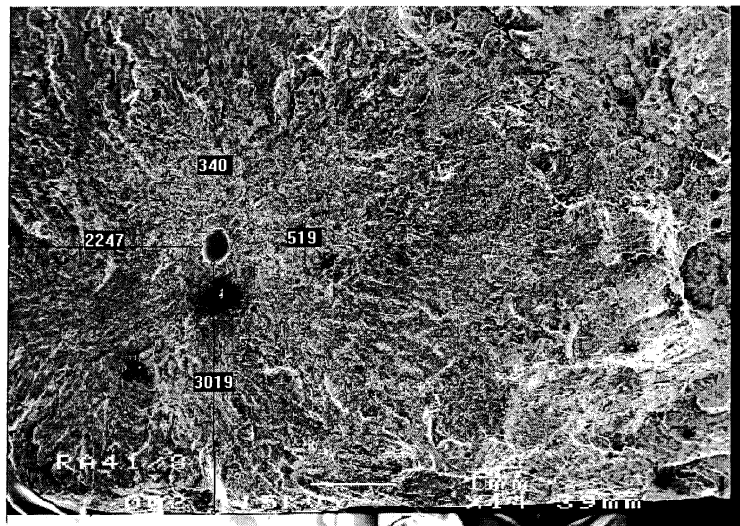


Figure 8.21 Internal initiation from the elliptical crack, Specimen RA41/8

In Specimen RA42/12 the fatigue crack started from the pore on the top left corner, Figure 8.22. The aspect ratio and the distance to the free surface in the thickness direction is $(1.9, 0.8mm)$ and in the width direction is $(0.53, 0.41mm)$.

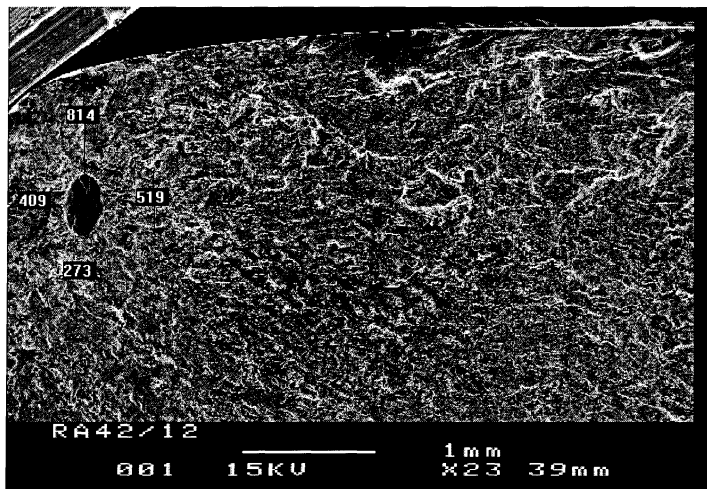


Figure 8.22 Fatigue crack initiation due to embedded flaw, Specimen RA42/12

Two pores were observed on the micrograph of specimen RA41/9 in Figure 8.23. Interaction of pores is ruled out considering their separation. Furthermore, the pore to the left is closer to the final fracture region. It is concluded that the fatigue initiation was from the pore (nearly spherical) on the right side. Further evidence is seen from the fracture mark. The aspect ratio as well as the distance to the free surface is (1.15, 1.96mm and a crack depth of 0.464mm.

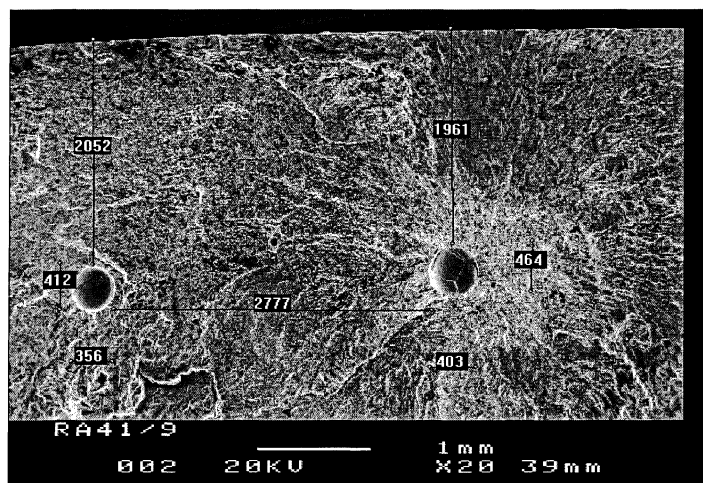


Figure 8.23 Fatigue crack initiation due to embedded flaw, Specimen RA41/9

The aspect ratio and location of the elliptical pore to the free surface for specimen RA42/14 in Figure 8.24 is (1.53, 2.53mm). The radial marks points to the failure initiation point. The line with the arrow pointing to the right hand side marks the boundary between the fatigue region and the final fracture domain.

Typical features characterising the left-hand region are ductile striations from fatigue crack growth. Dimples were found in the region in the direction of the arrow, indicating a ductile mode of failure.

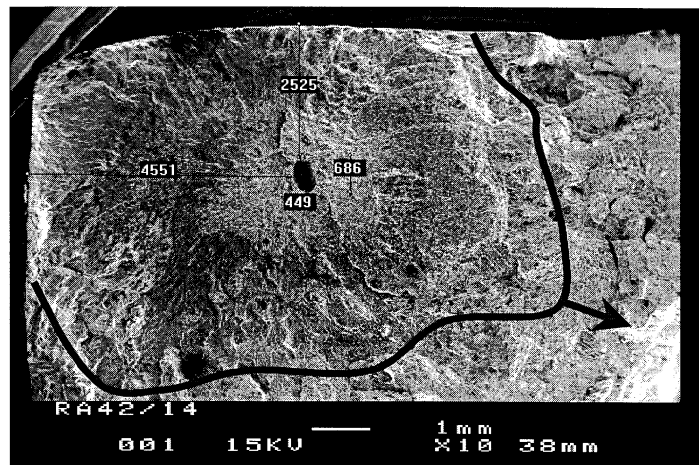


Figure 8.24 Fatigue crack initiation due to embedded flaw. The arrow points to dimples zone indicating a ductile mode of failure, Specimen RA42/14

Initiation of fatigue crack in Figure 8.25 is from the topmost elliptical crack, despite the closeness of the lower crack to the free surface.

From the pattern of the fracture marks, the influence of the lower crack appears to be insignificant.

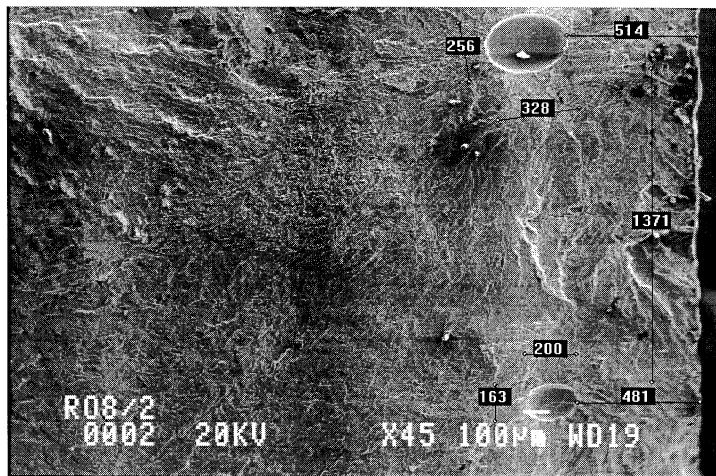


Figure 8.25 Embedded elliptic crack as a fatigue origin, Specimen R08/2

The images in Figure 8.26 and Figure 8.27 represent lack of fusion defects. The fracture marks are seen radiating from the defects, proving fatigue initiation at the defects.

The idealised form for the defect in Figure 8.26 is an elliptic crack located at a distance of $1.6mm$ to the free surface with crack depth of $0.603mm$ and crack length of $3.835mm$.

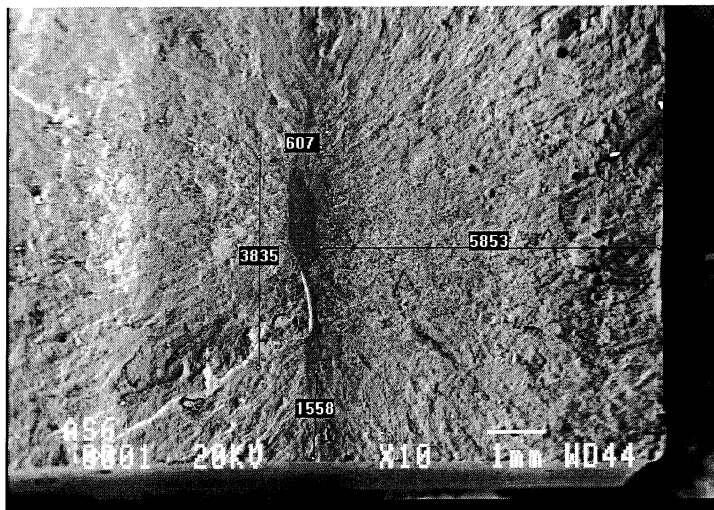


Figure 8.26 Fatigue crack initiation due to lack of fusion defect, Specimen AS6

The crack depth and crack length for BS2 in Figure 8.27 is $5.8mm$ and $0.54mm$ respectively. The distance to the free surface in the width and through-thickness direction are 0.54 and $2.6mm$. These defects can be treated as a two-dimensional crack in a three-dimensional body because the aspect ratio is very small.

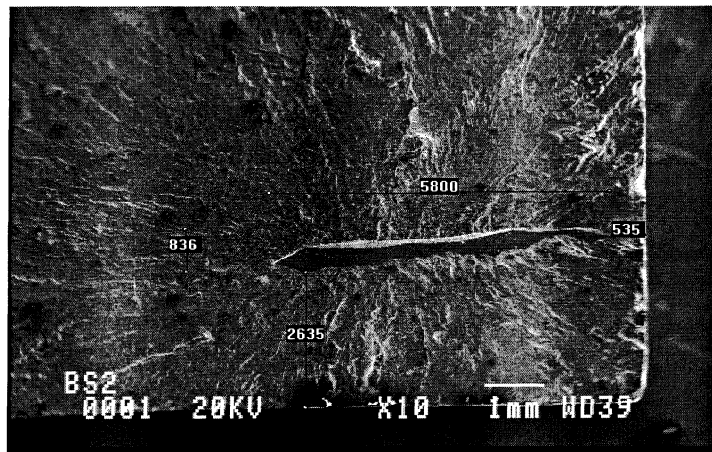


Figure 8.27 Fatigue crack initiation due to lack of fusion defect, Specimen BS2

8.3.1 Clusters of pores

Figure 8.28 and Figure 8.29 is taken from the same specimen, and are overlapping. Clusters of pores are seen in Figure 8.28 but the origin of the fatigue cracks is from the pore to the far left with the crack depth of $466\mu m$ with a crack length of $585\mu m$. Effect of interaction of pores was neglected.

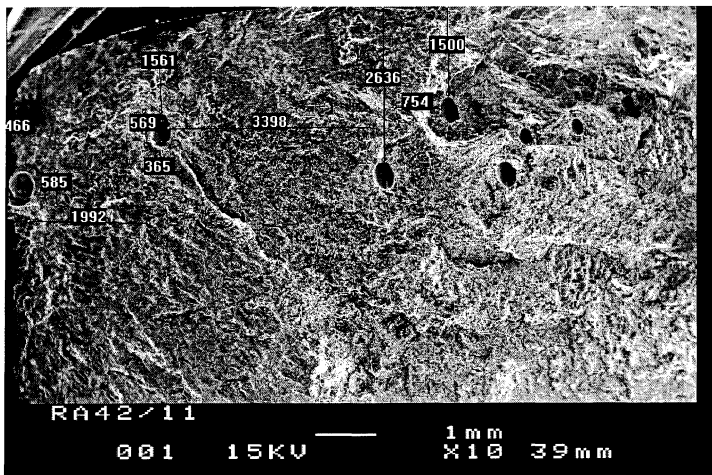


Figure 8.28 Clusters of pores. X10 the origin of the fatigue crack is to the far left, Specimen RA42/11.

The boundary between the fatigue region and the final fracture region is shown by the change in coloration in specimen RA42/11 (Figure 8.29) due to out of focus. This region is represented to the right of the demarcation. The region is very rich in dimples. To the left hand side of the boundary is ductile striations zone from fatigue crack growth.

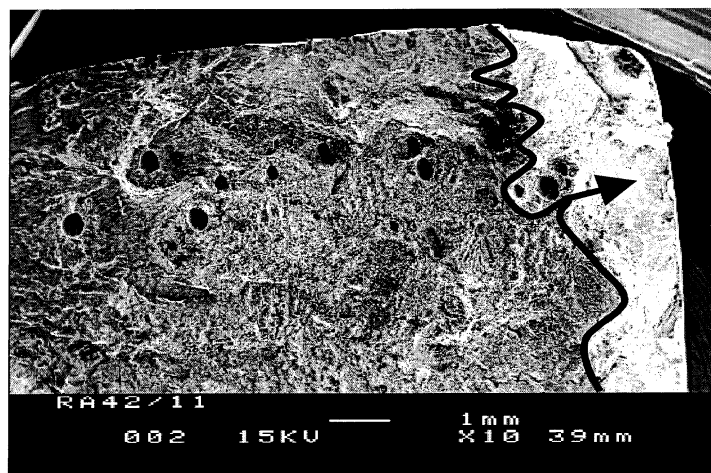


Figure 8.29 Clusters of pores. X10 but overlapped with (Figure 8.28), Specimen RA42/11

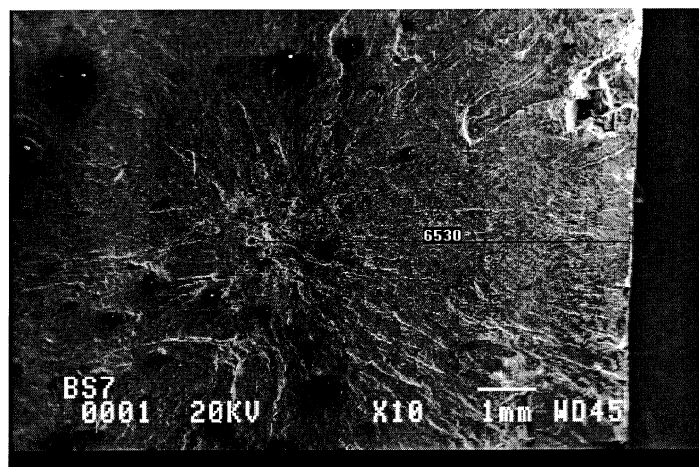


Figure 8.30 Clusters of pores as fatigue initiation origin. X10, Specimen BS7

Figure 8.30 and Figure 8.31 were taken from the same specimen. The fatigue crack was initiated from clusters of pores. In Figure 8.31, is a quantitative examination of the initiation site. Following the guideline (BSI PD6493, 1991) for interaction of such defect, high level of interaction is expected from the largest pore to the left and the two others above it.

The interaction can be indicated in two stages. Firstly, the two pores above will interact to give an elliptical pore of size $0.25 \times 0.29mm$. This new pore will now interact with the large pore below to give a much larger pore of size 0.49×0.57 with a distance of $6.53mm$ from the free surface.

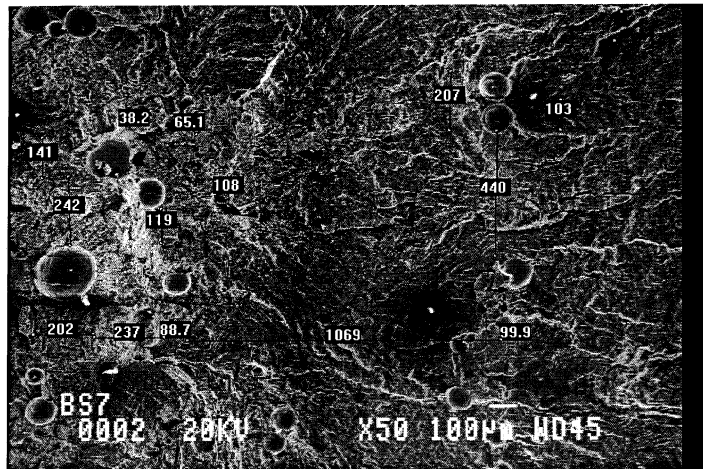


Figure 8.31 Clusters of pores as fatigue initiation origin. The largest pore to the left and the two others above it were assumed to interact, Specimen BS7

8.4 Results

In the tables below, SN data and geometry of initial defects for a range of specimens are shown. These data were used for the fracture mechanics modelling and analysis.

Table 8.2 Fatigue and geometry data for surface defects

Specimen ID	ΔS (MPa)	N	Crack depth, b (μm)	Aspect ratio, b/2a	d_1 (mm)	Comment
R03/13	500	74148	128	0.70	0	SE
R08/7	270	225003	224	1.32	„	RC
BS10	250	683690	309	0.53	„	SE
RA42/9	300	179014	244	0.42	„	RC
RA42/8	300	96884	257	1.03	„	SE
RA42/5	300	89151	536	1.24	„	MO
RA42/13	300	142033	291	0.55	≈ 0	RC
RA42/11	250	171171	466	0.80	0	SB

SE: Semi-elliptic RC: Re-categorised MO: Multi-origin SB: Surface breaking

Table 8.3 Fatigue and geometry data for surface initiation (PSBs)

Specimen ID	ΔS (MPa)	N	Crack depth, b (μm)	Aspect ratio, b/2a	d_1 (mm)	Comment
RA41/14	250	144352	≈ 0	≈ 0	≈ 0	PSB,s
RA41/12	250	149937	„	„	„	PSB,s
RA42/3	150	429313	„	„	„	PSB,s
T35/3	200	117333	„	„	„	PSB,s
T35/6	250	93576	„	„	„	PSB,s
T39/11	220	1.75E6	„	„	„	PSB,s

Table 8.4 Fatigue and geometry data for internal defect

Specimen ID	ΔS (MPa)	N	Crack depth, b (μm)	Aspect ratio, b/a	d_1 (mm)	Comment
RA42/10	250	592009	319	0.79	0.28	Elliptical pore
RA41/13	250	87896	1000	0.88	0	CS/EF
RA41/6	250	531234	497	1.41	1.38	Elliptical pore
RA41/10	300	544789	525	1.30	1.79	„
RA41/7	250	276548	498	1.45	1.34	„
RA41/8	250	1,48E6	340	0.66	2.25	„
RA42/12	250	172229	519	1.90	0.80	„
RA41/9	300	376852	464	1.15	1.96	„
RA42/14	300	617857	686	1.53	2.53	„
AS6	300	66030	603	6.36	1.6	Lack of fusion
BS7	350	118070	490	0.86	6.53	CP
R08/2	300	241426	328	1.28	0.514	Elliptic pore
BS2	250	238593	5.8mm	10.27	0.54	Lack of fusion

CS/EF: Coplanar surface and embedded flaw

CP: Clusters of pores

9 STRESS INTENSITY FACTOR

9.1 Small Fatigue Cracks

Three distinct categories of small fatigue cracks have been identified (Miller, 1991), (Tokaji, 1992) namely; microstructurally small cracks, mechanically small cracks and small cracks regarded as large cracks. Miller (1991) provided each of the phases with its own branch of fracture mechanics.

The present study deals with a crack size range $0.3 - 0.7\text{mm}$. This lies within the maximum crack length considered to be microstructurally small cracks. In essence it could be regarded as the minimum crack size for mechanically small cracks. Thus it is considered large enough to allow the use of LEFM, even if the small scale yielding condition is not met. This deviation only affects the crack closure behavior (Tokaji, 1992).

Given this condition (i.e. confinement of nonlinear material deformation to a small region surrounding the crack tip) for linear elastic fracture mechanics, crack growth can be characterized in terms of the stress intensity factor, ΔK expressed as

$$\Delta K = \Delta S \cdot \sqrt{\pi \cdot b} \cdot F \quad (9.1)$$

F is a form function depending on geometry, crack shape and size.

The stress intensity factor range, ΔK is the difference between the maximum and minimum stress intensity factor, during the load cycle. It is a measure of the cyclic stress field at the crack tip.

Experimental or approximate analytical methods are available procedures that can be utilised to obtain the stress intensity factor solution for internal cracks under tension or bending loads.

Stress intensity factor solutions for idealised geometry and load configuration for two-dimensional cracks e.g. Rooke et al. (1981), Newman et al. (1981), Tada et al. (1985) etc. are suitable for treatment of surface defects. Usually the results are obtained by numerical methods and presented in form of tables or curves.

For convenience, numerical equations or polynomial formulae are preferable. Newman et al. (1983) presented numerical equations for obtaining the stress intensity factor for cracks in three-dimensional finite bodies subjected to tension and bending loads. The case of embedded eccentrically placed crack was not covered in this analysis.

Isida et al. (1984b) provided stress intensity factor solutions for an embedded elliptical crack subjected to tension loading. They introduced the concept of back surface and front surface correction (Figure 9.2) to cater for the effect of finite thickness.

Fett et al. (1990) used the weight function approach to compute the stress intensity factor for any virtual incremental extension of a given crack. They introduced the concept of front surface and back surface correction based on the result of Isida et al., 1984. Guozhong et al. (1996) provided geometric function data in tabular form for an embedded elliptical crack in finite thickness plates under uniform tension.

9.2 Modelling of Internal Defect Near Free Surface Under Tension

Post fracture analysis based on fractographic investigation of fracture surfaces (Chapter 8) revealed that a number of fatigue failures in the titanium welds had originated from internal defects of sub-millimeter size which were found on arbitrary locations in the weld zone.

The defects were close to elliptical or spherical shape, this provided a basis for idealisation as an embedded elliptical crack located with one of its principal axes parallel to the plate surfaces, Figure 9.1 and subjected to uniform tension.

The spherical nature of such defect can be represented as the transition of an elliptical flaw to circular when the ratio of the principal axes tends to unity as the crack grows.

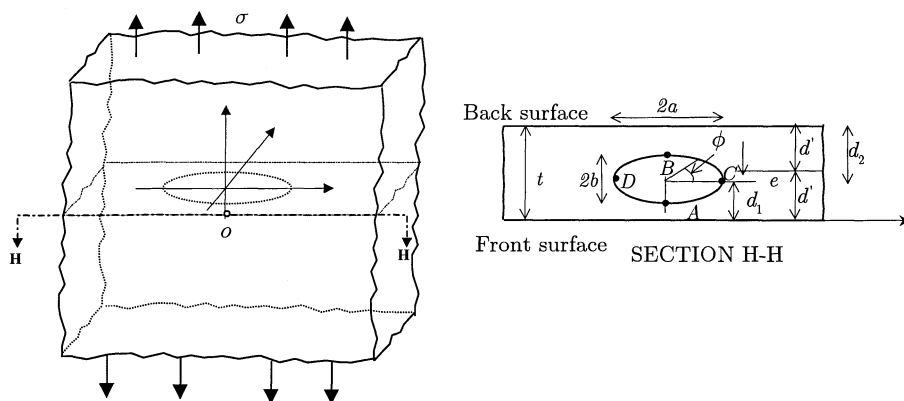


Figure 9.1 An elliptical crack embedded in plate subjected to uniform tension

The crack growth rate is a function of the stress intensity factor of point A, B, C and D in Figure 9.1. These stress intensity factors are indicators of the state of stress at these locations. For ease of identification, points A, B, C and D will be referred to as 6, 12, 3 and 9 o' clock position on the ellipse.

Case 1: $a > b$

At point A the mode I stress intensity factor is maximum. A larger driving force for crack growth is expected compared to points B, C and D for a situation where $a \geq b$.

Case 2: $a < b$

The formation of embedded elliptical pores in welded titanium components is arbitrary, hence it is not unlikely to have an elliptical pore close to the free surface with different orientation compared to case 1.

For $a < b$ and for small values of b/d_1 the maximum mode I stress intensity factor is located at points C and D, Isida et al. (1984b). As the crack grows, b/d_1 increases, and the maximum stress intensity factor will move to point A due to the free surface effect.

9.2.1 Magnification Correction Factor For An Embedded Elliptical Crack

For an embedded elliptical crack subjected to external load in a material, the shape and hence the form function varies throughout the fatigue life owing to the three dimensional nature of the defect.

Berge (1998b) and Mainçon (1999) used a constant form function in their crack growth modelling, equal to the form function of the initial crack. There is need to demonstrate the extent of influence of geometrical change on the form function. Obviously, internal elliptic defects will have a varying form function throughout the fatigue life.

The locations of interest are the symmetry points of the ellipse, Figure 9.1. The form function at the 12 o' clock position is not very significant in our model (embedded elliptical cracks in a semi-infinite plate under uniform tension) since the crack is closer to the front surface and small compared to the cross-sectional area of the plate.

9.2.1.1 Crack tip at short axis of cracks - 6 o' clock position

The stress intensity factors at the point close to the front surface (6 o' clock position) and the back surface (12 o' clock position) was determined by Isida et al. (1984b) for a wide range of embedded elliptical cracks.

Equations (9.2) and (9.3) gave the numerical result of the stress intensity factor at locations (point *A* and *B*).

$$K_{I,A} = \Delta S \cdot \frac{\sqrt{\pi \cdot b}}{\Phi} \cdot M_A \quad (9.2)$$

$$K_{I,B} = \Delta S \cdot \frac{\sqrt{\pi \cdot b}}{\Phi} \cdot M_B \quad (9.3)$$

M_A and M_B are the stress intensity magnification factors showing the free surface effects on the basis of the result of the elliptical crack of the same shape embedded in an infinite solid.

For an eccentrically located crack,

$$M_A = (M_1)_{\lambda=\frac{b}{d_1}} \cdot (M_2)_{\lambda=\frac{b}{d_2}} \quad (9.4)$$

$$M_B = (M_2)_{\lambda=\frac{b}{d_1}} \cdot (M_1)_{\lambda=\frac{b}{d_2}} \quad (9.5)$$

M_1 and M_2 give the respective correction factors for front surface and back surface for the semi-infinite body or of the finite thickness plate Figure 9.1.

The polynomial forms of Isida et al (1984b) are given in equations (9.6) – (9.7)

$$\begin{aligned} M_1 = 10^{-4} & \{9995 + 5 \cdot \mu - \mu^2 - \mu^3 \\ & + \lambda \{2038 - 3856 \cdot \mu + 5519 \cdot \mu^2 - 2746 \cdot \mu^3\} \\ & + \lambda^2 \{-7489 + 6965 \cdot \mu - 9850 \cdot \mu^2 + 5678 \cdot \mu^3\} \\ & + \lambda^3 \{13763 - 10266 \cdot \mu + 4242 \cdot \mu^2 - 1049 \cdot \mu^3\}\} \end{aligned} \quad (9.6)$$

$$\begin{aligned} M_2 = 10^{-4} & \{9999 + 3 \cdot \mu - 4 \cdot \mu^2 + 2 \cdot \mu^3 \\ & + \lambda \{282 - 2709 \cdot \mu + 5235 \cdot \mu^2 - 2845 \cdot \mu^3\} \\ & + \lambda^2 \{978 + 2969 \cdot \mu - 10351 \cdot \mu^2 + 6648 \cdot \mu^3\} \\ & + \lambda^3 \{1206 - 4826 \cdot \mu + 8366 \cdot \mu^2 - 4603 \cdot \mu^3\}\} \end{aligned} \quad (9.7)$$

Where $\mu = b/a$ and $\lambda = b/d_1$. Equations (9.6) and (9.7) are accurate within the range $0 \leq b/a \leq 1.0$ and $0 \leq b/d_1 \leq 0.8$.

The polynomial forms of these correction factors presented by Isida et al. (1984b) cover only 6 and 12 o' clock position. The magnification correction factor, Equations (9.8) and (9.9) determined by Fett et al. (1990) in combination with Equation (9.10) allows calculation of the correction factors for any point on the crack circumference. For ease of comparison, both polynomials form will be utilised in the calculation procedure.

$$\begin{aligned} \ln M_1 = & \{0.3826 - 1.399 \cdot \mu + 2.037 \cdot \mu^2 - 0.9213 \cdot \mu^3\} \lambda^2 \\ & + \{-4.4698 + 2.446 \cdot \mu - 4.892 \cdot \mu^2 + 2.5573 \cdot \mu^3\} \lambda^3 \\ & + \{0.7965 - 1.594 \cdot \mu + 2.931 \cdot \mu^2 - 1.5653 \cdot \mu^3\} \lambda^4 \end{aligned} \quad (9.8)$$

$$\begin{aligned} \ln M_2 = & \{0.2597 - 1.251 \cdot \mu + 1.920 \cdot \mu^2 - 0.9348 \cdot \mu^3\} \lambda^2 \\ & + \{-1.1631 + 2.233 \cdot \mu - 4.270 \cdot \mu^2 + 2.2773 \cdot \mu^3\} \lambda^3 \\ & + \{0.1327 - 1.424 \cdot \mu + 2.681 \cdot \mu^2 - 1.4283 \cdot \mu^3\} \lambda^4 \end{aligned} \quad (9.9)$$

Where $\mu = b/a$ and $\lambda = b/d_1$. Equations (9.8) and (9.9) are accurate within the range $b/a \geq 0.3$ and $b/d_1 \leq 0.9$.

9.2.1.2 Crack tip at long axis of the crack - 3 o' clock position

A comprehensive set of solutions were presented by Guozhong et al. (1996) for mode I stress intensity factors for embedded elliptical cracks in finite thickness plates under uniform tension. A wide range of parameters including the shape, size and location of the crack was studied in this reference.

The results presented in tabular form as a function of the dimensional form of the shape, size and location of the crack were compared with solutions from Isida et al. (1984b) for point A and point B. The correlation was found to be good. There was no basis for comparing the tabulated stress intensity factors for the point on the long crack axis (3 o' clock position) because the results obtained by Isida et al. (1984b) were only available for point A and B.

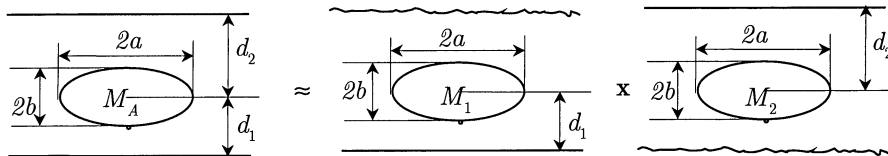


Figure 9.2 Concept of front surface and back surface corrections

Fett et al. (1997) proposed a magnification factor, equation (9.10) to estimate the angular dependency.

$$M(\phi) \cdot \left[\sin^2 \phi + \left(\frac{b}{a} \right)^2 \cdot \cos^2 \phi \right]^{-\frac{1}{4}} = \begin{cases} M_B + (M_A - M_B) \cdot \sin^2 \phi & \phi \geq 0 \\ M_B & \phi < 0 \end{cases} \quad (9.10)$$

Hence, for 3 and 9 'o clock position on the elliptical crack, the magnification correction factor is given by

$$M_{(C,D)} = \left(\frac{b}{a} \right)^{\frac{1}{2}} \cdot M_B \quad (9.11)$$

Similar to equations (9.2) and (9.3), the stress intensity factor equation at point C and D (Figure 9.1) is given by

$$K_{I,C,D} = \Delta S \cdot \frac{\sqrt{\pi \cdot b}}{\Phi} \cdot M_{C,D} \quad (9.12)$$

9.3 Elliptical Crack Under A Linear Stress Distribution

The geometry correction factor presented above was for the case of embedded elliptical flaw subjected to uniform tension.

A convenient approximate formula to account for the effect of bending load was given by Fett et al. (1990) relating the geometry correction factor in bending as a factor of the correction factor obtained in pure membrane case, Equations (9.13) - (9.17).

$$M_A^b \cong M_A^m \cdot \left(1 - 2 d_1/t + b/t \right) \quad (9.13)$$

$$M_B^b \cong M_B^m \cdot \left(1 - 2 d_1/t - b/t \right) \quad (9.14)$$

$$M_{C,D}^b \cong M_A^m \cdot \left(1 - 2 d_1/t \right) \quad (9.15)$$

The superscript *b* and *m* represent the bending and membrane case respectively.

The stress intensity factor for the general linear loading is given by

$$\Delta K_{I,N} = (\Delta \sigma_m \cdot Y_m + \Delta \sigma_b \cdot Y_b) \cdot \sqrt{b} \quad (9.16)$$

Where

$$Y(\phi) = \sqrt{\frac{\pi}{\Phi}} \cdot M(\phi) \quad (9.17)$$

SUMMARY

Two main methods were used to estimate the stress intensity factors for the embedded elliptic crack

1. Using Isida et al. (1984b) for point A and point B with Guozhong et al. (1996) for point C
2. Using Fett et al. (1997) for point A, B and C.

Linear superposition of membrane and bending stress intensity factor under combined loading was applied.

10 FRACTURE MECHANICS-BASED FATIGUE LIFE METHODS

Fatigue crack growth is governed by the cyclic variation of the stress-strain field close to the crack tip. This enables the use of fracture mechanics to solve fatigue-related problems.

In particular, fracture mechanics may be used to calculate the cycle by cycle growth of a fatigue crack, from an initial defect to final failure.

In the following, this tool (i.e. fracture mechanics) will be utilised to estimate the fatigue life of a welded titanium pipe containing an embedded elliptic crack close to one of the plate surfaces.

10.1 Fatigue Crack Growth Rate

Fracture mechanics model for calculating internal crack growth was developed for an embedded elliptical crack in a fusion weld of titanium riser pipe material.

Various empirical formulations have been presented in the literature for the fatigue crack growth for stages 1, 2 and 3 (Fatigue handbook, 1985.). Others

covers the threshold and the linear portion of PE crack growth region e.g. Klesnil et al. (1972) and Donahue et al. 1972). Priddle (1976) proposed a growth law starting from Forman's equation to cover the three regions in the fatigue crack growth curve.

Schematically, regions 1, 2 and 3 are shown in Figure 10.1.

The most commonly used relation for calculating fatigue crack growth using fracture mechanics is the Paris-Erdogan relation which expresses the relationship between crack growth rate and the stress intensity factor range, equation (10.1). It is conservative in the sense that it covers only the linear portion of the crack growth curve, neglecting threshold effects.

$$\frac{db}{dN} = C \cdot (\Delta K)^m \quad (10.1)$$

The Paris-Erdogan relation was chosen for the crack growth calculations, due to its simplicity, and availability of data for titanium alloys.

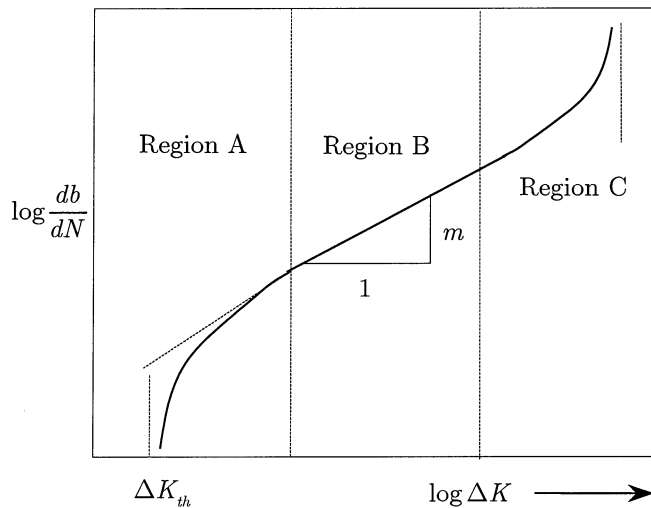


Figure 10.1 Crack growth rate curve. Region A, B and C denoted threshold, Paris-Erdogan and final failure region respectively.

Details for calculating the stress intensity factor are given in Chapter 9. C and m are the material constants obtained from crack measurements on standard notched specimens using standardised test methods (ASTM, 1993).

10.1.1 Threshold region

In a situation where the crack size is very small and the values of ΔK are very low, which is the case in the early stage of high cycle fatigue crack growth, adopting the Paris-Erdogan equation would be conservative.

As part of further refinement of the fracture mechanics model for fatigue crack growth, a crack growth expression involving the existence of the crack growth threshold could be employed to predict the fatigue crack growth life.

The threshold condition gives the fatigue limit within the LEFM regime at which for a given cyclic stress level the crack will not propagate, or for a given crack depth the stress range is insufficient to cause propagation (Miller, 1991). Alternately, it is a condition below which a crack will propagate at a slow rate (less than 10^{-10} m/cycle) (Mall, et al. 1990).

The empirical model of Donahue et al. (1972) was adopted which covers both the threshold and Paris-Erdogan region of the crack growth curve expressed as

$$\frac{db}{dN} = C \cdot (\Delta K - \Delta K_{th})^m \quad (10.2)$$

The fatigue life represented by equation (10.2) is obtained iteratively by stress intensity factor updating as the crack grows, i.e.

$$b_n = b_i + \sum_{i=1}^n f(\Delta K_i) \quad (10.3)$$

Where n is the number of load cycles.

10.1.2 Crack growth in three dimensions

For an elliptical crack the stress intensity varies along the crack front. In principle, crack growth should be calculated for each point on the crack front.

The assumption made by van Delft et al. (1986) was that for a semi-elliptical surface crack, a crack extension should lead again to a semi-ellipse. This assumption is very vital in reducing the infinite number of possible crack increments in three-dimensional problems.

Using the assumption made by van Delft et al. (1986), it is sufficient to consider crack extension in crack depth and crack width direction only. This method was extended to the embedded elliptical crack problem by Fett et al. (1990). Three different models for crack extension were considered, of which a model with constant half-axis was recommended.

With this model, four degrees of freedom is possible where each of the four half axes may be changed separately. It is sufficient to consider the growth in two degrees of freedom as shown in Figure 10.2a, here d_1 will vary throughout the cycle by cycle growth of the crack.

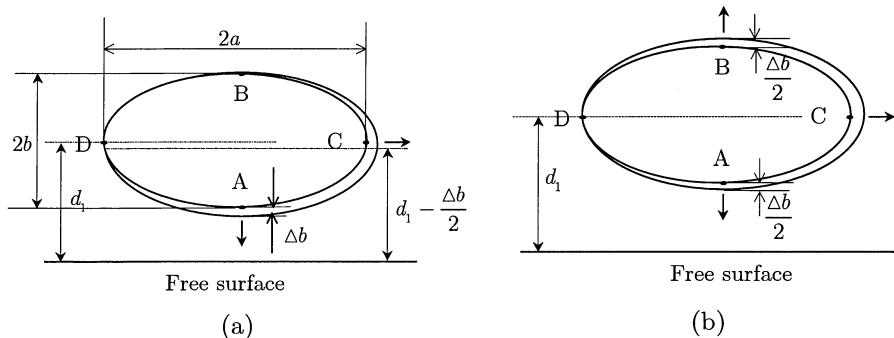


Figure 10.2 Cycle by cycle crack extension. (a) With constant half-axis – growth in two degrees of freedom, d_1 varied. (b) Modified form of (a), growth in 3 degrees of freedom, d_1 constant.

Assuming d_1 to be constant during the crack growth phase, the model can be extended as shown in Figure 10.2b, showing growth in three degrees of freedom while maintaining the crack ellipticity.

10.1.3 Cracks growing from internal defects

Under fatigue loading, and owing to the three-dimensional nature of an internal elliptical flaw, equation (10.2) could be applied in the four directions of the principal axes of an elliptical crack following the crack extension models recommended by Fett et al. (1990).

$$\frac{db}{dN} = C \cdot \left(\Delta K_{\left(\pm\frac{\pi}{2}\right)} - \Delta K_{th} \right)^m \quad (10.4)$$

$$\frac{da}{dN} = C \cdot \left(\Delta K_{(0,\pi)} - \Delta K_{th} \right)^m \quad (10.5)$$

Where (cfr. Figure 9.1)

- $\Delta K_{\left(\pm\frac{\pi}{2}\right)}$ = Stress intensity factor range at the short axis of the ellipse close to the front surface (point A, $\phi = -\frac{\pi}{2}$) and back surface (point B, $\phi = \frac{\pi}{2}$)
- $\Delta K_{(0,\pi)}$ = Stress intensity factor range at the long axis of the ellipse, (point C, $\phi = 0$) and (point D, $\phi = \pi$)
- ΔK_{th} = Threshold stress intensity factor
- $\frac{db}{dN}$ = Crack depth extension per load cycle
- $\frac{da}{dN}$ = Crack length extension per load cycle

Equations (10.4) and (10.5) can be applied, since the crack length and the crack depth are sufficient parameters for the description of the crack front.

10.2 Form Factors for the Stress Intensity Factor

A reliable estimate of the stress intensity factor is obtained with due consideration of the crack shape correction, influence of the weld geometry, finite thickness correction, interaction between adjacent defects etc. Interaction between adjacent defect has been considered in Chapter 8.

10.2.1 Influence of the weld geometry

In reality, the crack is located in the weld. The stress intensity form factor for embedded defect obtained in Chapter 9 does not account for the influence of the weld geometry.

To consider the influence of weld geometry, only the stresses in the intact structure at the location of the crack will contribute to the stress intensity factor. The stress distribution was obtained from Chapter 5 from experimental as well as finite element analyses.

The local stresses obtained both in the as-welded condition and after weld profile machining can be decomposed into membrane and bending components. Since the stress intensity factor is a linear function of the stress; the contribution from different stress fields can be superposed Equation (10.6).

$$\Delta K_I = (\Delta\sigma_m \cdot Y_m + \Delta\sigma_b \cdot Y_b) \cdot \sqrt{b} \quad (10.6)$$

Where Y_m and Y_b are the geometric functions for tension and bending.

10.2.2 Finite size corrections

In the development of Equations (9.2), (9.3) and (9.12) a small crack close to one of the plate surfaces in a finite thickness plate subjected to uniform tension was considered. These equations were corrected for finite thickness using the concept of front surface and back surface corrections presented by Isida et al. (1984b).

Guozhong et al. (1996) calculated the maximum deviation of this model compared with an embedded elliptical crack in a semi-infinite plate to be 5%. Essentially for a growth of near surface elliptic crack, magnification correction factor for a semi-infinite plate will be an approximation for finite thickness plates.

10.2.3 Effect of crack closure

In this study the level of crack closure was not known, hence the effect of crack closure was not accounted for. Klesnil and Lukas (1992) showed that closure was absent in the case of very small cracks due to the limited wake created by the growing crack (Klesnil and Lukas, 1992).

10.2.4 Crack growth relations for internal /surface cracks

For surface breaking pores or for an internal crack that grows and breaks through the free surface before reaching the critical size, a common form of modelling of a surface defect was applied. From Figure 9.1, the limiting crack geometry assumed for the transition from internal to surface crack is given by

$$d_1 - b \leq 10^{-6} m \quad (10.7)$$

When this condition was reached, as a conservative approximation, the crack shape was re-categorised as a semi-elliptical crack and the stress intensity factor calculation followed from available stress intensity factor calculation methods for such shape, Newman et al. (1981). Alternative stress intensity factor calculation methods that can be used are, Nisitani et al. (1974), Isida et al. (1984a) etc.

The rate of crack growth given by equation (10.2) can be applied in two directions of the principal axes of the semi-elliptical crack until the critical size is reached.

10.3 Fatigue initiation life

The fatigue life can be subdivided into fatigue life in a crack initiation period and a crack growth period (Fatigue Handbook, 1985). In a machined and non-welded component, fatigue initiation life may be very significant for the overall fatigue life. The initiation life is in general dependent on the microstructure and strength of the material.

In a welded component, a common assumption is that cracks already exist in the weld. Consequently the fatigue initiation life may be neglected, and fatigue life may be calculated using fracture mechanics methods.

Fan et al. (1991) used the eigen-strain method to model the fatigue crack initiation life. A normalised form of crack initiation life was presented in terms of applied shear stress, plastic modulus, crack geometry data and Poisson's ratio.

Kam (1994) related the initiation life to strain range, mean stress and some material parameters (e.g. fracture ductility and fracture strength) by combining Neuber's rule and the material cyclic stress strain curve e.g. the Ramberg-Osgood formula.

The initial defects in the titanium welds were essentially pores. In fracture mechanics terms, a pore is a blunt defect. However, the origin of the pores is believed to be from hydrogen, which is known to lead to embrittlement of titanium. Atteraaas et al. (1999) reported evidence of brittle mode of fracture close to such pores, in fatigue loading. For this reason, the pores were considered as initial cracks, and a fatigue initiation phase was neglected in the analysis.

11 FATIGUE CRACK GROWTH IN WELDED TITANIUM 6-4 ALLOY IN THE PRESENCE OF EMBEDDED DEFECT.

In chapter 10 the procedure for crack growth calculations developed by van Delft et al. (1986) was discussed. This procedure was developed for analysis of semi-elliptic cracks in tubular joint.

The method was extended for estimating the fatigue life of a welded titanium pipe containing an embedded elliptic crack close to one of the free surfaces (Figure 9.1).

Input parameters

The initial crack size ($2b_i, 2a_i$), material constants and stress range are the input parameters, where b_i and a_i are the respective half crack depth and half crack length for an elliptic crack with the major axis parallel to the free surface, Figure 9.1.

Crack depth increment

Dai et al. (1998) developed a numerical procedure for calculation of crack growth, using a stepwise constant stress intensity factor during a small but finite number of cycles, ΔN . They suggested 500 cycles or less when there is a steep variation of stress intensity factor with crack growth, e.g. at breakthrough of a free surface.

$$\Delta b = C \left(\Delta K_{\left(\pm \frac{\pi}{2}\right)} - \Delta K_{th} \right)^m \cdot \Delta N \quad (11.1)$$

The crack depth increment Δb is calculated according to Equation (11.1). The parameters in the equation have been obtained from the initial size and shape of the crack. The parameters in Equation (11.1) were defined in section 10.1.3.

Stress intensity factor

The stress intensity factors for the symmetry points on the crack front are based on the assumption that the initially elliptical crack remains elliptical as crack grows. The symmetry locations are points on the elliptic crack close to front surface (6 o' clock position), back surface (12 o' clock position) and at the sides (3, 9 o' clock position), cfr. Figure 9.1.

Influence of weld geometry can be accounted for through a superposition of the tension and bending contribution obtained in the as-welded and machined condition.

Crack extension in the length direction

For a small increment in depth direction, the crack extension in the length direction is given by

$$\Delta a = \Delta b \cdot \left(\frac{\Delta K_{(0)} - \Delta K_{th}}{\Delta K_{\left(\pm \frac{\pi}{2}\right)} - \Delta K_{th}} \right)^m \quad (11.2)$$

Number of cycles during the crack extension

Number of cycles for a given increment in crack growth is calculated from the differential of Equation (10.4).

$$\Delta N = \frac{\Delta b}{C} \left(\frac{1}{\Delta \bar{K}_{(\pm \frac{\pi}{2})} - \Delta K_{th}} \right)^m \quad (11.3)$$

With the same reasoning given by van Delft et al. (1986), there is an increase in stress intensity factor as the crack extends from b_i, a_i to $b_i + \Delta b, a_i + \Delta a$. As a result, the number of cycles given by equation (11.3) will be slightly higher than expected.

A better estimate can be obtained from

$$\Delta N = \frac{\Delta b}{C} \left(\frac{1}{\Delta \bar{K}_{(\pm \frac{\pi}{2})} - \Delta K_{th}} \right)^m \quad (11.4)$$

Where

$$\Delta \bar{K}_{(\pm \frac{\pi}{2})} = \Delta K_{(\pm \frac{\pi}{2})} \cdot \left(\frac{b_i + \Delta b}{b_i} \right)^{\frac{1}{2}} \quad (11.5)$$

Crack size and number of cycles for the next iteration step

Based on the crack extension model in section 10.1.2, four possible crack increments exist for point A, B, C and D.

Point A and B

A crack increment Δb in one cycle leads to a new ellipse approximated by the new geometrical data

$$\begin{aligned} 2b_i &= 2b_i + \Delta b \\ 2a_i &= 2a_i \\ d_1 &= d_1 \pm \frac{1}{2} \cdot \Delta b \\ N_i &= N_i + \Delta N \end{aligned} \tag{11.6}$$

Similarly,

Point C and D

$$\begin{aligned} 2b_i &= 2b_i \\ 2a_i &= 2a_i \mp \Delta a \\ d_1 &= d_1 \\ N_i &= N_i + \Delta N \end{aligned} \tag{11.7}$$

This new data provides a starting point for the next block until the critical or final crack size is reached. However, if the critical size is not reached before the crack breaks onto the free surface, as explained in section 10.2.4, the crack is treated as a semi-elliptic crack and polynomials equation for stress intensity factor calculations can be used.

Critical defect size

Critical defect is the size which under the given load will lead to unstable fracture or tearing. Geometrical conditions (plate thickness, distance to edge, etc.) and material properties will affect the critical defect size. The calculated critical defect sizes for steel material could be determined on the basis of the fracture assessment procedure described in the British Standard 7910:1999.

Fracture assessment methods are not developed for titanium. However, after the crack has grown to the size of some few millimetres, remaining life will be very short, Figure 11.1a. Based on simplified calculations, and engineering judgement, critical defect size for fatigue life calculation were assumed as shown in Figure 11.1b

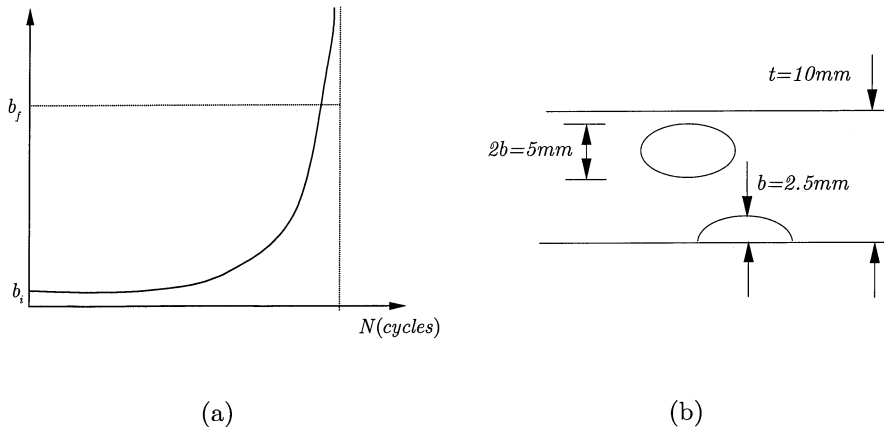


Figure 11.1 (a) Crack depth, b as a function of the number of cycles to failure.
(b) Critical defect size for a semi-elliptical surface crack and elliptical embedded flaw.

12 FRACTURE MECHANICS ANALYSIS RESULTS

The results are presented based on two stress intensity factor formulations given in Chapter 9. Two main cases were considered for the crack orientation, namely; crack with $b < a$ and $b > a$ (Figure 12.1). For some cases the results for a crack in an infinite plate was compared with analysis corrected for finite thickness.

Fatigue life formulation model based on the Paris-Erdogan crack growth relation (1963), and with an implied threshold given by Donahue et al. (1972) were considered (Figure 10.1). Two crack growth models with respect to the distance of the defect from the free surface were considered, namely; crack increment with constant axial distance to the free surface and crack increment with varying distance to the free surface (Figure 10.2).

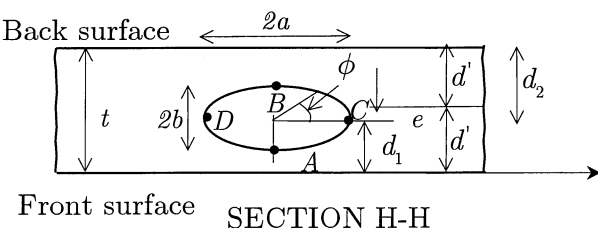


Figure 12.1 Elliptical crack embedded in plate subjected to uniform tension.

From the experimental and finite element results, the percentage of bending was estimated to be 15% of the applied stress. The effect on the fatigue life was assessed for some of the test data.

12.1 Stress Intensity Factor Model

12.1.1 Case 1: $b < a$

Method 1

The stress intensity solution given by Fett et al. (1997) is valid for points A, B, C and D of the crack front (Figure 12.1) within the range; $b/a \geq 0.3$ and $b/d_1 \leq 0.9$. For Method 1 this model was applied.

Method 2

The polynomial equation derived by Isida et al. (1984b) is accurate for points A and B within the range; $0 \leq b/a \leq 1.0$ and $0 \leq b/d_1 \leq 0.8$. The table of stress intensity data given by Guozhong et al. (1996) provides solutions for points C and D, valid for $0.25 \leq b/a \leq 1.0$ and $0.2 \leq b/d_1 \leq 0.8$.

For some of the specimens analysed, $b/d_1 < 0.2$. This limitation for points C and D was solved using two procedures, which were derived from the following initial models:

1. Linear extrapolation of the stress intensity solution to cover $b/d_1 < 0.2$.
This was referred to as Isida_extr in Figure 12.7.
2. Assuming stress intensity for point C is the average of that of points A and B for $b/d_1 < 0.2$.
3. Using the Fett et al. (1997) formula only for cases with $\frac{b}{d_1} < 0.2$ in the analysis. Referred to as Isida_Fett in Figure 12.7.

Initial studies showed that there were no large variations in the results obtained with the three models. Thus, only solutions for models 1 and 3 are presented. In the real sense the contributions will not affect the crack growth calculations significantly.

12.1.2 Case 2: $b > a$

Method 1 in the section above can also be applied for a defect with large crack depth compared to the crack length, i.e. $b > a$. The accuracy was not immediately known because the solution was derived for a crack with $b < a$. It is important to establish the accuracy of this method for the case with $b > a$.

Method 2 is not valid for case 2, i.e. $b > a$. However, an estimate of the solution can be obtained based on the two models proposed below. The two models below will be essential to validate the solution obtained from Method 1 above.

Model 1: Crack re-orientation

Crack re-orientation is obtained by rotating the initial crack by 90° about the crack centre. Now, the crack depth 'b' assumes the value of the crack length 'a' and vice versa (Figure 12.2). The implication is that the crack depth is reduced and the crack length increased. This means increased no of cycles to failure.

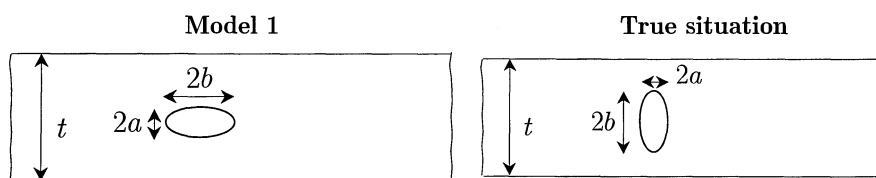


Figure 12.2 Extending Method 2 for a crack with $b > a$ using model 1

Furthermore, the distance of the crack to the free surface is also increased. This implies that the crack will spend more time growing from an internal defect to a surface crack.

Model 2: Crack enlargement at constant aspect ratio

Crack growth is modelled by keeping the initial crack depth ‘ b ’ constant, and increasing the crack length ‘ a ’ while keeping the aspect ratio of the original crack constant (Figure 12.3)

From Figure 12.1, for case 2 with $a < b$, this implies

$$a_{new} = \frac{b_{initial}^2}{a_{initial}}, \quad b_{new} = b_{initial} \quad (12.1)$$

This is conservative because the fatigue life will be lower than in reality. In the real sense, the fatigue life will lie between that obtained in Model 1 and Model 2.

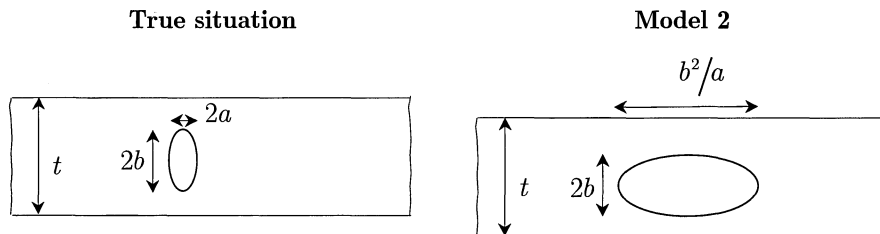


Figure 12.3 Extending Method 2 for a crack with $b > a$ using model 2

12.2 Model For Crack Increment And Stress Intensity Factor Updating

- Crack increment with constant distance of the defect from its axis to the plate surface (Figure 10.2b)
- Crack increment with varying distance of the defect from its axis to the plate surface (Figure 10.2a)

Crack increment with constant distance of the defect from its axis to the plate surface

The stress intensity factor is updated keeping the distance of the defect from its axis to the plate surface constant.

The following cases were considered:

1. Effect of finite thickness plate compare to solution in semi-infinite solid, under tensile loading condition. The stress intensity factor solution given by Fett et al. (1997) referred to as Method 1 was utilised in calculating the fatigue life.
2. Given that the membrane and bending stress is 85% and 15% of the applied stress range respectively, the fatigue life is calculated using Fett et al. (1997) stress intensity factor solution for a semi-infinite solid.

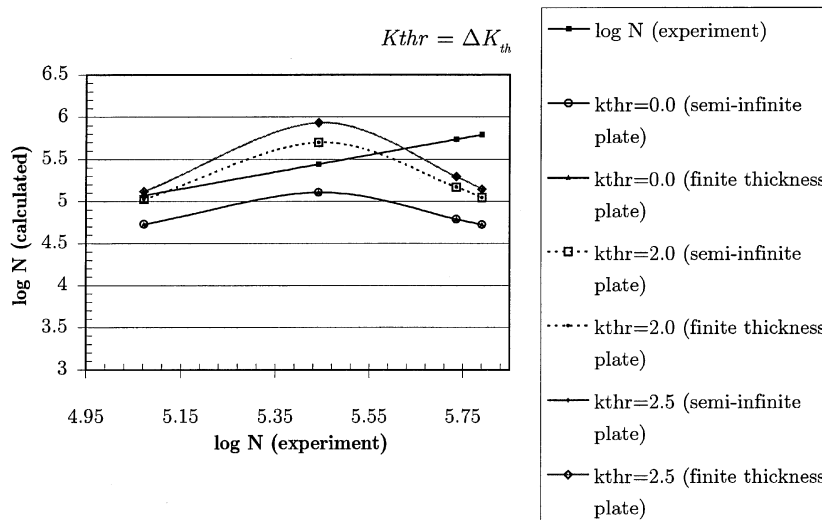


Figure 12.4 Semi-infinite solution compare with finite thickness solution and $d_1 = \text{constant}$. Reference curve for the experimental result is also plotted.

In Figure 12.4, the calculated fatigue life is shown using Method 1 (Fett et al., 1997). The stress intensity factor solution in a semi-infinite solid is compared with finite thickness plate under tensile loading condition. It is assumed here that the distance of the defect from its axis remains constant throughout the stress intensity factor updating cycles i.e. $d_l = \text{constant}$.

In general, the maximum deviation of the fatigue life obtained for defect in finite thickness plate and that in a semi-infinite body is less than 0.2%, hence the rest of the analyses were performed assuming stress intensity factor solution for a semi-infinite solid.

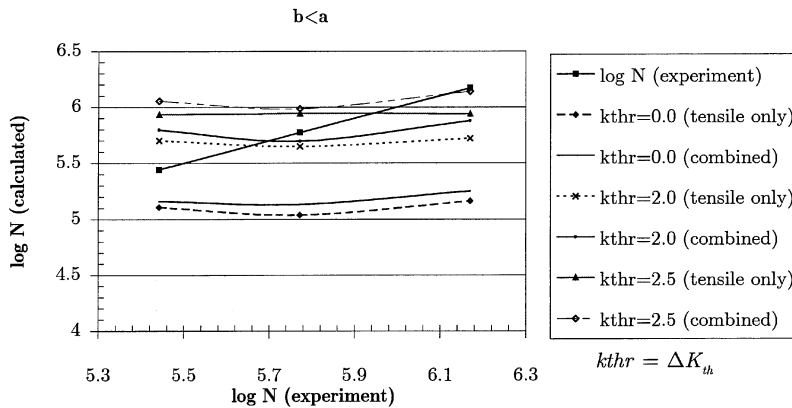


Figure 12.5 Method 1: Calculated fatigue life is compared under pure membrane and combined loading conditions i.e. membrane stress (85% stress range) and bending (15% stress range). $d_l = \text{constant}$. Reference curve for the experimental result is also plotted.

Calculated fatigue life is presented in Figure 12.5 and Figure 12.6 for $b < a$ and $b > a$ respectively based on Method 1 under combined loading condition i.e. membrane (85% stress range) and bending (15% stress range). It is also assumed that the distance of the defect from its axis remains constant throughout the stress intensity updating cycles i.e. $d_l = \text{constant}$.

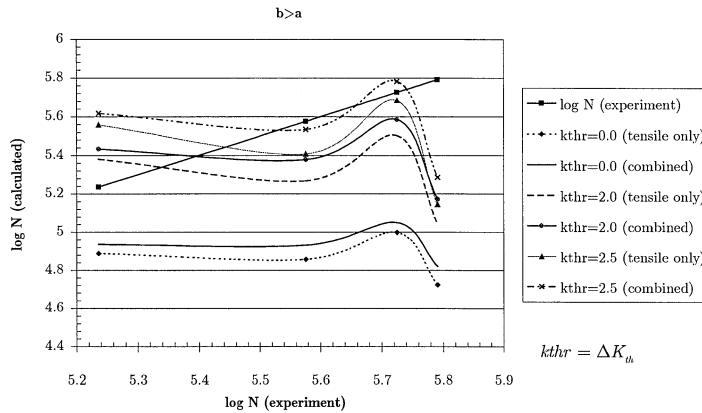


Figure 12.6 Method 1: Calculated fatigue life is compared under pure membrane and combined loading condition i.e. membrane stress (85% stress range) and bending (15% stress range). $d_1 = \text{constant}$. Reference curve for the experimental result is also plotted.

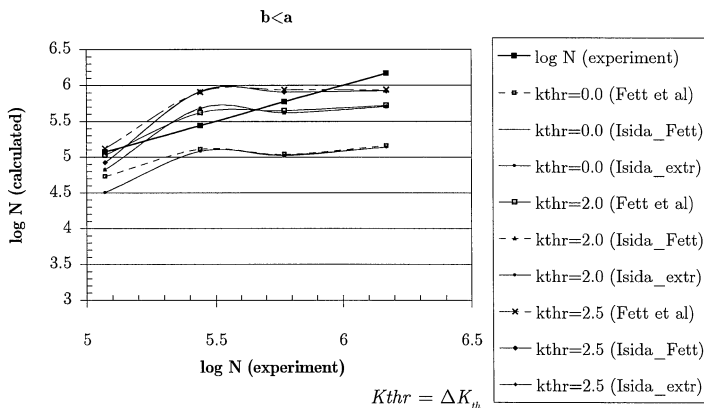


Figure 12.7 Method 1 (Fett et al., 1997) and Method 2 (Isida_Fett / Isida_Extr) are compared for case 1 with $b < a$ under tensile loading condition. Reference curve for the experimental result is also plotted.

In Figure 12.7 the calculated no of cycles to failure for Method 1 and 2 described in section 12.1.1 was compared with the experimental value.

Verification of Models 1, 2 and Method 1 for case 2: $b > a$

In Figure 12.8, Models 1, 2 and Method 1 are compared. As discussed in section 12.1.2, Model 1 gives a higher fatigue life, while Model 2 gives a conservative estimate of the fatigue life. The true solution will lie between that given by Model 1 and Model 2. This is obvious from the result obtained from Method 1 (Fett et al., 1997).

This is a sufficient justification for using Method 1 (Fett et al., 1997) for the stress intensity solution calculation for all values of b and a within the validity range.

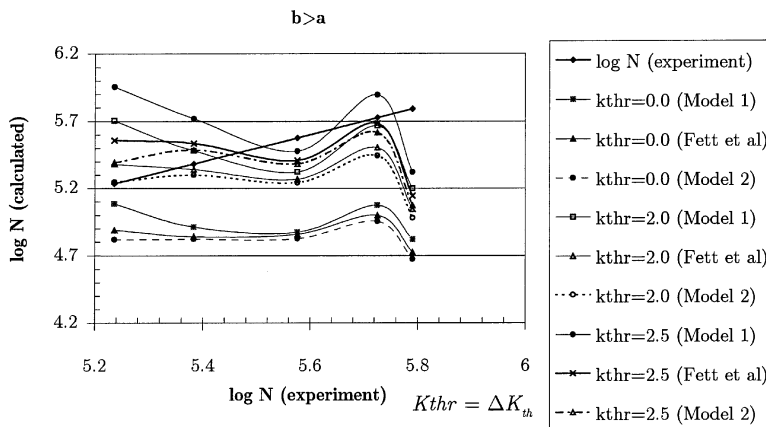


Figure 12.8 Model verification for the calculated fatigue life for case 2 with $b > a$. Reference curve for the experimental result is also plotted.

Crack increment with varying distance of the defect from its axis to the plate surface

In Figure 12.9, the fatigue life is calculated on the assumption that the distance of the defect from its axis decreases as the crack depth increases until it reaches a point where $d_l - b \approx 0.0$ (Figure 10.2a). For every increment, Δb , in crack depth $d_l = d_l - \Delta b/2$

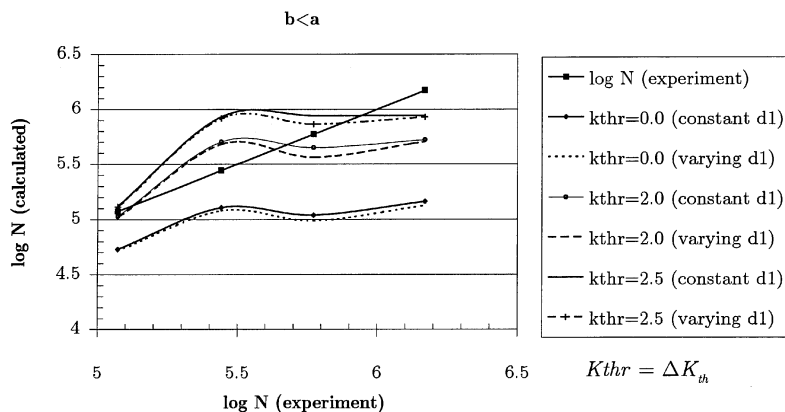


Figure 12.9 Fatigue life calculated compare for constant d_l and varied d_l using Method 1. Reference curve for the experimental result is also plotted.

From above, Method 1 used with varying or constant crack distance to the plate surface predicts almost same result.

12.3 Selection of Threshold for The Crack Growth Formula

For Grade 29 TIG weld metal, $m = 3.0$, $C = 2.8 \cdot 10^{-11}$ Baxter et al. (1997).
 $\Delta K_{th} = 4.0$ (Farhangdoost and Provan, 1996).

With these parameters, Equation (10.2) seriously overestimated the fatigue life and makes the fracture mechanics result unreasonable. Three important things to learn from this are

1. The initial crack size to fit Equation (10.2) might be larger than the defect size
2. Assuming all the material parameters to be correct, the rate of crack growth for such defect might be larger than predicted by Equation (10.2).
3. The threshold is an important parameter which is greatly influenced by the residual stress level.

Clearly, the first deduction cannot be proved. An easy way out is to reduce the threshold level. The threshold levels that best fit equation (10.2) is $2 \leq \Delta K_{th} \leq 2.5$ of which $\Delta K_{th} = 2.25$ gave a better fit.

Analytical integration of equation (10.2) assuming constant form factor yields

$$N(a_i, \infty) = \frac{2a_i^{1-\frac{m}{2}} \cdot (1 - \frac{\Delta K_{th}}{K})^{1-m} \cdot (1 - m + \frac{\Delta K_{th}}{K})}{(1 - m)(2 - m) \cdot C \cdot (F\Delta S\sqrt{\pi})^m} \quad (12.2)$$

Where $K = F\Delta S\sqrt{\pi a_i}$

Fatigue life to a finite crack length is obtained (Mainçon, 1998) by:

$$N(a_i, a_f) = N(a_i, \infty) - N(a_f, \infty) \quad (12.3)$$

With $\Delta K_{th} = 0$, equation (12.3) Fatigue Handbook (1985) gives:

$$N(a_i, a_f) = \frac{a_i^{1-\frac{m}{2}} - a_f^{1-\frac{m}{2}}}{(m/2 - 1) \cdot C \cdot (F\Delta S\sqrt{\pi})^m} \quad (12.4)$$

In Figure 12.10 for the case $b < a$ the Paris-Erdogan relation (Equation (12.2) with $\Delta K_{th} = 0$) grossly underestimated the fatigue life. Considering the scatter in the experimental data, iterated form of Equation (10.2) i.e. assuming F is not constant predicts a fatigue life within 0.4 and 2.2 times the experimental life. A ratio between 0.2 and 1.6 times the experimental life is obtained using equation (12.2) i.e. assuming F is constant.

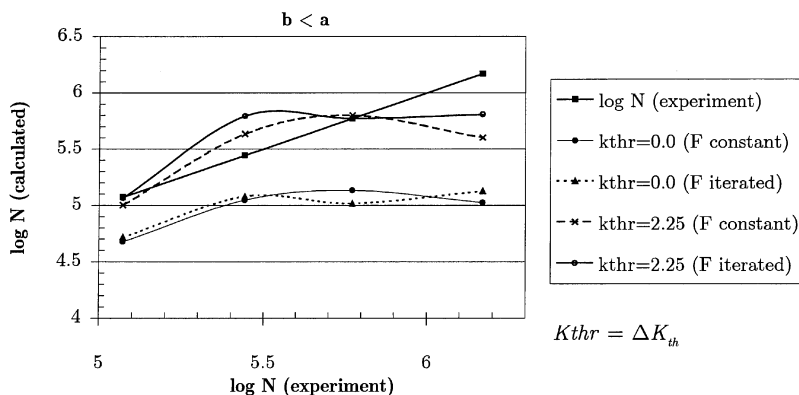


Figure 12.10 Iterated form of equation (10.2) i.e. assuming F is not constant and equation (12.2) i.e. assuming F is constant. Case $b < a$. Reference curve for the experimental result is also plotted.

For a defect with $b > a$ (Figure 12.11), the maximum stress intensity occurs at point C (Figure 12.1). Using this value in equation (12.2), the fatigue life is underestimated. If the stress intensity of point A (close to the free surface) is used instead of at point C, equation (12.2) predicts a better estimate. Of course, the initial form factor has been generated based on Method 1 (Fett et al., 1997).

In reality, as the crack grows (i.e. as b/d_1 increases), the maximum stress intensity tends to move towards point A. Thus using the stress intensity factor of point A does not introduce unnecessary error.

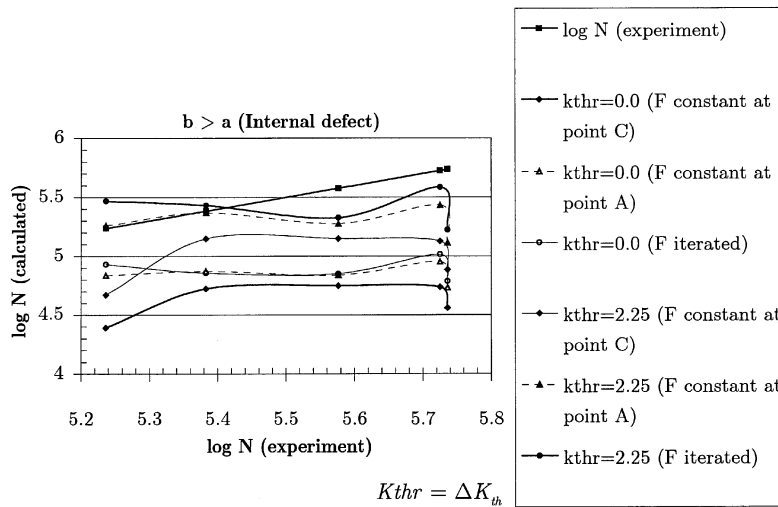


Figure 12.11 Iterated form of equation (10.2) i.e. assuming F is not constant and equation (12.2) i.e. assuming F is constant. Case $b > a$. The upper result is obtained using the stress intensity factor for point C, while the result below is calculated using the stress intensity factor of point A (Figure 12.1). Reference curve for the experimental result is also plotted.

The experimental fatigue life is compared with the calculated fatigue life in Figure 12.12 for surface defects. The stress intensity factor solution for semi-elliptic surface crack by Newman and Raju (1981) was used with two crack growth model (Paris-Erdogan, 1963 and Donahue et al., 1972 with an implied threshold of 2.25). Additionally, the form factor was iterated during the cycle by cycle growth of the crack.

In general the result predicted by the Paris-Erdogan relation (1963) is conservative with a factor which range from 0.3 – 0.7 on the experimental life. With an implied threshold of 2.25 the calculated fatigue life fall within 0.6 – 1.7 times the experimental life, Figure 12.12

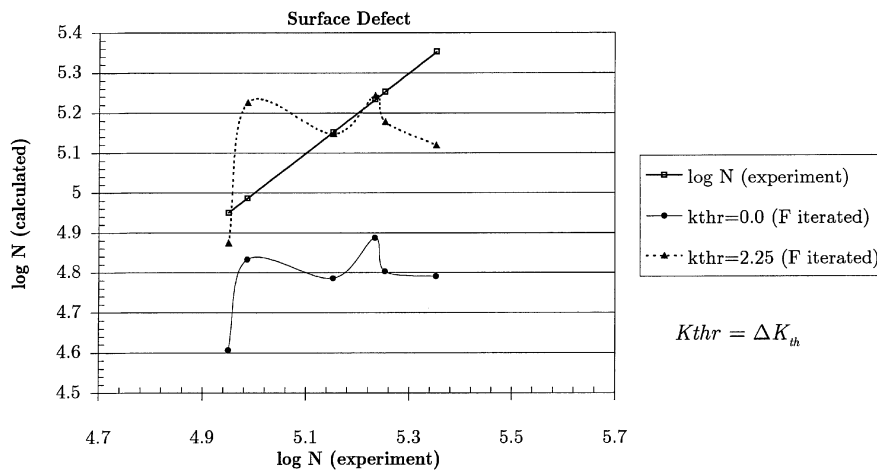


Figure 12.12 Estimation of fatigue life for surface defect using equation (10.2) i.e. F iterated. Reference curve for the experimental result is also plotted.

13 CONCLUSIONS AND RECOMMENDATIONS

13.1 Summary

The effect of embedded and surface breaking defects on the fatigue strength of titanium fusion welds was analysed experimentally and by fracture mechanics analysis.

Titanium pipe made from a medium strength alloy suitable for riser applications was girth welded using Tungsten Inert Gas welding. Coupon specimens were fatigue tested with constant amplitude axial loading. The stress distribution in the specimen geometry was calculated by solid Finite Element Analysis and compared with the stress distribution in the pipe. The effect of weld overfill was assessed.

A conclusion was that some level of misalignment and variability in the weld geometry apparently affected the stress distribution in the test specimen. A conservative approach for design was to assume the applied stress as fully tensile. This is justified because in a full section pipe, due to the radial stiffness of the cylindrical shell, misalignment and weld overfill does not give any secondary bending in a pipe.

Size, shape, orientation and relation to fatigue initiation were evaluated by fractography, using Scanning Electron Microscopy. A number of fatigue failures had been initiated from submillimetre pores in the interior of the weld.

Fatigue crack growth from internal and surface breaking defects was modelled using fracture mechanics. A procedure for calculating the fatigue life of a welded pipe containing cracks was presented.

Essentially, interaction between adjacent defects was included in the modelling based on BSI: PD 6493 (1991) using principles for recategorisation of cracks. The effect of finite size correction on the geometry factors for the stress intensity factor was studied using front surface and back surface correction given by Isida et al. (1984b).

Generally, the effect was less than 0.2% compared to the solution for a semi-infinite solid. As a result, the form factor was calculated based on stress intensity factor solutions for cracks in a semi-infinite solid. The reason for the closeness in the two results was because the cracks were located close to one of the free surfaces and were small compared to the cross-sectional dimension of the test pieces.

A computer code was written for crack growth calculation of a fatigue crack from an initial defect to final failure. The method was based on linear elastic fracture mechanics, and crack growth was characterised in terms of the stress intensity factor, ΔK . The method allows for updating of the stress intensity factor as the crack grows.

Two methods for stress intensity factor calculation (Isida et al., 1984b and Fett et al., 1997) were used and compared.

The parametric equations for stress intensity factor solutions given by Isida et al. (1984b) is suitable for elliptic cracks oriented with the major axis parallel to one of the free surfaces, for the tip of the crack at the short axis of the crack. The result was combined with the stress intensity solutions given by Guozhong et al. (1996) for the tip of the crack at the long axis.

The stress intensity factor solution given by Fett et al. (1997) is suitable for any point on the crack front.

The solution by Isida et al. (1984b) was extended to cover an elliptic crack with an aspect ratio greater than unity. Two methods were proposed namely; crack re-orientation and crack enlargement at constant aspect ratio. The solution given by Fett et al. (1997) is valid for an elliptic crack with the minor axis parallel and close to one of the free surfaces of the specimen in the thickness direction.

Two models for crack increment and stress intensity factor updating were used. Crack increment with varying distance of the defect from its axis to the plate surface (Fett et al. 1997), and crack increment with constant distance of the defect from its axis to the plate surface.

Two fatigue crack growth formulations were chosen viz.; Paris-Erdogan relation and the empirical model of Donahue et al. (1972) which covers both the threshold and the linear region (i.e. Paris-Erdogan region). The Paris-Erdogan relation underestimated the fatigue life by a factor of 2 - 4. The Donahue et al. (1972) model used with an implied threshold of $\Delta K_{th} = 2.25 \text{ MPam}^{\frac{1}{2}}$ gave better prediction with an estimated fatigue life within a factor of two of the experimental value. The assumed threshold values had a large effect on the computed fatigue life.

13.2 Concluding Remarks

Fatigue of TIG welded titanium is governed by pores. Good fatigue strength can be achieved by control of pores. The reliability of which depends on the level of Non Destructive Inspection (NDI).

The fracture mechanics model predicted a fatigue life within a factor of 2 of the experimental life. The predictions were based on integration of a crack

growth relationship with implied threshold, and data taken from the literature.

The fracture surfaces as shown by SEM images, were very rough. There is reason to believe that roughness-induced crack closure may have affected crack growth rates. However, no relevant data on this effect is available for quantitative modelling, and the effect was disregarded.

Residual stresses may also have had an effect. In this case, residual stresses on a macro-level were assumed to be small. This could be inferred from the welding process, which was TIG welding with a large number of strings, during which the residual stresses would decay due to the thermal cycling.

It was noted that when specimens were cut from the pipe, distortions were negligible. However, residual stresses on a micro-scale close to the pores may have been present, with a possible effect on the initial stages of crack growth.

The scatter in results is believed to be caused by these inherent uncertainties. For design applications, uncertainties must be accounted for by appropriate safety factors.

13.3 Recommendations for further studies

Crack growth formula

The present study deals with a crack size range 0.3 – 0.7mm. This lie within the maximum crack length considered to be microstructurally small cracks. This size was assumed to be the minimum crack size regarded as mechanically small to enable the use of LEFM. It might be important to use a different branch of fracture mechanics for the different phases of small crack growth in fatigue e.g. Miller (1991).

Threshold effect

A crack growth model with an implied threshold given by Donahue et al. (1972) was adopted. For the final analysis, a stress intensity threshold $\Delta K_{th} = 2.25 \text{ MPa}\sqrt{\text{m}}$ was assumed as a reasonable fit to the experimental data. The result indicated a large influence of the stress intensity threshold on the fatigue life. Improved crack growth models for the threshold region is needed.

Closure effects

In the selection of crack growth relation, crack closure effects may be an important consideration. It may be necessary to consider the effects of closure or be able to justify its preclusion in future analysis.

Crack initiation life

The fatigue life in a crack initiation period may be significant in the absence of brittle mode of fracture close to the pores. The pores are essentially the initial defects in the titanium welds. Models for crack initiation from two and three-dimensional internal defects may be necessary.

Transition from internal to surface crack

Modelling of the transition from internal to surface crack is affected by the validity range of the stress intensity factor solution adopted. Two situations could be obtained; firstly, at first calculation the aspect ratio b/a and or ratio of crack depth to crack distance from one of the free surfaces b/d_1 may fall outside the validity range of the stress intensity factor solution. Secondly, the critical defect size may not be reached in the course of crack growth from internal to surface defects whereas the validity range of the stress intensity factor may have been exceeded. Approximate solutions were given in Section 12.1. Though there were no significant differences between the solution

methods adopted, it may be necessary to account for this problem in future work.

Continuum Damage Mechanics CDM Approach

CDM provides a new approach to fatigue modelling and is able to model all three stages (crack initiation, stable crack growth and final fracture) of the fatigue fracture process using one model and one set of material parameters. Numerical implementation using finite element codes and experimental validation will be necessary (den Ouden, 2001).

REFERENCES

- ADACHI, S. (1987). *Mean strength dependence of fatigue strength in titanium alloys*. Dr. Ing. dissertation Hamburg Technical University.
- ALLEN, D., NEJAD, M., MIGLIN, B., PHIFER, E. and SMITH, J. (1998). *Steel catenary riser conceptual design and analysis for Bonga development*. Document No.: SDDSI 99-1024 for Shell Nigeria Exploration and Production Company, SNEPCO.
- ASTM (1993). E647-93. Philadelphia, U.S.A.: American Society for Testing and Materilas.
- ATTERAAS, L., ERIKSEN, T. and FOER, K. (1999). *Low frequency fatigue of titanium grade 29 in seawater at 150° C*. Seminar- Titanium Risers and Flow-lines, Trondheim.
- ATTERAAS, L. and FOER, K. (1998). *Fatigue of titanium grade 29 under cathodic “protection” in hot water*. Symposium on fatigue behaviour of titanium alloys. TMS Fall Meeting, Chicago, Illinois.
- BAUGUS, V., BAXTER, C. and TRIM, A. (1998). *Use of titanium taper joints in risers – The Neptune Field and Future Designs*. 17th International Conference on Offshore Mechanics and Arctic Engineering, OMAE 98, Lisbon.
- BAXTER, C., PILLAI, S. and HUTT, G. (1997). *Advances in titanium risers for FPSO's* Offshore Technology Conference, OTC 8409, Vol. 2, pp. 497 – 508, Houston, USA.

- BERGE, S. Private communication
- BERGE, S. (1998a). *Fatigue strength of titanium risers – effects of defects.* 17th Int. Conference on Offshore Mechanics and Arctic Engineering, Lisbon. (OMAE98-2209).
- BERGE, S. (1998b). *Fatigue of titanium fusion welds- models for assessment of defect sensitivity.* Symposium on fatigue behaviour of titanium alloys. TMS Fall Meeting, Chicago, Illinois.
- British Standard BS 7910: 1999, Guide on methods for assessing the acceptability of flaws in fusion welded structures. British Standards Institution 1999.
- BUITRAGO, J. and ZETTLEMOYER, N. (1998). *Fatigue design of critical girth welds for deepwater applications.* 17th International Conference on Offshore Mechanics and Arctic Engineering, OMAE98-2004
- CARLSEN, L. (1998). *Lecture notes on dynamics analysis of slender marine structures,* Institute of marine structures, Faculty of marine technology, NTNU, Trondheim, Norway.
- CHENG, W. and FINNIE, I. (1997). *Computation of Mode I stress intensity factors for three-dimensional bodies using displacements at an arbitrary location.* International journal of fracture no. 83, pp. 91 – 104.
- CLAYSON, A. (1999). *Fabrication of titanium pipe for riser and flow-line applications.* Seminar- Titanium Risers and Flow-lines, Trondheim.
- COLANGELO, V. J. and HEISER, F.A. (1987). *Analysis of metallurgical failures.* 2nd edition. A Wiley-Interscience publication.
- DAI, D., Hills, D., Hårkégard, G. and Pross, J. (1998). *Simulation of the growth of near-surface defects.* Engineering Fracture Mechanics, Vol. 59, No. 4, pp. 415-424.
- DAVIES, A. C. (1989). *The science and practice of welding,* Cambridge University Press, Vol. 1 and 2
- DEN OUDE N (2001). *Fatigue strength of laser welded steel.* Netherlands Institute of Metal Research, NIMR.

- DONAHUE, R. J., CLARK, H. M., ATANMO, P., KUMBLE, R. and McEVILY (1972). *Crack opening displacement and the rate of fatigue crack growth.* Int. J. of Fracture Mechanics, 8, pp. 209 – 219.
- EBARA, R., YAMADA, Y., and GOTO, A. (1983). *Corrosion – Fatigue behaviour of Ti-6Al-4V in a sodium chloride aqueous solution.* Corrosion Fatigue: Mechanics, Metallurgy, Electrochemistry, and Engineering. ASTM STP 801. T. W. Crooker and B. N. Leis, Eds., American Society for Testing and Materials, pp. 135 – 146.
- ENGESVIK, K. (1981). *Analysis of uncertainties in the fatigue capacity of welded joints.* Dr. Ing. Dissertation, Norwegian University of Science and Technology, Department of Marine Structures, Trondheim, Norway.
- Engineering Sciences Data, Item Number 82015 (May 1982). *Fatigue crack propagation rates and threshold stress intensity factor ranges for titanium alloy plate, bar and forgings.* The Royal Aeronautical Society, London.
- FALTINSEN, O. M. (1995). *Sea loads on ships and offshore structures.* Cambridge University Press. ISBN 0 521 45870 6
- FAN, H., KEER, L. and MURA, T. (1991). *The effect of plastic deformation on crack initiation in fatigue.* International journal of Solids and Structures, No. 9, pp. 1095 – 1104.
- FARHANGDOOST, K. and PROVAN, J. W. (1996). *A stochastic systems approach to fatigue reliability – an application to Ti-6Al-4V.* Engineering Fracture Mechanics 53 (5), pp. 687 – 706.
- Fatigue Handbook, (1985) Ed. Almar-Næss, Tapir, Trondheim.
- FETT, T., MATTHECK, C. and MUNZ, D. (1990). *Averaged stress intensity factors for embedded elliptical cracks.* Engineering Fracture Mechanics, Vol. 35, No. 6, pp. 987-996
- FETT, T. and MUNZ, D. (1997). *Stress intensity factors and weight functions.* Advances in Fracture series. Computational Mechanics Publications.
- FISHER, E., DZIEKONSKI, M. (1990). *The use of titanium for offshore/subsea systems.* International Conference on Titanium in Practical Applications, Trondheim, Norway.

- FOWLER, H., FOWLER, F. and ALLEN, R. (1991). *The concise oxford dictionary of current english*. Oxford University Press.
- GRAUMAN, J. S. (1999). *Titanium and titanium alloy environmental behaviour aspects for application to offshore oil and gas production*. Seminar- Titanium Risers and Flow-lines, Trondheim.
- GUOZHONG, C., KANGDA, Z. and DONGDI, W. (1995). *Analysis of embedded elliptical cracks in cylindrical pressure vessels*. International Journal of Pressure Vessel and Piping 64, pp. 153 – 159.
- GUOZHONG, C., KANGDA, Z. and DONGDI, W. (1996). *Analyses of embedded elliptical cracks in finite thickness plates under uniform tension*. Engineering Fracture Mechanics Vol. 54. No. 4, pp. 579 – 588.
- HAAGENSEN, P. J. (1998). *Introduction to fatigue*. Training in Aluminium Alloy Structural Design (WP3 Fatigue), NTNU, Trondheim.
- HELLAN, K. (1985). *Introduction to fracture mechanics*, McGraw-Hill, New York.
- HERMAN, R. (1991). *Titanium tapered joint applications*. Offshore Mechanics and Arctic Engineering (OMAE), Vol. III-A, Materials Engineering, ASME, pp. 299 – 304.
- HIBBIT, KARLSON & SØRENSEN, inc.(1998) *ABAQUS users manual: version 5.8*
- HOBBACHER, A. (1993) *Stress intensity factors of welded joints*. Engineering fracture mechanics Vol. 46. No. 2, pp. 173 – 182.
- HULL, G. A., DOS SANTOS, J. and TORSTER, F. (1999). *Radial friction welding of titanium risers - process and properties*. Seminar- Titanium Risers and Flow-lines, Trondheim.
- ISIDA, M., NOGUCHI, H. and YOSHIDA, T. (1984a). *Tension and bending of finite thickness plates with a semi-elliptical surface crack*. International Journal of Fracture 26, pp. 157 – 188.
- ISIDA, M. and NOGUCHI, H. (1984b). *Tension of a plate containing an embedded elliptical crack*. Engineering fracture mechanics Vol. 20. No. 3, pp. 387-408.

- KAM, J. C. P. (1994). *Reliability fatigue fracture mechanics*. Handbook of Fatigue Crack Propagation in Metallic Structures, pp. 1721 – 1765.
- KLESNIL, M. and LUKAS, P. (1972). *Influence of strength and stress history on growth and stabilisation of fatigue cracks*. Engineering Fracture Mechanics 5, pp. 77 – 92.
- KLESNIL, M. and LUKAS, P. (1992). *Fatigue of metallic materials*. Amsterdam: Elsevier
- LANGØY, M. A. and STOCK, S. R. (1998). Symposium on fatigue behaviour of titanium alloys. TMS Fall Meeting, Chicago, Illinois.
- LEE, D. S. (1997a). *Stress distribution in a long circular cylinder containing an elliptical crack*. Zamm. Z. angew. Math. Mech. 77, 9, pp. 701 – 709.
- LEE, D. S. (1997b). *Stress intensity factors for an embedded elliptical crack in a plate of finite thickness*. Acta Mechanica 120, pp. 127 – 140.
- LEINUM, J. R., PEDERSEN, K. and ROVEN, H. J. (1992). *Effects of crack direction on fatigue crack propagation mechanisms in an unrecrystallized AlMgSi Alloy*. Proceedings from the 3rd International Conference on Aluminium Alloys, pp. 521 – 526.
- LUNDE, L (1999). *Experiences using Titanium on Norwegian Continental Shelf*. Titanium Risers and Flowlines Seminar, Trondheim, 1999
- MAINÇON, P. (1999). *Fatigue reliability of long welds – Application to Titanium Risers*, Dr. ing. Dissertation, Norwegian University of Science and Technology, Department of Marine Structures, Trondheim, Norway.
- MALL, S., PEREZ, J. and NICHOLAS, T. (1990). *Influence of loading history on fatigue threshold behaviour in a titanium alloy*. Engineering Fracture Mechanics Vol. 37, No. 1, pp. 15-26.
- McCLUNG, R. C., LAWLESS, B. H., GORELIK, M., DATE, C., GILL, Y. and PIASCICK, R. S. (1998). Symposium on fatigue behaviour of titanium alloys. TMS Fall Meeting, Chicago, Illinois.
- MILLER, K. J. (1991). *Metal fatigue – past, current and future*. Proceedings of Institute of Mechanical Engineers, vol. 205, pp. 291 – 304.

- MURAKAMI, Y. (ed.) 1987. *Stress intensity factors handbook, (in 2 volumes)*, Pergamon Press.
- NEJAD, M., NEWBERRY, B., PHIFER, E. and ZHANG, J. (1998) *Results from Bonga steel catenary riser. Preliminary Analysis and Fatigue Testing*. Bonga Document No.: SDDSI 99-1017 for Shell Nigeria Exploration and Production Company, SNEPCO.
- NEWBERRY, B. (1998) *Thick end welded riser joints for fatigue life improvement of deepwater SCRs. Preliminary Analysis and Fatigue Testing*. Bonga Document No.: SDDSI 99-1017 for Shell Nigeria Exploration and Production Company, SNEPCO.
- NEWMAN, J.C. Jr. and RAJU, I.S. (1981) *An empirical stress intensity factor equation for the surface crack*. Engineering Fracture Mechanics, Vol. 15. No. 1-2, pp. 185-192.
- NEWMAN, J.C. Jr. and RAJU, I.S. (1983). *Stress intensity factor equation for cracks in three-dimensional finite bodies*. Fracture mechanics: Fourteenth symposium – Volume I: Theory and Analysis, ASTM STP 791, J.C. Lewis and G. Sines, Eds. American Society for Testing and Materials, pp. I238-I265.
- NISITANI, H. and MURAKAMI, Y. (1974). *Stress intensity factors of an elliptical crack or a semi-elliptical crack subject to tension*. Int. Journal of fracture, 10, pp. 353 – 368.
- NOGUCHI, H. and SMITH, R. A. (1995). *An analysis of a semi-infinite solid with three-dimensional cracks*. Engineering Fracture Mechanics, vol. 52, No.1, pp.1-14.
- PARIS, P. C. and ERDOGAN, F. (1963). *A critical analysis of crack propagation laws*. Journal of Basic Engineering 85, pp. 528-534.
- PD6493 (1991). *Guidance on methods for assessing the acceptability of flaws in fusion welded structures*. Technical Report PD6493: 1991, British Standards Institute.
- PEACOCK, D. K. (1999). *Design of high performance corrosion resistant systems for offshore application using titanium*. Titanium Risers and Flowlines seminar, Trondheim.

- PRIDDLE, E. K. (1976). *High cycle fatigue crack propagation under random and constant load amplitude*. Int. J. Pressure Vessel and Piping 4, pp. 89 – 111.
- RAMULU, M. and Kobayashi, A. (1994). *Numerical and experimental study of mixed mode fatigue crack propagation*. Handbook of Fatigue Crack Propagation in Metallic Structures, pp. 1073 – 1123
- ROCHA, M. M. and SCHUELLER, G. I. (1996). *A Probabilistic criterion for evaluating the goodness of fatigue crack growth models*. Engineering Fracture Mechanics Vol. 53, No. 5, pp. 707 – 731.
- ROOKE, D. P., BARATA, F. I. and CARTWRIGHT, D. J. (1981). *Simple methods for determining stress intensity factors*. Engineering Fracture Mechanics, Vol. 14, pp. 397 – 426.
- ROVEN, H. J. and NES, E. (1991). *Cyclic deformation of ferritic steel -II. Stage II crack propagation*. Acta Metall. Mater. Vol. 39, No. 8, pp. 1735 – 1754.
- RUPEN, J. A., HOFFMANN, C. L., RADHAKRISHAN, V. M. and McEVILY, A. J. (1980). *The effect of environment and temperature on the fatigue behaviour of titanium alloys*. FATIGUE Environment and Temperature Effects. Proceedings of the 27th Sagamore Army Materials Research Conference, held July 14-18, 1980, at the Sagamore Hotel, Bolton Landing, Lake George, New York, pp. 265 – 300.
- SCHUTZ, R. (1991). *Applicability of titanium alloys to offshore systems*. OMAE – Vol. III-A, Materials Engineering, ASME, pp. 277-285
- SCOTT, P. M. and THORPE, T.W. (1981). *A critical review of crack tip stress intensity factors for semi-elliptic cracks*. Fatigue of Engineering Materials and Structures, Vol. 4, pp. 291-309.
- SHAH, R. C. and KOBAYASHI, A.S. (1972). *Stress intensity factor for an elliptical crack approaching the surface of a plate in bending*. ASTM STP 513, pp. 3-21.
- SIMONSEN, T., MURALI, J. and FOSS, J. (1999). *The Heidrun TLP titanium drilling riser*. Proceedings of titanium risers and flowlines seminar, Trondheim, 17th Feb. 1999.

- STROUD, K. A. (1995). *Engineering mathematics (4th Edition), Programmes and Problems*. Macmillan Press Ltd.
- STROUD, K. A. (1996). *Further engineering mathematics (3^d Edition), Programmes and Problems*. Macmillan Press Ltd.
- SOLBERG, J. K. (1998). *Lecture notes on failure of metals*, Institute of material technology and electrochemistry, NTNU, Trondheim, Norway.
- SURESH, S. (1991). *Fatigue of materials*. Cambridge solid state science series
- TADA, H., PARIS, P. and IRWIN, G. (1985). *The stress analysis of cracks handbook*, Del Research Corporation, USA.
- TAYLOR, D. and JIANCHUN, L. (1993). *Sourcebook on fatigue crack propagation: Thresholds and crack closure*, Engineering Materials Advisory Services Ltd., UK.
- TO, S., LAMBERT, S. B. and BURNS, D. J. (1993). *A multiple crack model for fatigue in welded joints*. International Journal of Fatigue, 15, No. 4, pp. 333 – 340
- TOERSTAD, E. H., BRATFOS, H., ERIKSEN, G. and HAUGE, O. (1999). *Qualifying titanium risers for the Visund field*. Proceedings of titanium risers and flowlines seminar, Trondheim, 17th Feb. 1999.
- TOKAJI, K. and OGAWA, T. (1992). *The growth behaviour of microstructurally small fatigue cracks in metals*. Short Fatigue Cracks, European Structural Integrity Society, ESIS 13, Mechanical Engineering Publications, pp. 85-99.
- VAN DELFT, D.R.V., DIJKSTRA, O. D. and SNIJDER, H. H. (1986). *The Calculation of Fatigue Crack Growth in Welded Tubular Joints using Fracture Mechanics*. 18th annual Offshore Technology Conference in Houston, Texas. May 5 – 8, (OTC 5352), pp. 573 – 579.
- WANG, X., STEPHAN, B., LAMBERT and Glinka, G. (1998). *Approximate weight functions for embedded elliptical cracks*. Engineering Fracture Mechanics Vol. 59, No. 3, pp. 381-392.
- XIAO, Z. M., LIM, M. K. and LIEW, K.M. (1995). *Stress intensity factors of two internal elliptical cracks in three-dimensional solid*. Engineering Fracture Mechanics Vol. 50, No. 4, pp. 431 – 441.

- ZHENG, X. L. (1987). *A simple formula for fatigue crack propagation and a new method for determination of ΔK_{th}* . Engineering Fracture Mechanics 27, 465-475.
- ZHENG, X. L. (1994). *Mechanical model for fatigue crack propagation in metals*. Handbook of Fatigue Crack Propagation in Metallic Structures, pp. 363 – 395
- ØDEGÅRD, J. (1998). *Titanium risers and flowlines – Report 4.4 . Mechanical characterisation – Welded Joint Qualification*. SINTEF REPORT

PREVIOUS DR.ING. THESES

Department of Marine Structures

- Kavlie, Dag : Optimization of Plane Elastic Grillages. 1967.
- Hansen, Hans R. : Man-Machine Communication and Data-Storage Methods in Ship Structural Design. 1971.
- Gisvold, Kaare M. : A Method for non-linear mixed -integer programming and its Application to Design Problems.
- Lund, Sverre : Tanker Frame Optimization by means of SUMT-Transformation and Behaviour Models. 1971.
- Vinje, Tor : On Vibration of Spherical Shells Interacting with Fluid. 1972.
- Lorentz, Jan D. : Tank Arrangement for Crude Oil Carriers in Accordance with the new Anti-Pollution Regulations. 1975.
- Carlsen, Carl A. : Computer-Aided Design of Tanker Structures. 1975.
- Larsen, Carl M. : Static and Dynamic Analysis of Offshore Pipelines during Installation. 1976.
- Hatlestad, Brigit : The Finite Element Method used in a Fatigue Evaluation of Fixed Offshore Platforms. 1979.
- Valsgård, Sverre : Finite Difference and Finite Element Method Applied to Non-Linear Analysis of Plated Structures. 1979.
- Pettersen, Erik : Analysis and Design of Cellular Structures. 1979.
- Nordsve, Nils T. : Finite Element Collapse Analysis of structural Members considering Imperfections and Stresses due to Fabrication. 1980.
- Fylling, Ivar J. : Analysis of towline Forces in Ocean towing Systems. 1980.
- Haver, Sverre : Analysis of Uncertainties related to the stochastic Modelling of Ocean Waves. 1980.
- Odland, Jonas : On the Strength of welded Ring stiffened cylindrical Shells primarily subjected to axial Compression. 1981.
- Engesvik, Knut : Analysis of Uncertainties in the fatigue Capacity of Welded Joints. 1982.
- Eide, Oddvar Inge : On Cumulative Fatigue Damage in Steel Welded Joints. 1983.
- Mo, Olav : Stochastic Time Domain Analysis of Slender Offshore Structures. 1983.
- Amdahl, Jørgen : Energy absorption in Ship-platform impacts 1983.
- Czujko, Jerzy : Collapse Analysis of Plates subjected to Biaxial Compression and Lateral Load. 1983.
- Soares, C. Guedes : Probabilistic models for load effects in ship structures. 1984.

- Mørch, Morten : Motions and mooring forces of semi submersibles as determined by full-scale measurements and theoretical analysis. 1984.
- Engseth, Alf G. : Finite Element Collapse Analysis of Tubular Steel Offshore Structures. 1985.
- Baadshaug, Ola : Systems Reliability Analysis of Jacket Platforms. 1985. (Confidential)
- Hessen, Gunnar : Fracture Mechanics Analysis of Stiffened Tubular Members. 1986.
- Taby, Jon : Ultimate and post-ultimate strength of dented tubular members. 1986.
- Wessel, Heinz-J. : Fracture mechanics analysis of crack growth in plate girders. 1986.
- Leira, Bernt Johan : Gaussian Vector-processes for Reliability Analysis involving Wave-induced Load Effects. 1987.
- Xu JUN : Non-linear Dynamic Analysis of Space-framed Offshore Structures. 1988.
- Guoyang Jiao : Reliability Analysis of Crack Growth under Random Loading considering Model Updating. 1989.
- Olufsen, Arnt : Uncertainty and Reliability Analysis of Fixed Offshore Structures. 1989.
- Wu Yu-Lin : System Reliability Analyses of Offshore Structures using improved Truss and Beam Models. 1989.
- Farnes, Knut-Aril : Long-term Statistics of Response in Non-linear Marine Structures. 1990.
- Sotberg, Torbjørn : Application of Reliability Methods for Safety Assessment of Submarine Pipelines. 1990.
- Hoen, Christopher : System Identification of Structures Excited by Stochastic Load Processes. 1991.
- Sødahl, Nils : Methods for Design and Analysis of Flexible Risers. 1991.
- Haugen, Stein : Probabilistic Evaluation of Frequency of Collision between Ships and Offshore Platforms. 1991.
- Ormberg, Harald : Non-linear Response Analysis of Floating Fish Farm Systems. 1991.
- Marley, Mark J. : Time Variant Reliability Under Fatigue Degradation. 1991.
- Bessason, Bjarni : Assessment of Earthquake Loading and Response of Seismically Isolated Bridges. 1992.
- Sævik, Svein : On Stresses and Fatigue in Flexible Pipes. 1992.
- Dalane, Jan Inge : System Reliability in Design and Maintenance of Fixed Offshore Structures. 1993.
- Karunakaran, Daniel : Nonlinear Dynamic Response and Reliability Analysis of Drag-dominated Offshore Platforms. 1993.
- Passano, Elizabeth : Efficient Analysis of Nonlinear Slender Marine Structures. 1994.

- Bech, Sidsel M. : Experimental and Numerical Determination of Stiffness and Strength of GRP/PVC Sandwich Structures. 1994.
- Hovde, Geir Olav : Fatigue and Overload Reliability of Offshore Structural Systems, Considering the Effect of Inspection and Repair. 1995.
- Wang, Xiaozhi : Reliability Analysis of Production Ships with Emphasis on Load Combination and Ultimate Strength. 1995.
- Hellan, Øyvind : Nonlinear Pushover and Cyclic Analyses in Ultimate Limit State Design and Reassessment of Tubular Steel Offshore Structures. 1995.
- Hermundstad, Ole A. : Theoretical and Experimental Hydroelastic Analysis of High Speed Vessels. 1995.
- Eknes, Monika Løland : Escalation Scenarios Initiated by Gas Explosions on Offshore Installations. 1996.
- Halse, Karl Henning : On Vortex Shedding and Prediction of Vortex-Induced Vibrations of Circular Cylinders. 1997.
- Igland, Ragnar Torvanger : Reliability Analysis of Pipelines during Laying, Considering Ultimate Strength under Combined Loads. 1997.
- Vikestad, Kyrre : Multi-Frequency Response of a Cylinder Subjected to Vortex Shedding and Support Motions. 1998
- Azadi, Mohammad R. E. : Analysis of Static and Dynamic Pile-Soil-Jacket Behaviour. 1998.
- Videiro, Paulo Mauricio : Reliability Based Design of Marine Structures. 1998.
- Mainçon, Philippe : Fatigue Reliability of Long Welds Application to Titanium Risers. 1999.
- Langhelle, Nina Kristin : Experimental Validation and Calibration of Nonlinear Finite Element Models for Use in Design of Aluminium Structures Exposed to Fire. 1999.
- Berstad, Are Johan : Calculation of fatigue damage in ship structures. 1999.
- Tveiten, Bård Wathne : Fatigue Assessment of Welded Aluminum Ship Details. 1999.
- Sagli, Gro : Model Uncertainty and Simplified Estimates of Long Term Extremes of Hull Girder Loads in Ships. 2000.
- Tronstad, Harald : Nonlinear Analysis and Design of Cable Net Structures Like Fishing Gear Based on the Finite Element Method. 2000.
- Wang, Lihua : Probabilistic Analysis of Nonlinear Wave-induced Loads on Ships. 2001.
- Kristensen, Odd H.H. : Ultimate Capacity of Aluminium Plates under Multiple Loads, Considering HAZ Properties. 2001.
- Heggelund, Svein E. : Calculation of Global Design Loads and Load Effects in Large High Speed Catamarans. 2001.
- Babalola, Olusegun T. : Fatigue Strength of Titanium Risers - Defect Sensitivity. 2001.